Dissertation in Physics

submitted to the

Combined Faculties of the Natural Sciences and Mathematics

of the Ruperto-Carola-University of Heidelberg, Germany

for the degree of

Doctor of Natural Sciences

Put forward by

Simone Giacchè

born in Aosta, Italy

Oral examination: 22nd June 2016

ELECTRON AND POSITRON ACCELERATION AT PULSAR WIND TERMINATION SHOCKS

Referees: Prof. John G. Kirk
            Prof. Matthias Bartelmann

Abstract

Many astrophysical sources are very efficient particle accelerators. Among these, Pulsar Wind Nebulae (PWNe) are excellent laboratories to study the acceleration mechanism because of their proximity and brightness. In these objects, the rotational energy extracted from the central pulsar is converted in a striped-wind consisting of relativistic electrons and positrons and large-amplitude electromagnetic fields. When the wind impacts with the surrounding medium, a relativistic shock forms where the ordered flow of the pulsar becomes randomised and energetic particles emit Synchrotron and Inverse Compton radiation.

We study the conversion of the pulsar wind in a strong superluminal wave. The conversion is triggered by the interaction of the wind with the shock when this is sufficiently far away from the pulsar. The shock structure is modified by the superluminal wave and the properties of the modified shock (precursor) depend on the Lorentz factor and magnetisation of the incoming wind. A relatively large fraction of electrons and positrons in the wind is energised and reflected by the turbulent electromagnetic fields in the precursor and is available for further acceleration. We suggest that the onset of the precursor is a solution to the problem of injection in the acceleration mechanism. We investigate the acceleration of the injected particles and we find that it proceeds in two distinct regimes, determined by the relative magnitude of the wavelength of the wind stripes and of the gyro-radius of energetic particles. We discuss the implications of this acceleration scenario in the context of PSR B1259-63, a pulsar powering a PWNe in a binary system.

Zusammenfassung

Viele astrophysikalische Quellen sind effiziente Teilchenbeschleuniger. Unter diesen Quellen eignen sich Pulsar Wind Nebulae (PWNe) aufgrund ihrer Nähe und Helligkeit hervorragend für das Studium des Beschleunigungsmechanismus. In diesen Objekten wird die Rotationsenergie des zentralen Pulsars in einen gestreiften Wind (striped-wind) verwandelt, welcher sich aus Elektronen, Positronen und elektromagnetischen Feldern hoher Amplitude zusammensetzt. An der Stelle, an der der Wind auf die umgebende Materie trifft, entsteht eine relativistische Stoßfront, die die einströmende Energie thermalisiert und bewirkt, dass die darin enthaltenen Teilchen Synchrotron- und Inverse-Compton-Strahlung emittieren.

Wir untersuchen die Umwandlung des Windes in eine elektromagnetische Welle mit hoher Amplitude und einer Phasengeschwindigkeit, die die des Lichts übertrifft (superluminal wave). Die Umwandlung wird durch die Wechselwirkung des Windes mit der Stoßfront bewirkt, vorausgesetzt, dass diese sich in ausreichender Entfernung des Pulsars befindet. Die Struktur der Stoßfront wird dadurch verändert und erhält, abhängig vom Lorentzfaktor und vom Magnetisierungsgrad des Windes, einen sog. Vorläufer (Precursor). Ein verhältnismäßig hoher Anteil der einströmenden Teilchen wird in diesem Precursor (vor)beschleunigt und gespiegelt und erfüllt dadurch die Voraussetzungen, um weiter beschleunigt zu werden. Die Entstehung des Precursors löst damit das Injektionsproblem des sekundären Beschleunigungsmechanismus. Wir untersuchen diesen Mechanismus und finden unterschiedliche Eigenschaften in zwei getrennten Parameterbereichen, die durch die relative Grösse des Gyrationsradius und der Wellenlänge der Streifen definiert sind. Wir diskutieren diesen Beschleunigungs Szenario im Zusammenhang mit dem Objekt PSR B1259-63, einem bekannten Binärpulsar.

Contents

List of Figures

List of Tables

Chapter 1

Introduction

The study of particle acceleration at relativistic shock fronts is fundamental to understand and model the emission mechanism producing the radiation that we observe from many astrophysical sources. Pulsar Wind Nebulae (PWNe) host the most relativistic shocks in Nature and they share many similarities with other sources where particle acceleration is supposed to play a crucial role, such as radio galaxies, γ-ray bursters and blazars. The proximity and brightness of PWNe make them ideal laboratories to investigate the shock acceleration process common to other classes of relativistic sources.

PWNe are bubbles of relativistic particles, electron-positron pairs and perhaps ions, and large-amplitude electromagnetic fields powered by rapidly spinning Neutron Stars (NSs). The NSs, usually also observed as pulsars, dissipate their rotational energy in the surrounding medium. Only $\sim 1\%$ of the energy lost by the NS is emitted as pulsed radiation in the proximity of the pulsar, while most of it goes into the acceleration of the highly relativistic and magnetised plasma. PWNe are generated in the interaction of this ultra-relativistic wind launched by the central pulsar with the parent Supernova Remnant (SNR) or the Interstellar Medium (ISM) [55]. Their broad-band spectrum, extending from the radio to the γ-ray band, is normally modeled as Synchrotron and Inverse Compton emission from a non-thermal (power-law) distribution of electron-positron pairs. These particles are supposed to be accelerated at the so-called Termination Shock (TS), the collisionless shock front separating the magnetised pulsar wind and the unmagnetised nebula. However, it is still a matter of debate which is the mechanism responsible for the acceleration of these particles and which is the location where it takes place.

Diffusive Shock Acceleration (DSA) or Fermi Acceleration [12, 18, 22] has become a paradigm for the production of energetic particles in the proximity of strong non-relativistic shocks in magnetised plasma. DSA is a stochastic process relying on repeated scattering of charged particles off magnetic irregularities to confine the particles near the shock front, that they perceive as a discontinuity in the flow. These particles gain energy crossing the shock multiple times until they escape downstream of it. The spectrum of accelerated particles builds up in a power-law distribution $N(\gamma)d\gamma \propto \gamma^{-s}d\gamma$, where γ is the Lorentz factor of energetic particles and s is the power-law spectral index. Whether a similar process can be efficient at the ultra-relativistic TS in PWNe is unclear. In fact, the escape probability downstream of the shock increases for large values of the Lorentz factor of the shock front and consequently the efficiency of the acceleration process diminishes. Another issue to deal with is the injection problem. By this, we mean that not all the particles in the pulsar wind participate to the acceleration mechanism, but only those which are decoupled from the background plasma, are pre-accelerated until their gyro-radius is larger than

the thickness of the shock and are reflected upstream of the shock front. The injection problem is intimately related to the dynamics and evolution of the flow and of its energy content from the central source (the NS) to the TS and subsequent nebula, which also determine the amount of energy available to be radiated.

The mixture of electromagnetic fields and electron-positron plasma constituting the pulsar wind propagates outwards as an electromagnetic wave. In the inner region of the wind, the plasma density is large enough to screen out any electric field component along the magnetic field lines. The absence of an electric field in the proper frame of the plasma allows the use of the equations of relativistic magnetohydrodynamics (MHD) and the wave is described as a striped-wind (equivalent to an entropy wave), where stripes of toroidal magnetic field of opposite polarity are separated by thin current sheets. In this part of the wind the energy content is dominated by the fields. As the wind expands, its density drops as $1/r^2$ and at sufficiently large radius it is no more sufficient to sustain an ideal MHD wave and the propagation of strong superluminal waves becomes possible (see Sect. 1.2). In the outer part of the wind the energy content of the flow is dominated by plasma particles. Observations of the emission from PWNe require that this is verified in particular in proximity of the TS. Interestingly, in PWNe environments the conversion of the striped (MHD) wind into a strong electromagnetic wave can manifest as a precursor to the TS where a large amount of energy stored in the electromagnetic fields is transferred to particles [6, 107]. This process, which cannot be accommodated in the ideal MHD approximation, is highly attractive to explain the observation of non-thermal radiation from PWNe. The conversion of the electromagnetic energy into direct particle kinetic energy can in turn decouple a fraction of electrons and positrons from the rest of the plasma and pre-accelerate it.

The goal of this work is to investigate whether a process similar to DSA, that we shall call Fermi-like or simply Fermi acceleration, is able to accelerate electrons and positrons at the ultra-relativistic pulsar wind TS as required by the observation of Synchrotron and Inverse Compton emission from PWNe. We investigate the formation and the properties of the shock precursor mediated by superluminal waves generated by the conversion of the pulsar striped-wind. We do this using a newly developed two-fluid code [6] and we suggest that the formation of the precursor to the TS constitutes a solution to the injection problem. Subsequently, we simulate the full Fermi-like acceleration process of particles injected by the precursor using a Monte Carlo approach, where the presence of magnetic turbulence (acting as elastic scattering centres) is realised with the standard technique of *pitch-angle* scattering. This is done both upstream of the shock, in the pulsar wind, and downstream of it, in the nebula. We find that the acceleration proceeds in two regimes, one dominated by the magnetic field in the stripes of the pulsar wind and one dominated by the scattering off magnetic irregularities, according to the relative magnitude of the wavelength of the stripes and of the particles gyro-radius. For values of these parameters reasonable in PWNe environments, the Fermi-like acceleration proceeds in the scattering-dominated regime and produces a power-law spectrum with index $s \sim 4.23$.

As a testbed of our model for particle acceleration in PWNe, we consider the pulsar PSR B1259-63 which orbits the massive Be star SS 2883 (e.g., [65, 66, 108, 1]). Contrary to a young isolated PWN, where the density in the pulsar wind is dictated by the pressure of the confining medium (the SNR or ISM), for a PWN in a binary system the density, and correspondingly the condition for the conversion of the striped-wind into superluminal waves, depends on the confining pressure of the companion stellar wind. Thus, the orbital motion might periodically lead to the formation of the shock precursor. Recent observations of PSR B1259-63 measured for two consecutive orbits an outstanding and unforeseen flare in the GeV band [1, 131]. Assuming that the beginning of the flare coincides with the onset of the TS precursor, which leads to efficient electrons and positrons acceleration, we are able to estimate the density in the pulsar wind. This value of the density is in agreement, within a factor of ~ 3, with the

value computed with pair-production models in the pulsar magnetosphere.

The remaining of this chapter has an introductory goal to acquaint the reader with PWNe, as they are central to the thesis. In Sect. 1.1 we summarise the present status of our knowledge about PWNe, referring to observations, theoretical and numerical works. We separate the structure of these sources in three main regions, namely the magnetosphere, the wind region and the nebula, that we describe in Sects. 1.1.1, 1.1.2 and 1.1.3, respectively. In Sect. 1.2 we present the conditions under which the pulsar striped-wind can converts into a superluminal wave and the parameters describing this electromagnetic mode and in Sect. 1.3 we briefly summarise the mechanisms which might contribute to the acceleration of particles at the TS of the pulsar wind. Section 1.4 is dedicated to the class of sources known as γ-ray binaries and to the specific case of its prototype object, PSR B1259-63. Finally, in Sect. 1.5, we summarise the content of the remaining chapters and appendices of this thesis.

1.1   Structure of Pulsar Wind Nebulae

The central NS, ultimate source of energy of a PWN, spins with period P (and frequency ω). It dissipates its rotational energy driving the pulsar wind in the surrounding medium and consequently slows down at a rate $\dot{P}$. The observation of the characteristic radio pulses from this star allows to compute the total pulsar spin-down luminosity as

$$L_{\mathrm{SD}} = 4\pi^2 I \frac{\dot{P}}{P^3} \tag{1.1}$$

where I is the NS moment of inertia, which for a NS mass of $1.4\,M_\odot$ ($M_\odot$ is the solar mass) and a radius of $10\,km$ is $I \sim 10^{45}\,g\,cm^{-2}$. Typical values for PWNe are $L_{\mathrm{SD}} \sim 10^{34} - 10^{38}\,erg\,s^{-1}$ [55]. The pulsar wind is apparently radiationless as it expands outwards until its pressure is balanced by the ram pressure of the surroundings. Here, a relativistic shock forms, the termination shock, where the flow is slowed down to adjust its speed to the non-relativistic speed of the expansion of the SNR ($\sim 10^3 km\,s^{-1}$). At this location, the radial flow of the wind is randomised and its bulk energy is transformed into that of a relativistically hot plasma, which shines via Synchrotron and Inverse Compton emissions in the observed nebula. The nebula has different morphologies and sizes at different frequencies, as it can be seen in the composite image of the Crab in Fig. 1.1, where X-rays are shown in blue, optical in green and radio in red. This might be the signature of the radiative cooling of the highest energy particles as they are convected and diffuse away from the inner nebula, or of different acceleration sites for radio-emitting and X-ray-emitting electrons and positrons [30]. Radio emission traces the contour of the nebula, whereas X-rays highlight the shape of the region where most of the wind energy is deposited and particles are accelerated. The jet-torus geometry showed in Fig. 1.1 (evident in X-rays) is considered to be archetypal for PWNe around young pulsars whose velocities are smaller than the speed of sound inside their host SNRs [67]. The torus is the region where most of the energy of the wind is deposited in the nebula and its shape, elongated in the equatorial plane and more compact along the rotation axis, is due to the intrinsic anisotropy of the wind (see Sect. 1.1.2). The jet instead arises because of the collimation of the flow along the rotation axis [89]. On the other hand, if the pulsar speed is supersonic, PWNe are highly distorted and acquire a cometary shape as shown in the X-ray image plotted in the left panel of Fig. 1.2 for the Mouse PWN. This can happen in two distinct scenarios. (1) The pulsar reaches the edge of the SNR shell and drives a bow-shock in the exterior medium. This normally occurs if the pulsar speed is in excess of $10^3 km\,s^{-1}$ and its age is few tens of thousands years (e.g., [55, 67]). Few tens of objects are observed to be in this evolutionary stage [68]. (2) A pulsar and its nebula orbit a massive star with strong stellar wind. In this case, the orbital motion and the interaction with the stellar outflow confines the PWN in a cometary shape.
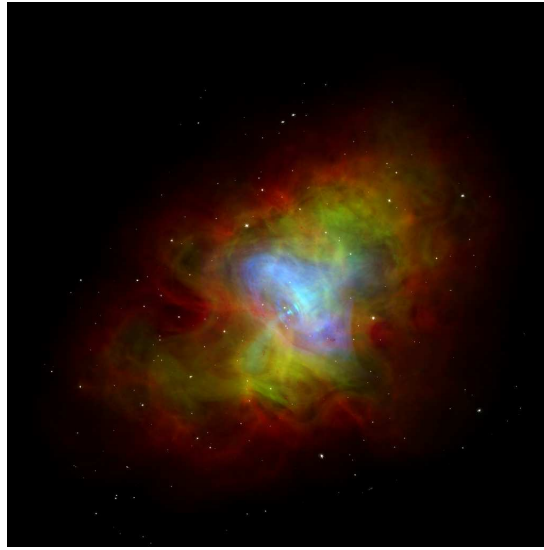
Figure 1.1: Composite image of the Crab Nebula, showing *X*-rays in blue, optical in green and radio in red. Credits: *X*-ray: NASA/CXC/ASU/J. Hester et al.; Optical: NASA/HST/ASU/J. Hester et al.; Radio: NRAO/AUI/NSF [61].
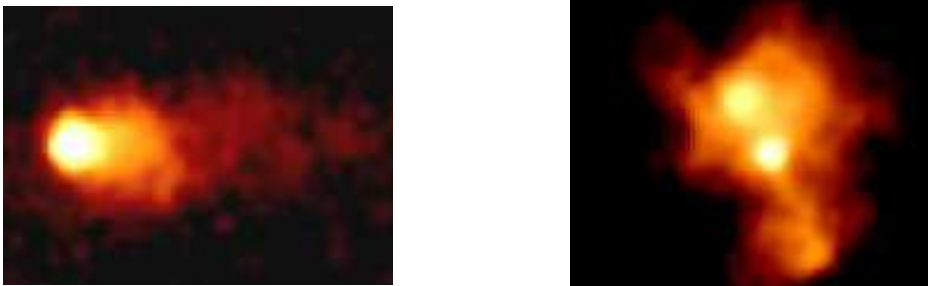
Figure 1.2: Chandra *X*-ray images of PWNe. Left panel: the Mouse PWN, example of the bow-shock-tail geometry. Right panel: the Kes 75 PWN, example of an amorphous geometry. These images must be compared to the *X*-ray image (in blue) in Fig. 1.1 for comparison with the torus-jet geometry. Credits: adapted from Kargaltsev & Pavlov 2008 [68].

This scenario has been suggested to explain the phenomenon of γ-ray binaries (see Sect. 1.4). Eventually, the prolonged interaction of the powerful environment of PWNe with the surrounding medium or highly anisotropic

supernova ejecta lead to amorphous geometries [68], as shown in the *X*-ray image plotted in the right panel of Fig. 1.2 for the Kes75 PWN. Both panels of Fig. 1.2 must be compared with the *X*-ray image of the Crab (in blue in Fig. 1.1) for comparison with the torus-jet geometry.

However, despite the diverse observed morphologies, which most likely depend on the time evolution of the system and therefore on the properties of the progenitor and of the environment, one single paradigm for the structure of PWNe, though not yet complete, can be constructed. This paradigm mainly relies on observations and modeling of the Crab nebula, which is the best studied of such systems (see [30] for a review).

1.1.1 Magnetosphere

The inner region of a PWN is the magnetosphere, conventionally extending from the star surface up to the light cylinder radius $r_{LC} = c/\omega$, which is the distance at which the speed of a particle corotating with the NS becomes luminal. The dynamics in the magnetosphere is completely dominated by very strong electromagnetic fields. However, this is also true for at least part of the wind region which lies outside r_{LC}. The magnetosphere is modeled in the context of Force Free Electrodynamics (FFE), a low inertia limit of Magneto-Hydrodynamics (MHD).

The compression, during supernova collapse, of the magnetic field of the parent star into a NS of radius $r_{NS} \sim 10\,km$ and the dynamo effect [20, 127] produce a magnetic field in excess of $B = 10^{12}\,G$ for most pulsars showing PWNe [55]. The rotation of such a magnetic field induces an enormous electric field which is able to tear particles from the stellar surface. These particles are then accelerated in charge-starved regions (or gaps) where $\mathbf{E} \cdot \mathbf{B} \neq 0$, probably located close to the magnetic poles [8, 120], and redistributed in order to screen out the accelerating field component in the magnetosphere. The necessary particle density is given by the Goldreich-Julian density

$$n_{GJ} = \left| \frac{\omega \cdot \mathbf{B}}{2\pi ec} \right| \tag{1.2}$$

(e.g., [104]) where ω is the angular velocity and $\mathbf{B}$ is the magnetic field of the star. In the gaps, energetic particles emit curvature radiation streaming along curved magnetic field lines (rather than Synchrotron radiation arising from the gyration about the field lines) since they are accelerated by $\mathbf{E} \parallel \mathbf{B}$. If the emitted photons are energetic enough, they can produce electron-positron pairs in the strong magnetic field of the pulsar. These secondary particles radiate their energy in two channels. (1) The component of the momentum perpendicular to the field line is radiated via Synchrotron radiation. (2) The component of the momentum parallel to the field line is radiated via Inverse Compton Scattering of thermal photons coming from the surface of the NS or of *X*-ray photons produced by the Synchrotron channel [141]. The secondary photons may produce further pairs, leading to an electromagnetic cascade which fills the magnetosphere with plasma (e.g., [63]). The number of secondary particles generated by each primary is parametrised by the multiplicity factor κ. According to numerical simulations and comparisons with the spectrum of the Crab Nebula, the multiplicity factor is $\kappa \sim 10^4 - 10^6$ (e.g., [72, 28, 125]), while pair production models suggest $\kappa \sim 10^1 - 10^5$ [8, 62, 63, 135]. In principle, ions can also be extracted from the star surface as primary particles, but given that they are not produced during the cascades, their number density contributes at most a factor $1/\kappa$ to the total number density. If the multiplicity is as large as suggested, their contribution is negligible both in number and energy density content.

In the ideal MHD approximation, the electron-positron plasma within the light cylinder corotates with the NS with speed $\mathbf{v} = \omega \times \mathbf{r}$. Except inside the gaps, the electric field $\overline{\mathbf{E}}$ vanishes in the proper frame of the fluid because the

magnetic field is frozen into the corotating plasma. This ideal-MHD condition is expressed by

$$\overline{\mathbf{E}} = \mathbf{E} + \mathbf{v} \times \mathbf{B}/c = 0 \tag{1.3}$$

(over-lined quantities are expressed in the proper frame of the plasma). The magnetic field lines are nearly equipotential (*i.e.* $\mathbf{E} \cdot \mathbf{B} = 0$), so that charged particles can be thought of as sliding along the field which rigidly corotates with the NS [57]. The magnetic field lines which pass through the light cylinder are open and extend beyond the magnetosphere. Plasma sliding along open field lines leaves the pulsar magnetosphere at a rate $\dot{N} = \kappa \dot{N}_{\text{GJ}}$ where

$$\dot{N}_{\text{GJ}} \approx \frac{\omega^2 r_{\text{NS}}^3}{ec} B \tag{1.4}$$

is the Goldreich-Julian particle flux from the polar caps stemming from the definition of the Goldreich-Julian density given in Eq. 1.2. The existence of a steady state in the magnetosphere is granted by the presence of the gaps, continuously replenishing it and balancing the outflowing charges with pairs whose energy ranges from tens to hundreds of MeV [82].

1.1.2 Wind

Outside the light cylinder, the plasma cannot corotate, because the motion would be superluminal. Hence, the magnetic field lines are wrapped backwards with respect to the rotation of the NS. This is due to the fact that the magnetic field is frozen into the plasma (condition expressed in Eq. 1.3). For an aligned rotator, the situation is properly described by the split-monopole model [102], where the magnetic field lines propagate to infinite in the northern hemisphere and from infinite in the southern hemisphere. The change in magnetic polarity is accompanied by the formation, in the equatorial plane, of a current sheet of hot plasma and null magnetic field which balances the magnetic pressure. This steady and axisymmetric model has been generalised by [23] to the oblique rotator. The inclination of the magnetic-axis to the spin-axis ζ causes the current sheet to oscillate around the equatorial plane, separating regions connected to opposite magnetic poles every half a period. The situation is represented in Fig. 1.3. The current sheet cuts the equatorial plane in twins spirals separating the stripes of opposite magnetic polarity, from which the name of striped-wind. The plasma in the stripes is magnetised and cold whereas the plasma in the current sheet is unmagnetised and relativistically hot. The corresponding structure in hydrodynamics is called an entropy wave of wavelength $\lambda = 2\pi r_{\text{LC}}$. For colatitudes $\theta \sim \pi/2$ in the pulsar wind, where θ is the polar angle computed from the pulsar spin-axis, the stripes have the same width $\lambda/2$ and the average field integrated over λ vanishes, while at lower (or higher) colatitudes an average magnetic field survives because of the different length of the stripes of opposite polarity. At colatitudes $\theta < \pi/2 - \zeta$ and $\theta > \pi/2 + \zeta$, the field does not change sign and there is no current sheet embedded in the flow.

At the light cylinder, the magnitude of the poloidal and azimuthal components of the field are comparable. However, conservation of the magnetic flux in a diverging flow allows to compute the radial dependence of B_{r}, B_{θ} and B_{ϕ} [29] as follows

$$B_{\text{r}} \propto \frac{r_{\text{LC}}}{r^2} \tag{1.5}$$

$$B_{\theta} \propto \frac{r_{\text{LC}}}{r^3} \tag{1.6}$$

$$B_{\phi} \propto \frac{r_{\text{LC}}}{r} \tag{1.7}$$
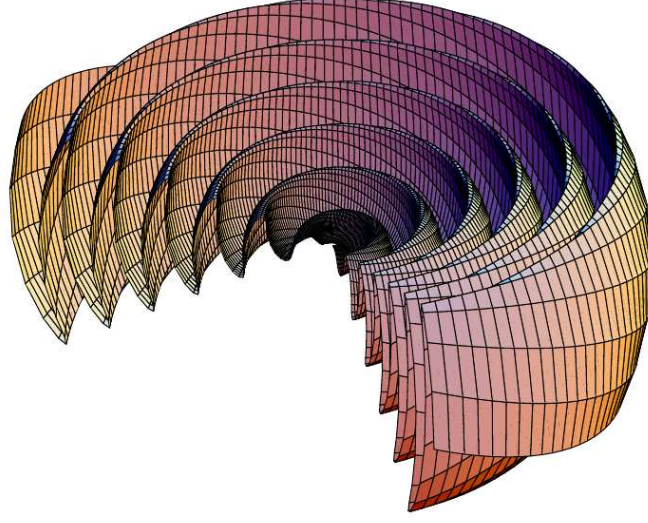
Figure 1.3: Corrugated current sheet separating the regions of opposite magnetic polarity in the striped-wind model. Credits: Kirk *et al.* 2009 [80].

which means that for large radial distances from the light cylinder the azimuthal component B_ϕ dominates and the field is mainly toroidal. Hence, the magnetic field structure can be regarded as concentric rings of constant toroidal magnetic field of opposite sign separated by sheets of poloidal current $\mathbf{j}_\theta$ of width Δ, which is of the order of the thermal Larmor radius [41]. The $\mathbf{j}_\theta \times \mathbf{B}_\phi$ force exerted on the charge carriers by the poloidal current and the toroidal field might cause the evolution of the current sheet from a purely sinusoidal profile into a square wave profile, where the current sheet itself becomes thinner [41, 105].

The relative strength of the electromagnetic and particle content of the wind is an important characteristic of the flow and it also depends on the radial distance r. This is expressed using the magnetisation parameter σ, defined as the ratio of the magnetic energy density to the particle enthalpy density in the proper frame as follows

$$\sigma = \frac{\overline{B}^2}{4\pi\overline{w}} \tag{1.8}$$

where $\overline{w}$ is the proper enthalpy density of the plasma ($\overline{\mathbf{E}} = 0$ in this frame). Given that we assumed the plasma to be cold, the proper enthalpy is nothing but the rest mass energy density $\overline{w} = m_e c^2 n/\Gamma$, where n is the particle number density and Γ is the Lorentz factor of the wind in the frame where the NS is at rest (lab. frame), assumed to be $\Gamma \gg 1$. In addition, since the magnetic field is completely transverse to the wind velocity, we can write $\overline{B} = B/\Gamma$ and express the magnetisation in the lab. frame as

$$\sigma = \frac{B^2}{4\pi m_e c^2 n\Gamma} \tag{1.9}$$

which is the ratio of the Poynting flux to the particle kinetic energy flux.

The wind emerging from the magnetosphere at the light cylinder is characterised by $\sigma \gg 1$, namely the energy content of the electromagnetic component of the wind dominates over that of the plasma particles (e.g., [71, 72]).

The fast magnetosonic speed v_{fms} of such a flow is thus very close to the speed of light since

$$v_{\text{fms}} = \frac{c\overline{B}}{\sqrt{4\pi\overline{w} + \overline{B}^2}} \approx c\sqrt{\frac{\sigma}{1+\sigma}} \tag{1.10}$$

and the corresponding Lorentz factor is $\Gamma_{\text{fms}} = \sqrt{\sigma}$ [79]. Although relativistic, the wind is supposed to be subsonic at its base $\Gamma \lesssim 100 < \Gamma_{\text{fms}}$ [40]. In the FFE approximation, it then accelerates as it travels outwards until $\Gamma \sim \Gamma_{\text{fms}}$ at the sonic point [29], where the plasma inertia becomes important and the FFE approximation breaks down. The wind is still Poynting dominated at the sonic point and it propagates as an ideal-MHD flow. However, this cannot proceed indefinitely because the particle density drops faster than the toroidal magnetic field and the wind becomes unstable. In fact, as pointed out by [105], the mass continuity requires that $nvr^2 = $ constant in a steady, spherical and relativistic flow, so that the density of current carriers drops as $n \propto 1/r^2$. Integrating Ampère's law in the plasma frame over the toroidal ring of width $\overline{\Delta}$ we obtain

$$2\overline{B}_\phi = \frac{4\pi}{c}\overline{j}_\theta\overline{\Delta} \tag{1.11}$$

where $\overline{j}_\theta = \overline{n}ev_\theta$ and v_θ is the poloidal drift velocity of electrons (the drift velocity of positrons is in the opposite direction and the two currents add up). The transformations into the lab. frame $B_\phi = \Gamma\overline{B}_\phi$, $n = \Gamma\overline{n}$, $\Delta = \overline{\Delta}/\Gamma$ give

$$B_\phi \propto \Gamma nv_\theta\Delta. \tag{1.12}$$

Here, the left-hand side evolves as $1/r$ (see Eq. 1.7) and the right-hand side as $1/r^2$ if Γ and Δ were constant (notice that the drift velocity v_θ is limited by c). This means that, in these conditions, at some distance from the light cylinder there cease to be enough particles to carry the current sustaining the wind. However, the dissipation of the magnetic field could alleviate this issue. According to [41, 93], the current sheet is able to sweep up additional particles from the adjacent stripes. Thus, its width Δ increases and the magnetic field reconnects (annihilates) in the sheet. This mechanism efficiently converts Poynting flux into particle kinetic energy. As a result, the wind is accelerated further. The maximum wind Lorentz factor, attainable when the Poynting flux is completely dissipated, is thus $\hat{\mu} = \sigma_{\text{LC}}\Gamma_{\text{LC}}$, where Γ_{LC} and σ_{LC} are the Lorentz factor and the magnetisation at the light cylinder, respectively. Nevertheless, as a consequence of the acceleration of the wind, the dissipation time scale suffers from relativistic time dilation. Whether or not the dissipation of the Poynting flux proceeds to completion before the wind encounters the termination shock depends on the field annihilation rate in the rest frame of the stripes. In the slow regime, the wind Lorentz factors grows as $\Gamma \propto r^{1/2}$, which allows only a fraction of the wind magnetisation to be converted into particle kinetic energy within the termination shock for all but millisecond pulsars [93]. Instead, in the fast regime, a sizeable fraction of the Poynting flux can be dissipated as $\Gamma \propto r^{1/3}$ [86]. Typical values for the Crab, inferred from observations or computed with numerical simulations, are $\sigma_{\text{LC}} \sim 10^4 - 10^5$, $\Gamma_{\text{LC}} \sim 200$ and $\Gamma \sim 10^5 - 10^6$ (e.g., [41, 82]).

1.1.3 Termination shock and nebula

When the pressure of the relativistic electron-positron wind is balanced by the ram pressure of the surrounding medium, a termination shock forms, where the pulsar wind injects its energy in the surrounding nebula in the form of relativistic electron-positron pairs and magnetic field. The surface of the TS is highly non-spherical. A part from the deformations owed to the possible inhomogeneities in the supernova ejecta, the luminosity per solid

angle scales as $dL/d\Omega \propto \sin^2 \theta$ [103, 23], so that most of the energy is transported in an equatorial belt, whose extension depends on the inclination of the magnetic-axis with respect to the spin-axis [24]. As a consequence, the TS is oblate with a cusp-like shape at the poles, as can be observed for example in the *X*-ray image of the Crab (see Fig. 1.1). The toroidal shape of the TS has been computed analytically by [94] simply equating the ram pressure of the pulsar wind to the downstream pressure, assuming that the latter is roughly constant on the surface of the TS. Subsequently, 2-dimensional and 3-dimensional relativistic MHD simulations (e.g., [88, 42, 116]) confirmed the results of the analytic estimate. In the axisymmetric picture considered in these works, the TS is perpendicular since the magnetic field is asymptotically toroidal far away from the pulsar and the shock normal has no azimuthal component.

PWNe are observed to emit from radio to TeV frequencies, with a luminosity close to $10 - 20\%$ of the total pulsar spin-down luminosity [71]. This radiation is mainly associated to Synchrotron radiation produced by particles emitting in the nebular magnetic field and to Inverse Compton scattering of CMB and Infra-Red photons. The resulting spectrum can be modeled with a broken power-law with few spectral breaks. In radio, the spectral index of the observed flux density $\mathscr{F}_\nu \propto \nu^{-\alpha}$ is $0 \lesssim \alpha \lesssim 0.3$, while at higher frequencies the spectrum is steeper (in *X*-rays $\alpha \sim 1.1$) [55]. For the Crab nebula, this implies that the energy of emitting electrons and positrons ranges from ~ 100 MeV to ~ 1 PeV [82], an that their energy distribution is probably a power-law with one or more breaks. Hence, efficient particle acceleration must take place at the TS, where the bulk energy of the wind is transformed into the kinetic energy of particles.

The dynamics of the acceleration is connected to the Poynting flux dissipation mechanism. We know in fact that the wind is launched from the pulsar magnetosphere with $\sigma \gg 1$, but downstream of the TS the magnetisation must be low. This is required by two observational constraints: (1) the speed of the post-shock medium must match the speed of the expanding nebula [118]; (2) most of the energy must be carried by particles, rather than electromagnetic fields, to justify the spectrum of PWNe. In early 1-dimensional studies it was difficult to reconcile these two requirements with the expectations of pulsar wind electrodynamics. In fact, in ideal MHD a radial highly-magnetised (with a toroidal magnetic field) supersonic relativistic pulsar wind cannot be slowed down by a shock to match the typical expansion speed of the confining SNR. This can be achieved only for very low magnetisation $\sigma \sim 10^{-3}$ (e.g., [71, 72]), whereas the pulsar wind, with minor deviations from a purely radial outflow, could have $\sigma \sim 1$ at the typical distances of the nebula [37]. The inability of theoretical models to explain the transition from a highly magnetised wind to a low-magnetisation post-shock flow is known as the σ-problem, whose solution is still a matter of debate. It has been suggested [16] that the σ-problem is an artifact of 1-dimensional models which suppress current instabilities and magnetic field turbulence and mixing. If this is true, the value of the magnetisation needed to meet constraints (1) and (2) would not need to be as low as $\sigma \sim 10^{-3}$. This view in supported by 2-dimensional relativistic MHD simulations (e.g., [42, 43]), where the value of the magnetisation necessary to reproduce the observed jet-torus morphology of the Crab nebula is $\sigma \gtrsim 0.03 - 0.1$. In this case, the extra degree of freedom allows to accommodate a larger degree of turbulence and mixing and thus a larger magnetisation, partially alleviating the σ-problem. Recently, the results of 3-dimensional relativistic MHD simulations [115, 116] showed that a good agreement with the observations of the Crab can be obtained also for a magnetisation of order unity, which is much closer to the expectations of pulsar wind electrodynamics. This is particularly due to randomisation of the magnetic field in the body of the nebula and partial dissipation of the magnetic energy. Further studies are required to understand whether the rate of magnetic dissipation in these simulations is still excessive [116].

The partial alleviation of the σ-problem implied by the results of 2-dimensional, and in particular 3-dimensional,

simulations does not rule out the possibility that other non-ideal effects play a role [27]. For example, it has been suggested that, when the striped-wind instability described in the previous section is not able to entirely dissipate the Poynting flux, the encounter of the MHD flow with the shock drives the reconnection mechanism and leads to complete dissipation of σ [95]. This is due to the fact that the plasma is compressed by a huge factor across the shock, of the order of the ratio of the Lorentz factors of the flow upstream and downstream. Thus, the downstream temperature becomes comparable to the particle kinetic energy upstream, so that the width of the sheet Δ exceeds the wavelength of the stripes. As a result, the striped pattern is erased and the magnetic field annihilated.

Here, we suggest an alternative scenario, where the dissipation of the Poynting flux is mediated by strong superluminal waves generated via mode conversion of the MHD wind.

1.2   The role of superluminal waves

The rotation of a magnetised NS whose magnetic dipole axis is misaligned with respect to the spin-axis is expected to drive in the plasma a large variety of electromagnetic waves at the rotational frequency of the pulsar (ω) [100]. However, the density of the plasma at the light cylinder is large enough to cause severe damping of low-frequency waves and it is conceivable that only MHD waves survive at distance $r > r_{\rm LC}$ [10], namely those waves satisfying $\mathbf{E} + \boldsymbol{\beta} \times \mathbf{B} = 0$, where $\boldsymbol{\beta}$ is the velocity of the wave. The phase speed of these waves is $\beta_\phi = E/B < 1$, *i.e.*, subluminal [6]. A rotating and magnetised NS can be expected to emit waves whose polarisation is predominantly linear in the equatorial plane, circular in the polar region, and with different degrees of elliptical polarisation at intermediate latitudes [76]. The linearly polarised wave in this picture corresponds to the striped-wind configuration introduced above. We stress that the striped-wind and the wave descriptions of the pulsar wind are not in contradiction. Rather, they are complementary approaches to be applied at relatively high plasma density (striped-wind) and low plasma density (wave), so that in the following we will use striped-wind and subluminal wave as synonyms.

As already said, the subluminal wave requires a minimum plasma density in order to propagate as an ideal MHD wave. Hence, this provides a good description of the pulsar wind in the inner part of the outflow, but not beyond a critical radius $r = r_{\rm LC} \cdot a_{\rm L}/\hat{\mu}$ [7]. In this expression, the parameter

$$a_{\rm L} = \sqrt{\frac{4\pi e^2 L_{\rm SD}}{m_{\rm e}^2 c^5 \Omega_{\rm s}}} \tag{1.13}$$

is the strength parameter of a circularly polarised vacuum wave that would be needed to carry the entire pulsar luminosity $L_{\rm SD}$ at the surface of the light cylinder [7, 107], where $\Omega_{\rm s}$ is the portion of sky occupied by the wind, e is the fundamental electric charge and $m_{\rm e}$ is the electron mass. The parameter

$$\hat{\mu} = \frac{L_{\rm SD}}{\dot{N} m_{\rm e} c^2} \tag{1.14}$$

is the energy carried per particle in units of $m_{\rm e}c^2$ (also called mass-loading factor of the wind [102]), where $\dot{N}$ is the pair production rate of the pulsar. This corresponds to the maximum bulk Lorentz factor Γ that is achieved only when the entire energy flux is carried by cold particles. These relations allow us to define a dimensionless expression of the radial coordinate

$$R = \frac{\hat{\mu}}{a_{\rm L}} \frac{r}{r_{\rm LC}} \,. \tag{1.15}$$

The dimensionless critical radius is $R = 1$. For $R > 1$, the MHD picture can be extended by considering electromagnetic waves of superluminal phase speed ($E > B$) [7]. Non-linear solutions for superluminal waves have been obtained for two polarisations: linear [11] and circular [76]. For the circular polarisation there exist two modes, one free-escaping and one confined [76]. The former detaches from the fluid particles, becomes a vacuum wave and has the same magnetisation of the MHD wave, thus we are not interested in this mode. The latter does not detach from the fluid and dissipates the magnetisation into particle energy [76, 6], which constitutes a viable mechanism for the dissipation of the Poynting flux in PWNe.

The condition for the propagation of superluminal waves $R > 1$ is equivalent, in frequency space, to the dispersion relation [76]

$$\omega = \Gamma_> \overline{\omega}_p \qquad (1.16)$$

expressed in terms of the proper plasma frequency

$$\overline{\omega}_p = \sqrt{\frac{4\pi e^2 \overline{n}}{m_e}} \qquad (1.17)$$

where $\overline{n}$ is the proper number density of the plasma. In Eq. 1.16, $\Gamma_>$ is the Lorentz factor corresponding to the speed $\beta_> = c/v_\phi < 1$ [7] (v_ϕ is the superluminal wave phase speed) performing the Lorentz transformation from the lab. frame to the homogeneous frame or H-frame [38, 39]. Seen from an observer in this frame, which moves radially outwards with speed $\beta_>$, the wave is spatially homogeneous and the magnetic field vanishes. Equation 1.16 states that the proper plasma frequency is the cut-off frequency for superluminal waves since $\omega > \overline{\omega}_p$.

The conversion to a superluminal wave can occur in two different scenarios. (1) Spontaneously, when the magnetic reconnection proceeds too slowly to maintain the pressure balance between the magnetic stripes and the current sheets required for the evolution of the radial wind. (2) Triggered by the interaction of the wind with the termination shock. However, independently of the scenario, the superluminal wave must initially carry the same energy, momentum and particle fluxes of the incoming subluminal wave. In the striped-wind the energy per particle (in units of $m_e c^2$) is given by $\hat{\mu}$ defined in Eq. 1.14, the radial momentum per particle (in units of $m_e c$) is

$$\nu \approx \hat{\mu} - \frac{\sigma}{2\hat{\mu}} \qquad (1.18)$$

and the particle flux density is

$$J = 2c\overline{n}^u \Gamma \beta \qquad (1.19)$$

where σ, Γ and β are the magnetisation, Lorentz factor and speed of the wind, respectively [107]. The set of jump conditions between the circularly polarised subluminal and superluminal modes, ensuring that these quantities are conserved, is the following [7, 107]

$$\hat{\mu} = \gamma + \frac{\beta_> \Gamma_>^2 p_\perp^2}{p_\parallel} \qquad (1.20)$$

$$\nu = p_\parallel + \frac{\Gamma_>^2 p_\perp^2 (1 + \beta_>^2)}{2p_\parallel} \qquad (1.21)$$

$$J = 2c\overline{n}^d p_\parallel \qquad (1.22)$$

where γ, $p_\parallel$ and $p_\perp$ are the Lorentz factor, parallel and transverse momenta (the latter both in units of mc) of the fluids (electrons and positrons), respectively. Here $p_\parallel = \hat{\mu}\Gamma_>^2/R^2$ and $p_\perp \approx \gamma$ provided that the flow remains

relativistic [107]. We remark that the quantities $\bar{n}^{\,\mathrm{u}}$ and $\bar{n}^{\,\mathrm{d}}$ in Eqs. 1.19 and 1.22 are the wind proper densities respectively upstream and downstream of the surface at distance R from the pulsar where the conversion takes place. In particular, $\bar{n} = \bar{n}^{\,\mathrm{d}}$ in Eq. 1.17 (Eqs. 1.17, 1.19 and 1.22 can be used to estimate the wind proper density at the TS; for more details see Sect. 5.4).

Once generated, superluminal waves can propagate both in the forward and backward directions and, when they interact with a shock, they strongly modify and finally dominate the shock structure [126, 6]. Despite their strongly non-linear amplitudes under pulsar conditions, these waves are efficiently damped through instabilities (e.g., [99, 10]), leading to plasma heating. Interestingly, it has been shown analytically [107] and numerically [6] that the confined superluminal mode can settle as a steady wave in an electron-positron plasma, creating a shock precursor ahead of the TS where the Poynting flux is dissipated[1]. The mechanism of conversion of the pulsar striped-wind into superluminal waves and their subsequent damping is important not only for the solution of the σ-problem, but also because it might create a favourable ambient for particle acceleration in the proximity of the TS.

1.3 Particle acceleration in PWNe

Being the region where most of the wind bulk energy is deposited in the plasma, the TS seems to be the natural location for particle acceleration. This argument is strengthened by the observation of X-ray Synchrotron emission from a toroidal structure located at $r_{\mathrm{TS}} = 4 \cdot 10^{17}\,cm$ from the Crab pulsar (e.g., [101]), which is in very good agreement with the position in the equatorial plane of the TS estimated theoretically $r_{\mathrm{TS}} = 3 \cdot 10^{17}\,cm$ [71]. Furthermore, recent 2-dimensional [110] and 3-dimensional [116] relativistic MHD simulations suggest that the site of the electrons and positrons acceleration is not the entire surface of the TS, but only the striped-wind section of the TS.

The energy distribution of accelerated particles required to explain the Synchrotron spectrum of the Crab nebula is a broken power-law extending to $E_{\max} \sim 1$ PeV. Low energy particles (radio emitting electrons and positrons) have a distribution $N(\gamma) \propto \gamma^{-1.5}$ and high energy particles (X-ray emitting electrons and positrons) have a distribution $N(\gamma) \propto \gamma^{-2.2}$, where γ is the Lorentz factor of the accelerated particles.

It is remarkable that the slope of the particle distribution at high energies is very close to the one produced in the first-order Fermi acceleration process at a relativistic shock front (e.g., [79, 81, 2]). This is a stochastic shock acceleration mechanism in which particles are elastically scattered by magnetic fluctuations and inhomogeneities embedded in the flow both upstream and downstream of the shock. These particles cross the shock multiple times, gaining energy at each cycle. The increase in energy is of the order of the speed of the shock (hence the name first-order acceleration) and results from the fact that energetic particles do not interact with the shock, which they only perceive as a discontinuity in the flow, but they sample the different speed of the upstream and downstream fluids. This acceleration process is thus only important for non-thermal, pre-accelerated particles whose gyro-radius is much larger than the shock thickness. The particle energy distribution naturally builds up in a power-law because of the competition between the energy gain at every cycle and the probability of escaping downstream of the shock. Both the energy gain per cycle and the escape probability are independent of the particle energy, the former depending only on the shock speed, the latter depending on the velocity of the downstream flow.

At perpendicular shocks, like the pulsar wind TS, this process is normally thought to be inefficient for magnetisa-

---

[1]This structure can also be referred to as electromagnetically modified shock, in analogy with the Cosmic Ray modified shock structure [47].

tions $\sigma \gtrsim 10^{-3}$ [124], since particle trajectories are connected to magnetic field lines which, in the downstream, are effectively advected away from the shock. This strongly decreases the chance of re-crossing upstream inhibiting Fermi acceleration, unless strong cross-field diffusion is allowed.

Other scenarios have been suggested to explain efficient particle acceleration in PWNe. One possibility is Shock Drift Acceleration (SDA) [17]. In this process, a particle gains energy as its gyro-centre makes one single crossing of the shock front from upstream to downstream and in so doing drifts in a direction parallel (or anti-parallel) to the electric field. Particles cross the shock front a finite number of times (the process is not stochastic) and receive a boost in energy that is independent of their initial energy. As a consequence, the spectrum downstream of the shock of particles accelerated via SDA has the same shape of the injection spectrum upstream, which is shifted to higher energy (if the injection spectrum is a power-law, the spectral index does not change). Another possibility is that the acceleration of electrons and positrons in the pulsar wind is triggered by the reconnection of the magnetic field lines driven by the encounter of the wind with the TS (e.g., [114, 125]). It has been shown with 2-dimensional Particle-In-Cell simulations [125] that the reconnection of the magnetic field forms islands of plasma which then coalesce until the dissipation of the alternating components of the magnetic field (and consequently of the striped configuration of the flow) proceeds to completion[2]. In between neighbouring islands, the reconnection electric field is able to accelerate particles. The average particle energy in the downstream is increased by a factor of σ, as expected for full dissipation of the Poynting flux. For values of the pair multiplicity κ and of the size of the TS reasonable for PWNe, the spectrum of accelerated particles is a Maxwell-like distribution peaked at $\sim \Gamma(\sigma + 1)$ and a power-law tail of high energy particles is not obtained.

The Fermi process is thus still a good candidate to produce the distribution of particles required to explain the Synchrotron spectrum of the Crab in the X-ray band. However, if Fermi acceleration is indeed responsible for the electrons and positrons acceleration, another problem to cope with is the injection problem. The injection is the process through which a fraction of the particles in the plasma is decoupled from the rest of the fluid and energised until the particle gyro-radius is much larger than the thickness of the shock. For non-relativistic shock fronts, meandering magnetic field lines [58, 59] or whistler waves [123, 119] are held responsible for the injection of electrons (see Sect. 3.3). Here, we suggest that the dissipation of the Poynting flux at the termination of the pulsar wind mediated by the superluminal waves can produce a turbulent environment where a population of non-thermal electrons (and positrons) can be created and that the turbulence embedded in the flow can sustain Fermi-like acceleration, in particular in the equatorial region of the pulsar wind.

1.4 PWNe in γ-ray binaries

In this work, we are interested in the establishment of the shock precursor as a consequence of the conversion of the striped-wind mode into superluminal waves triggered by its interaction with the TS. Subsequently, we want to study the effects of this structure on the particle acceleration process. We will see in Chapt. 2 that a stable electromagnetically modified shock, able to efficiently dissipate σ, most likely forms when $\omega \gtrsim \overline{\omega}_p$ (or equivalently $R \gtrsim 1$), rather than when $\omega \gg \overline{\omega}_p$ (or equivalently $R \gg 1$). From Eq. 1.17, we can thus deduce that the proper density in the pulsar wind should not be too low. This is the case for isolated pulsars, where the

---

[2]The study is performed for a non-vanishing value of the magnetic field averaged over the length of the stripes, which is supposed to be realistic outside the pulsar equatorial region [125]. This set-up is chosen for the plasma to be magnetised enough to inhibit Fermi acceleration and focus solely on the acceleration caused by the magnetic reconnection.

pulsar wind is confined by the low pressure exerted by the supernova ejecta and the critical surface at $R = 1$ lies well within the TS (the striped-wind can still convert into superluminal waves, but in the spontaneous regime that we do not investigate in this work) [7]. However, luminous and non-accreting pulsars orbiting a massive star might power PWNe, in which case the interaction of the pulsar with the outflow of the companion reshapes and possibly confines the pulsar wind to densities close to the critical value. This is one of the possible paradigms which have been proposed to model the class of astrophysical sources known as γ-ray binaries[3]. These systems are composed of a compact object and a massive star and they are distinguished by the dominant radiative output (of non-stellar origin) in the γ-ray band $\gtrsim$ MeV (see [49] for a complete review). At the moment, five sources are categorised as γ-ray binaries, namely PSR B1259-63, LS 5039, LS I +61°303, HESS J0632+057° and 1FGL J1018.6-5856. PSR B1259-63 is the only γ-ray emitting binary known to host a pulsar [65, 66], which makes the pulsar wind nebula scenario particularly compelling. The picture is the following. A pulsar and its PWN orbit a massive ($M_\star = 10 - 20 \, M_\odot$) main sequence star whose surface temperature is $T_\star \sim 2 - 4 \times 10^4 \, K$. The luminosity of the massive companion is large enough to drive a strong radiation-driven stellar wind with supersonic speed of $v_w \sim 2 \times 10^3 km \, s^{-1}$ and mass-loss rate in the range $\dot{M}_w \sim 10^{-8} - 10^{-6} \, M_\odot \, yr^{-1}$. This wind is highly anisotropic and probably forms an excretion disk in the equatorial plane of the star. The morphology of the TS and subsequent nebula are strongly influenced by the interaction with the companion wind. This depends on the pressure balance between the two winds, which is parametrised by

$$\eta = \frac{L_{\rm SD}}{c\dot{M}_w v_w} \tag{1.23}$$

which is the dimensionless ratio of momentum fluxes (e.g., [25]). The impact of the outflows creates two shocks, terminating the pulsar and stellar winds respectively, separated by a contact discontinuity. This region has a bow-like shape pointing towards the object with the lower dynamic pressure. Normally, $\eta = 0.1$ (implying $\dot{M}_w \sim 10^{-8} \, M_\odot$) is assumed to be appropriate for γ-ray binaries [139, 25, 51], meaning that the bow-shock is always bent in the direction of the pulsar. This also means that the termination shock is much closer to the pulsar than in the isolated pulsar case, because of the larger ambient pressure. Given that the distance between PSR B1259-63 and its companion varies between $l_p \sim 10^{13} \, cm$ at periastron and $l_a \sim 10^{14} \, cm$ at apastron, the location of the TS is $r_{\rm TS} < 10^{14} \, cm$, i.e., much smaller than what is found for the Crab[4].

The emission at GeV and TeV energies observed in these objects is supposed to be mainly produced in the apex of the bow-shock, where electrons and positrons efficiently accelerated at the pulsar wind TS upscatter via Inverse Compton scattering stellar or disk photons to high energies (e.g., [97, 77, 50]). The light-curve in these bands shows a large degree of variability and modulation due to the orbital motion [60]. This is caused by a combination of two phenomena: (1) the flux of target photons decreases when the distance between the stars increases; (2) the emission via Inverse Compton scattering depends on the angle between the directions of the target photon and of the scattering electron, making some locations on the orbit more favourable for observation from Earth [13].

We argue that for PWNe in γ-ray binaries, the orbital motion plays a crucial role in the conversion of the striped-wind wave into a superluminal mode. In fact, the density in the pulsar wind is modulated along the orbit because of the interaction with the strong wind of the massive companion. The conversion can be triggered at the TS when the pulsar frequency is above the cut-off frequency, condition that is probably met not in correspondence of the periastron, where the action of the confining wind is stronger, but away from it.

---

[3]The other possible paradigm for the explanation of γ-ray binaries is the micro-quasar scenario, in which the compact object accretes matter from the companion; we do not discuss this scenario in this work.

[4]$r_{\rm TS}$ would be even smaller for LS 5039 and LS I +61°303° if they were pulsars, because of their orbital parameters [49].

1.4.1   The case of PSR B1259-63

The scenario of conversion of the striped-wind into superluminal waves is particularly appealing for PSR B1259-63. In this binary system, the radio pulsar of frequency $\omega \sim 131\ Hz$ orbits the massive Be star SS 2883 in $\sim$ 1237 d [64, 108]. The orbit is highly eccentric ($e = 0.87$, [65, 66]) and the distance between the two stars varies by a factor larger than ten between periastron and apastron. The multi-wavelength picture is strongly modulated along the orbit and it presents signatures of the colliding wind geometry. Close to apastron, where the interaction between the winds is weak, Synchrotron and Inverse Compton emissions generated from particles probably accelerated at the termination shock between the pulsar and the stellar winds seem to provide a satisfactory explanation of the radio to γ-ray spectrum [132]. Close to periastron, the winds interaction is stronger, in particular with the equatorial region of the stellar outflow. This is normally modelled as a dense disk inclined with respect to the orbital plane (e.g., [66, 64, 35]) through which the pulsar passes twice per orbit and which eclipses the radio pulsation. During these eclipses unpulsed non-thermal emission from radio to TeV energies dominates the spectrum, in agreement with the models of Inverse Compton scattering of stellar and disk photons [77, 74]. The most striking spectral feature is a powerful GeV flare that has been observed for two consecutive orbits about thirty days after periastron passage [1, 131], when the pulsar has supposedly left the putative circumstellar disk. During these episodes, a sizeable fraction of the total pulsar spin-down luminosity is released in the $0.1 - 1$ GeV band [1] without any remarkable spectral or flux variation in any other energy band. Possible explanations involve the following models. Additional target photon fields for Inverse Compton scattering, other than the stellar photon field, can be supplied by the PWN to the shocked electrons and positrons [50] or by the circumstellar disk to the unshocked cold pulsar wind [73, 74]. The re-acceleration of the flow downstream of the pulsar the TS in the tail of the bow-shock structure can Doppler boost the Synchrotron and Inverse Compton emission of shock accelerated particles [91, 90]. The partial or total disruption of the putative circumstellar disk can lead to the formation of an irregular contact surface between the pulsar and stellar winds which traps the unshocked pulsar wind with consequent release of all its energy into this limited region [36]. However, despite the large number of models suggested to explain the GeV flare, a consistent picture seems to be still missing.

1.5   Structure of the thesis

The structure of this thesis dedicated to the study of electron and positron acceleration at the TS in PWNe is the following:

Chapter 2. We introduce the two relativistic fluids (electrons and positrons) model which can describe a pulsar wind, simulated with a magnetic shear wave of frequency ω, and its conversion into superluminal waves under appropriate conditions. We then present the results of the numerical simulation implementing this model obtained for different values of the Lorentz factor Γ_0, magnetisation σ_0 and frequency ω. We analyse the properties of the shock precursor generated by the superluminal waves for different parameters, focusing on the two runs for which we obtain a stationary precursor.

Chapter 3. We investigate the pre-acceleration or injection process of electrons and positrons at the pulsar termination shock. This is done by numerically integrating test particle trajectories in the background electromagnetic fields produced by the two-fluid simulation for the two stationary configurations of the precursor. This approach

determines the reflection probability at the shock, namely the injection probability in a subsequent full acceleration process, and the spectrum and angular distribution of reflected and transmitted electrons and positrons.

Chapter 4. We review the details of Fermi acceleration and we describe the Monte Carlo code used to simulate this process. We address the problem of Fermi acceleration in the equatorial region of the relativistic pulsar wind termination shock (in this region the shock is perpendicular) in different regimes. These are determined by the relative magnitudes of the wavelength of the striped-wind and of the gyro-radius of energetic particles when the scattering length, defined by the degree of magnetic turbulence, is much larger than the wavelength of the stripes. We present the results of our simulations in the form of power-law spectral indexes and angular distributions at the termination shock obtained in the different regimes.

Chapter 5: We apply the physical scenario for particle acceleration developed in the previous chapters to the specific case of the γ-ray binary system PSR B1259-63/SS 2883. We assume that the periodic GeV flare occurring about thirty days after periastron passage is triggered by the conversion of the striped-wind into superluminal waves and by the formation of the shock precursor. Under this assumption, we build a geometrical model to constrain the inclination of the magnetic dipole moment to the pulsar-spin-axis and we estimate the magnetisation, Lorentz factor and multiplicity of the pulsar wind and the density of the plasma at the termination shock. Our estimates of these parameters are compared to the values provided by state of the art theories and simulations of pulsar wind nebulae.

Chapter 6: We summarise the techniques used to investigate the process of electrons and positrons acceleration in PWNe and we draw the conclusions of this thesis.

Appendix A: We illustrate the geometry of the shock front used in the Monte Carlo approach and we present the set of Lorentz transformations of spatial coordinate, time, energy, angle and magnetic field connecting the relevant reference frames in our treatment, namely the upstream, downstream and shock rest frames.

Appendix B: We present the details of the *pitch-angle* scattering technique used in the Monte Carlo code to simulate the presence of magnetic irregularities both upstream and downstream of the shock front.

Chapter 2

Simulation of the Pulsar Wind

Since only very simplified problems related to the physics of pulsars can be solved analytically, numerical methods become fundamental for the investigation of these objects. This chapter is dedicated to the numerical simulation of the relativistic and magnetised outflow powered by a rapidly spinning Neutron Star (NS), in proximity of the wind termination shock (TS). In particular, we study the effects of the conversion of a pulsar striped-wind, simulated as a magnetic shear wave of frequency ω (which is the NS rotational frequency) and characterised by the magnetisation σ_0 and Lorentz factor Γ_0, into electromagnetic waves with superluminal phase speed carrying the same energy, momentum and particle fluxes. To do this we use a two-fluid code developed by [6].

In Sect. 2.1 we introduce the two relativistic fluids (electrons and positrons) model which can support a superluminal wave and reproduce the features of the pulsar wind. The relativistic Magneto-Hydrodynamics (MHD) equations for the two fluids are supplemented by the Maxwell's equations and by a polytropic equation of state for each species to comprise thermal effects in the picture. This constitutes the simplest model capable of describing superluminal electromagnetic waves.

In Sect. 2.2 we present the results of the two-fluid code for different values of frequency, magnetisation and Lorentz factor of the shear wave and we analyse the general properties of the shock precursor formed ahead of the pulsar TS when superluminal waves are launched. We find that the breakout of the precursor always generates a linear expansion phase in which the leading edge of this structure travels upstream with speed χ. In general, the relative magnitude of χ with respect to the superluminal wave group speed determines whether the precursor keeps expanding upstream for the entire simulation, sets up in a stationary state where its extension remains constant with time, or undergoes an oscillation-like phase where its extension alternately expands and contracts. Independently of the evolution of the precursor, the conversion into superluminal electromagnetic waves leads to the dissipation, at least partial, of the Poynting flux carried by the incoming striped-wind. We investigate how the different values of ω, σ_0 and Γ_0 affects the dissipation of the Poynting flux in the shock precursor and how this affects the properties of the plasma.

We find that, in particular circumstances, the forward and backward propagation of superluminal waves in the precursor leads to a steady state of this structure. Section 2.3 describes the detailed analysis of two runs where such a stable state of the shock precursor is achieved, with special focus on the differences in the profiles of the Poynting flux and of the proper plasma frequency. The results obtained in these two specific situations constitute the reference for the following chapters.

2.1   Model

We have seen in Chapt. 1 how, in a Pulsar Wind Nebula (PWN), the combination of electromagnetic fields and electron-positron plasma produced in the magnetosphere propagates outwards in the form of a relativistic wind until the pressure of the outflow is balanced by the ram pressure of the surrounding medium and the wind is terminated by the relativistic termination shock. In the ideal MHD picture, far out the light cylinder $r_{\mathrm{LC}} = c/\omega$, the pulsar wind is described as a series of stripes of toroidal magnetic field of opposite polarity separated by thin sheets of poloidal current (e.g., [71, 41, 105]; see also Sect. 1.1.2). The poloidal component of the magnetic field in the wind drops faster with distance than the azimuthal component (see Eqs. 1.5-1.7), thus for $r \gg r_{\mathrm{LC}}$ the magnetic field in the pulsar wind is predominantly toroidal. The resulting pattern of spatially varying magnetic field in pressure equilibrium in a motionless plasma is equivalent to an electromagnetic wave of wavelength $\lambda = 2\pi c/\omega$ [100] satisfying the frozen-in condition $\mathbf{E} + \boldsymbol{\beta} \times \mathbf{B} = 0$, where $\boldsymbol{\beta}$ is the speed of the wind and $\mathbf{E}$ and $\mathbf{B}$ are the electric and magnetic fields expressed in the lab. frame, respectively. The phase speed of this wave is subluminal $\beta_\phi = E/B < 1$. The misalignment between the magnetic moment and the pulsar spin-axis causes the phase-averaged magnetic field to vanish only in the equatorial plane of the pulsar, while at different latitudes a non-zero average magnetic field is carried by the pulsar wind along with the wave-like component.

In a radial and relativistic wind, however, the density of charge carriers decreases faster than the magnitude of the magnetic field and consequently the wave pattern becomes unstable [105, 93] and the ideal MHD approximation ceases to apply. In this case, new degrees of freedom open up allowing superluminal modes with $\beta_\phi > 1$ to propagate. The condition for the propagation of superluminal waves can be expressed equivalently by $R > 1$ or $\omega > \overline{\omega}_{\mathrm{p}}$, where R is the critical dimensionless radius defined in Eq. 1.15 and $\overline{\omega}_{\mathrm{p}}$, namely the proper plasma frequency, is the cut-off frequency defined in Eq. 1.17. Non-linear solutions for superluminal waves have been obtained for two polarisations, linear and circular, together with the jump conditions ensuring that the superluminal mode carries the same energy, momentum and particle fluxes as the subluminal (or striped) incoming mode [73, 7] (see Sect. 1.2, in particular Eqs. 1.20-1.22 for the circular polarisation). The superluminal wave can remain coupled to the plasma and dissipate the magnetisation into particle energy. The onset of this mechanism is particularly appealing for the dissipation of Poynting flux in magnetically dominated, relativistic flows such as pulsar winds.

The conversion to a superluminal wave can occur in two different scenarios [6]: (1) spontaneously, when the magnetic reconnection proceeds too slowly to maintain the pressure balance between the magnetic stripes and the current sheets required for the evolution of the radial wind; (2) triggered by the interaction of the wind with the termination shock. Scenario (1) is suitable for isolated pulsars since the critical radius beyond which the superluminal modes are allowed lies well within the radius of the termination shock [76, 7]. On the other hand, the orbital motion of PWNe in binary systems might lead the TS to cross R, and scenario (2) occurs. In this work we mainly focus on the latter case.

We consider a sinusoidal, circularly polarised, fully transverse, magnetic shear wave[1] injected into a relativistic, cold two-fluid (electrons and positrons) plasma and forced to interact with a shock. This subluminal wave resembles the striped-wind, except that the current sheet is replaced by a static shear, with $|\mathbf{B}|^2$ = constant. The phase-averaged magnetic field vanishes, so that this wave simulates the pulsar wind in the equatorial plane. The set of relativistic MHD and Maxwell's equations describing the system is supplemented by a polytropic equation of state for each species s to account for the increase of enthalpy of the plasma when particles become relativistically

---

[1]In laboratory plasma physics this mode is known as a 'sheet-pinch' configuration.

hot. The complete set of equations is the following:

$$\frac{\partial}{\partial t}(\Gamma_s \overline{n}_s) + \nabla \cdot (\overline{n}_s \mathbf{u}_s) = 0 \tag{2.1}$$

$$\frac{\partial}{\partial t}\left(\frac{\overline{w}_s}{c^2}\Gamma_s \mathbf{u}_s\right) + \nabla \cdot \left(\frac{\overline{w}_s}{c^2}\mathbf{u}_s \mathbf{u}_s + \mathbf{I}\,\overline{p}_s\right) = q_s \Gamma_s \overline{n}_s \left(\mathbf{E} + \frac{\mathbf{u}_s}{\Gamma_s c} \times \mathbf{B}\right) \tag{2.2}$$

$$\frac{\partial}{\partial t}\left(\overline{w}_s \Gamma_s^2 - \overline{p}_s\right) + \nabla \cdot \left(\overline{w}_s \Gamma_s \mathbf{u}_s\right) = q_s \overline{n}_s \mathbf{u}_s \cdot \mathbf{E} \tag{2.3}$$

$$\nabla \cdot \mathbf{E} = 4\pi\rho \tag{2.4}$$

$$\nabla \cdot \mathbf{B} = 0 \tag{2.5}$$

$$\frac{1}{c}\frac{\partial}{\partial t}\mathbf{E} = \nabla \times \mathbf{B} + \frac{4\pi}{c}\mathbf{J} \tag{2.6}$$

$$\frac{1}{c}\frac{\partial}{\partial t}\mathbf{B} = -\nabla \times \mathbf{E} \tag{2.7}$$

where $\overline{n}_s$, $(\Gamma_s c, \mathbf{u}_s)$, $\overline{p}_s$ and q_s are the proper number density, four-velocity, proper pressure and electric charge of species s, respectively (over-lined quantities are expressed in the comoving frame). The charge density $\rho = \Gamma_p q_p \overline{n}_p + \Gamma_e q_e \overline{n}_e$ and current density $\mathbf{j} = q_p \overline{n}_p \mathbf{u}_p + q_e \overline{n}_e \mathbf{u}_e$ introduce coupling between the fluids and the electromagnetic fields. For the sake of simplicity, we will refer to electrons and positrons as electrons ($q_p = -q_e = e$) and we will drop the subscript e to identify the electron mass. The proper enthalpy density $\overline{w}$ is defined in terms of the ratio of specific heat γ_{pol} (throughout this work we use the value $\gamma_{pol} = 4/3$, appropriate for an ideal gas of relativistic particles)

$$\overline{w}_s = \overline{n}_s m_s c^2 + \frac{\gamma_{pol}}{\gamma_{pol} - 1}\overline{p}_s. \tag{2.8}$$

This equation of state and the expression of the fluids finite temperature $\overline{T} = \overline{p}/\overline{n}$ lead to the definition of an effective plasma frequency

$$\overline{\omega}_p^{eff} = \sqrt{\frac{8\pi e^2 \overline{n}}{mh}} \tag{2.9}$$

where the factor $h = \overline{w}/\overline{n}mc^2 = 1 + \gamma_{pol}\overline{T}/mc^2(\gamma_{pol} - 1)$ is the effective increase of plasma enthalpy. Notice that the factor of $\sqrt{2}$ difference with respect to the definition of proper plasma frequency given in Eq. 1.17 arises because here $\overline{n}$ is the proper number density of electrons, which accounts for half of the total number density of the plasma. The finite temperature effect, expressed by the factor h introduced by [6], is important to account for the fact that the cold incoming wind (see Sect. 1.1.2) is heated up when superluminal waves drive the dissipation of the wind Poynting flux. In the following, we will use $\overline{\omega}_{p0}$ to refer to the proper plasma frequency in the cold fluid and $\overline{\omega}_p^{eff}$ when the correction due to the finite temperature becomes relevant. Analogously, the magnetisation parameter in the cold flow upstream can be defined as

$$\sigma_0 = \frac{B_0^2}{8\pi\Gamma_0 n_0 mc^2} \tag{2.10}$$

where B_0, n_0 and Γ_0 are the magnetic field strength, the electron number density and the wind Lorentz factor far upstream, respectively, as expressed in the lab. frame. A thorough definition of the magnetisation is given instead by

$$\sigma(x) = \frac{c|\mathbf{E} \times \mathbf{B}|}{4\pi \sum_s \Gamma_s \overline{w}_s u_{s,x}} \tag{2.11}$$

which includes the finite temperature correction and does not assume any relationship between **E** and **B**. This definition also accounts for the variation of the magnetisation along the x-axis, the symmetry axis of the simulation. The shock front dividing the incoming pulsar wind on the left-hand side (upstream) from the nebula on the right-hand side (downstream) is a 2-dimensional infinite interface in the yz-plane, whose normal is parallel to the x-axis (see Fig. A.1 in Appen. A for an illustration of the shock geometry).

In the upstream rest frame, which moves along the x-axis with Lorentz factor Γ_0 and speed $\beta_0 = \sqrt{1 - 1/\Gamma_0^2}$ with respect to the shock (laboratory) frame, the magnetic shear is a stationary pattern in which the magnetic field vector rotates in space with constant magnitude. On the other hand, in the lab. frame, the analytic form of the magnetic wave injected in the upstream fluids is the following:

$$B_y = +B_0 \cos(k_0 x - \Omega t) \tag{2.12}$$

$$B_z = -B_0 \sin(k_0 x - \Omega t) \tag{2.13}$$

where the wave frequency $\Omega = \omega/\overline{\omega}_{p0}$ is expressed in terms of the proper plasma frequency and the wavenumber is $k_0 = \Omega/\beta_0 > 0$. The components of the electric field are computed with the frozen-in condition (Eq. 1.3), whereas the transverse four-velocity of electrons is determined by Ampère's law to be

$$u_y = +u_{\perp,0} \cos(k_0 x - \Omega t) \tag{2.14}$$

$$u_z = -u_{\perp,0} \sin(k_0 x - \Omega t) \tag{2.15}$$

where $u_{\perp,0} = cB_0 k_0/8\pi n_0 e$. Since the current density **j** is parallel to the magnetic field, far upstream a force-free equilibrium is defined. The structure of the magnetic shear wave does not affect the density, temperature and bulk flow velocity of the fluids, but it is simply convected in the upstream by the flow itself [6]. The circularly polarised magnetic shear wave constitutes a simplification of the linearly polarised entropy mode containing current sheets usually employed to describe the pulsar wind in the equatorial region. This choice is done under the assumption that the most important physical parameter is the frequency of the wave Ω, rather than its polarisation or functional form, a view that is supported by Particle-In-Cell simulations [125].

The initial conditions in the downstream are found from the Rankine-Hugoniot relations assuming the complete dissipation of the Poynting flux. The relations are:

$$2\overline{n}_1 u_{1,x} = 2\overline{n}_2 u_{2,x} \tag{2.16}$$

$$2\overline{w}_1 \frac{u_{1,x}^2}{c^2} + 2\overline{p}_1 + \left(1 + \frac{u_{1,x}^2}{\overline{\Gamma}_1^2 c^2}\right) \frac{\overline{B}_1^2}{8\pi} = 2\overline{w}_2 \frac{u_{2,x}^2}{c^2} + 2\overline{p}_2 \tag{2.17}$$

$$2\overline{w}_1 \Gamma_1 u_{1,x} + \frac{u_{1,x}}{\Gamma_1} \frac{\overline{B}_1^2}{4\pi} = 2\overline{w}_2 \Gamma_2 u_{2,x} \tag{2.18}$$

where $u_{1,x}$ and $u_{2,x}$ are the x components of the fluid four-speed upstream and downstream of the shock, respectively.

The simulation set-up presented so far is used in a 1-dimensional code [6] whose results show that a well established electromagnetically modified shock precursor forms ahead of the shock when the ratio of the wave (pulsar) frequency to the plasma frequency is $\Omega > 1$. This is due to the fact that $\overline{\omega}_{p0}$ is the cut-off frequency for the propagation of superluminal waves (see Eq. 1.16 and related text for discussion). Figure 2.1 shows the time evolution
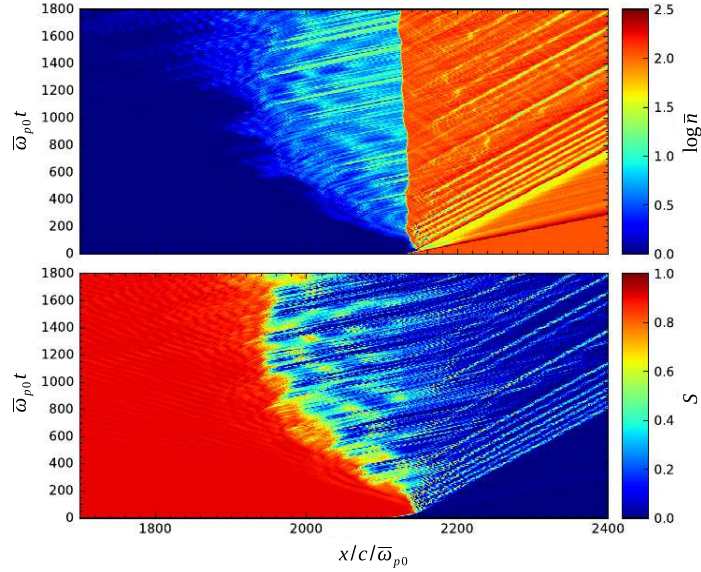
Figure 2.1: Time evolution of the density profile (upper panel) and normalised Poynting flux profile (lower panel) as a function of the spatial coordinate $x/c/\overline{\omega}_{\mathrm{p0}}$, in a region close to the termination shock ($x_{\mathrm{sh}}/c/\overline{\omega}_{\mathrm{p0}} \approx 2140$). The propagation against the flow of superluminal waves creates a shock precursor where the Poynting flux is dissipated. Credits: Amano & Kirk 2013 [6].

of the precursor in the density profile (upper panel) and normalised Poynting flux profile (lower panel) for an upstream Lorentz factor $\Gamma_0 = 40$, magnetisation $\sigma_0 = 10$ and frequency $\Omega = 1.2$ (the definition of the normalised Poynting flux is given in Eq. 2.19). The magnetic shear propagates from the left to the right of the simulation box until it interacts with the shock. When the wave frequency exceeds the proper plasma frequency, the interaction triggers the conversion to superluminal modes which can then propagate either in the positive or negative direction. Forwards propagating superluminal waves are damped in the dense region downstream of the shock, whereas backwards travelling waves can propagate into the upstream until their frequency is larger than the local proper plasma frequency. These waves dissipate the Poynting flux, as they are damped via various instabilities (e.g., [99, 10]), and form an electromagnetic shock precursor which manifests as a region of smooth variation of plasma density, temperature, pressure and four-velocity ahead of the shock. The definition of electromagnetically modified shock is given in analogy with the cosmic-ray modified shock [47], where the structure of the discontinuity is altered by the current of energetic particles (cosmic rays) streaming from downstream to upstream rather than by electromagnetic waves. In particular, a steady state of the shock precursor is achieved in [6] at $\overline{\omega}_{\mathrm{p0}}t \sim 800$ when the size of the precursor stops growing with time.

In the following, we analyse the formation and evolution of this structure for different values of the input parameters Γ_0, σ_0 and Ω, with particular focus on two runs for which a stationary state of the shock precursor is reached.

2.2 Results of two-fluid simulations

In this section we present the results of the investigation of the Γ_0, σ_0 parameter space obtained with the two-fluid code introduced above, but first we need to discuss a technical issue. The magnetic shear wave of frequency Ω, magnetisation σ_0 and Lorentz factor Γ_0 is continuously injected from the upstream boundary of the simulation box. The location of the shock front is chosen to avoid the perturbations created at this location to reach the upstream boundary. These perturbations propagate at the speed of light and are generated in particular for large values of σ_0 and Γ_0. If they reach the upstream boundary within the simulation time, the simulation might become unstable and collapse. Hence, the size of the simulation box and its time duration must be chosen accordingly. On the other hand, the simulation of boxes very extended both in time and space is computationally expensive. Therefore, the dynamic range of the parameters Γ_0 and σ_0 that we can simulate is limited.

The following normalisations are used throughout the discussion: $1/\overline{\omega}_{p0}$ for time, $c/\overline{\omega}_{p0}$ for space, c for velocity, $\overline{n}_0$ for density and $mc^2 \sim 511$ KeV for energy. Here, $\overline{\omega}_{p0} = \sqrt{8\pi e^2 \overline{n}_0/m}$ is the proper plasma frequency in the upstream without the relativistic temperature correction. In these units, the magnitude of the magnetic field far upstream, as expressed in the lab. frame, can be computed from Eq. 2.10 as $B_0 = \Gamma_0 \sqrt{8\pi\sigma_0} (\overline{n}_0 mc^2)^{1/2}$. Given that the value of the proper plasma density far upstream $\overline{n}_0$ is implicitly defined by the expressions for Ω and $\overline{\omega}_{p0}$, in the following we will give the magnitude of the magnetic field in dimensionless units $B_0 = \Gamma_0 \sqrt{8\pi\sigma_0}$.

Each run requires the following set of input parameters:

- the Lorentz factor of the incoming flow Γ_0, pertaining to both electrons and positrons;

- the magnetisation of the incoming flow σ_0;

- the frequency of the magnetic shear wave (pulsar) in units of the proper plasma frequency $\Omega = \omega/\overline{\omega}_{p0}$;

- the proper temperature of the incoming flow $\overline{T}_0$;

- the proper density of the incoming flow $\overline{n}_0$.

Before launching the simulation, the Rankine-Hugoniot conditions (Eqs. 2.16-2.18) are solved for the set of parameters above to obtain the jump conditions for the temperature, density and four-velocity across the shock. For the entire set of runs we performed, we used a constant upstream temperature $\overline{T}_0 = 10^{-2}$ to ensure that the correction h is always very small far upstream. Unless otherwise specified, the standard size and duration of the simulation box are $x [0 : 2000]$ and $t [0 : 1000]$, respectively.

In Tab. 2.1 we summarise the input parameters for the different runs. In the first column we give the identification name of each run. The simulation of different values of Ω requires a further distinction, e.g., RUN D1.2 is the run with $\Gamma_0 = 40$, $\sigma_0 = 10$ and $\Omega = 1.2$. Notice that for all the runs, the upstream flow is supersonic $\Gamma_0 \geq \sqrt{\sigma_0}$.

The reason to perform simulations for different values of Ω lies in the fact that $\Omega = 1$ is the cut-off frequency for the propagation of superluminal waves; $\Omega < 1$ and $\Omega > 1$ thus define two opposite regimes. In the former, the plasma density is large and the non-MHD modes are not allowed to propagate, so that the electromagnetically modified precursor cannot form. In the latter, instead, the plasma density is low enough that superluminal waves can propagate and form the pre-shock in the upstream flow. Moreover, $\Omega = 1.2$ corresponds to a density slightly larger than the critical density and thus to the break-out stage of the precursor, whereas larger values of Ω refer to large radial distances from the pulsar in terms of the dimensionless radius R and thus to a stage in which the propagation of non-MHD mode has long been established.

ID	Γ_0	σ_0	Ω
RUN A	10	10	1.2
RUN B		25	1.2
RUN C		100	1.2
RUN D	40	10	0.4 ,1.2, 2.5
RUN E		50	1.2
RUN F	50	25	1.2
RUN G		100	1.2
RUN H	70	10	1.2
RUN I		50	1.2
RUN J		100	1.2
RUN K	100	25	1.2, 2.5, 3.8
RUN L		50	1.2
RUN M		100	1.2

Table 2.1: Summary of the input parameters for the two-fluid simulations. The first column contains the name of the different runs. Where needed, the value of the frequency is added to the ID.

2.2.1   Linear phase

Independently of the initial set of parameters Γ_0, σ_0 and Ω (as long as $\Omega > 1$) the precursor initially undergoes a phase in which its extension into the upstream grows linearly with time. This can be observed in Fig. 2.2, where the time evolution of the electron pressure profile is shown for RUN C (left panel) and RUN H (right panel). This phase is due to the generation of the superluminal waves at the location of the shock and to their propagation in the negative x direction and subsequent interaction with the incoming magnetic shear wave and damping. From now on, we will use the word shock to refer to the discontinuity in the pressure, density, temperature and velocity profiles (see for example Figs. 2.2, 2.5, 2.11) which can be observed after the region of smooth variation of these quantities, that we call precursor or pre-shock. The location of the shock is approximately at 2/3 of the simulation box. Although the linear expansion phase is a feature of each and every simulation we performed, the way this phase ends strongly depends on the initial parameters. We found three possible fates in our sample.

In the first case, represented by RUN C and RUN H in Fig. 2.2, the precursor expands in the upstream for the entire duration of the simulation ($t = 1000$). For RUN C and RUN D2.5 the simulation time has been extended to $t = 2000$ (the size of the box has been increased accordingly) to understand whether the fact that we do not observe the end of the linear phase is due to the limited time range. Instead, for these two specific runs, the leading edge of the precursor keeps moving in the negative x direction, as it is shown in the left panel of Fig. 2.3 for RUN D2.5. The runs manifesting this behaviour are RUN A, RUN B, RUN C, RUN D2.5, RUN H, RUN K2.5 and RUN K3.8. It is conceivable that there are situations in which the damping of superluminal waves proceeds very slowly and/or the heating of the plasma driven by the superluminal waves, and consequently the decrease of the value of the proper plasma frequency, allows their propagation further upstream. In this case, the extension of the precursor keeps growing with time. Hence, to observe the end of the linear phase, simulation boxes very extended both in time and space are required, to avoid perturbations to reach the upstream boundary as discussed above. In fact, the perturbations propagating upstream can reach the upstream boundary of a small simulation box and cause the simulation to collapse or be reflected, as can be seen in the top left corner in the left panel of Fig.
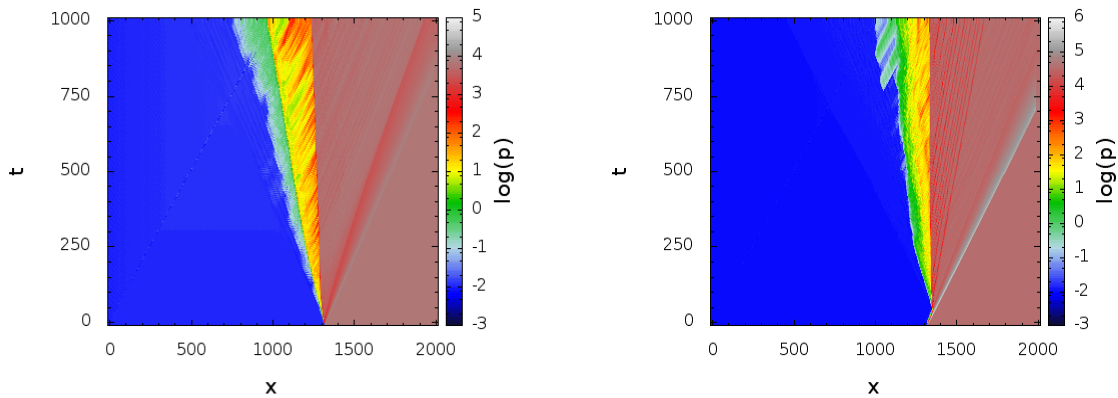
Figure 2.2: Time evolution of the electron pressure profile for RUN C (left panel) and RUN H (right panel).
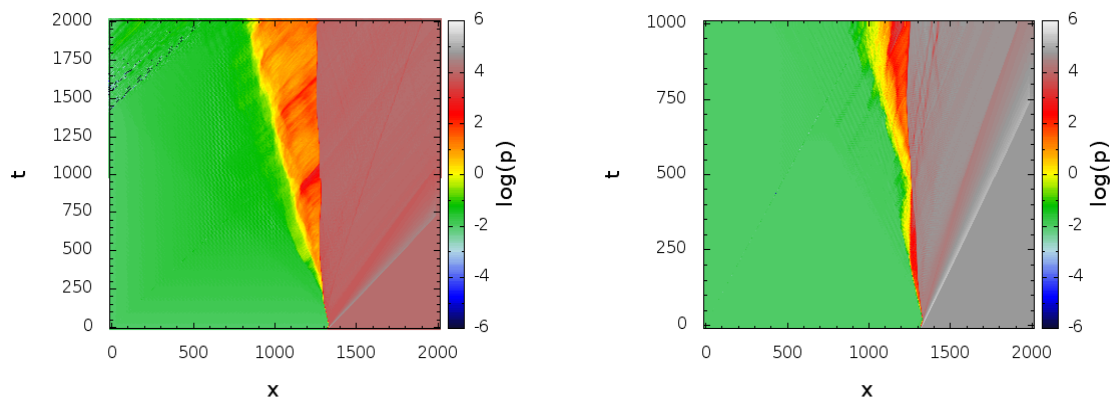
Figure 2.3: Time evolution of the electron pressure profile for RUN D2.5 (left panel) and RUN E (right panel). In the left panel the linear phase is shown to last until $t = 2000$. In the right panel we show the oscillation-like profile of the precursor.

2.3. The reflection would affect in a non-trivial manner the structure of the pre-shock. However, the computation time needed for the simulation of large time and space ranges is prohibitive, so we limit our analysis to those runs in which the linear phase ends in the time frame $t = 1000$.

A more complex behaviour is exhibited in the second case, visible in the right panel of Fig. 2.3 for RUN E, which is representative of more turbulent runs. These are RUN E, RUN F, RUN G, RUN I, RUN J, RUN L and RUN M. Here, after a very short linear phase lasting about $\Delta t \sim 250$, the precursor shrinks and then expands again in an oscillation-like pattern. This might be due to a very efficient damping of the non-MHD waves in proximity of the shock which leads to a decrease of the pressure gradient established by the superluminal waves. At this stage, the pressure is not able to sustain the precursor region, which is then reduced in size before a new expansion phase. The third and last possibility is that the linear phase ends when the precursor achieves a steady state, in which its leading edge stops propagating upstream of the shock and its extension remains constant with time. This regime is appealing for studying how the electromagnetically modified region affects particle trajectories and possibly triggers efficient particle acceleration, in particular when this phase lasts for a long period compared to the wave period. We find that the steady state is achieved for RUN D1.2 and RUN K1.2, which we present in Sec. 2.3.

2.2.2 Precursor growth-rate

We define the dimensionless precursor growth-rate $\chi = dL/dt$, where L is the extension of the precursor upstream, as the magnitude of the slope of the linear phase discussed in the previous section. The growth-rate, which is the speed of the leading edge of the pre-shock in the upstream, is of course limited to be less than unity, where $\chi = 1$ identifies a precursor expanding in the upstream at the speed of light. We compute χ fixing dL to the maximum extension reached by the precursor and using the corresponding dt. For the runs where a precursor steady state is achieved, which we refer to as *stable*, the computation of χ is straightforward. On the other hand, for the runs where the linear phase does not end within the simulation time, dL is taken to be the extension of the pre-shock at $t = 1000$. We refer to these runs as *linear*. Finally, for the runs undergoing the oscillation-like regime,
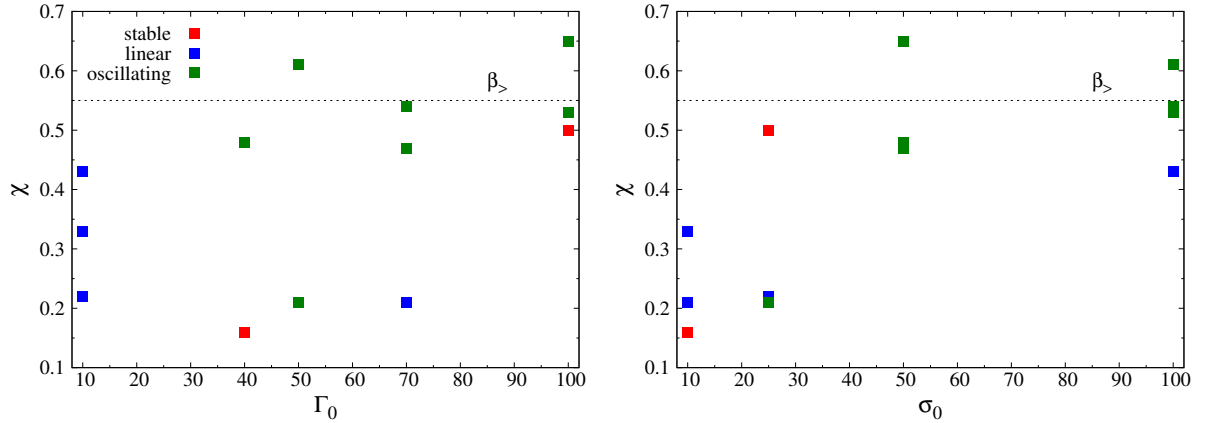
Figure 2.4: Dimensionless precursor growth-rate $\chi = dL/dt$ plotted as a function of Γ_0 (left panel) and as a function of σ_0 (right panel) for the different possible behaviours of the linear phase for runs with $\Omega = 1.2$.

we measure dL at the end of the first linear expansion. We refer to these runs as *oscillating*. We measure χ for the complete sample of runs in Tab. 2.1 with $\Omega = 1.2$ and we plot it in Fig. 2.4 as a function of Γ_0 (left panel) and σ_0 (right panel) for the different categories. We compare the values of the precursor growth-rate with the group velocity $\beta_>$ of a superluminal wave in the ideal case in which the incoming magnetic shear is fully converted into this non-MHD mode. The superluminal wave group velocity corresponds to the velocity of the H-frame [7, 107] which we introduced in Sect. 1.2. The related Lorentz factor $\Gamma_>$ appears in the dispersion relation Eq. 1.16. Hence, comparing this relation with the definition of Ω, we obtain $\beta_> = \sqrt{1 - 1/\Omega^2}$. In Fig. 2.4, $\beta_>$ is plotted as a horizontal black dashed line.

Although we could investigate a narrow dynamic range of parameters, a general trend emerges where *stable* and *linear* runs have $\chi < \beta_>$ and *oscillating* runs have $\chi \sim \beta_>$. Given that the precursor is observed as a gradient in the pressure profile due to the dissipation of the Poynting flux, $\chi \sim \beta_>$ means that the region where superluminal waves are efficiently damped expands almost as rapidly as the region where these waves can propagate. The superluminal wave can thus be completely damped shortly after being generated (see the first oscillation of the precursor in the right panel of Fig. 2.3). If this happens, the pressure gradient associated to the damping of the superluminal waves at the leading edge of the precursor decreases and cannot sustain the precursor itself. Consequently, the preshock shrinks until the magnetic shear interact again with the shock front, which is the mechanism triggering the conversion to superluminal waves in the first place. At this stage, a new expansion phase of the precursor can start. On the contrary, when $\chi < \beta_>$ the damping of the superluminal waves is probably less efficient than in the previous situation so that the non-MHD modes can propagate further into the upstream creating a wide region where the Poynting flux is dissipated. In this sense, the value of χ is a rough indicator of the superluminal waves damping efficiency.

The points in Fig. 2.4 must be intended to have large error bars, because of the method used to measure χ. However, this estimate allows us to say that *oscillating* runs tend to accumulate at large values of Γ_0 (left panel of Fig. 2.4) and, more prominently, at large values of σ_0 (right panel of Fig. 2.4). This means that large wind magnetisation might lead to rapid damping of superluminal waves, albeit a more intense investigation of the σ_0, Γ_0 parameter space is needed to strengthen this conclusion.

2.2.3 Extension of the precursor

Even though we are able to define the initial precursor growth-rate, it is much more complicated to estimate the maximum extension of the precursor region ahead of the shock. This is due to the different ways in which the linear phase can terminate, as we discussed above. For those runs entering the oscillation-like regime, the size of the pre-shock seems to be more extended in the second expansion cycle (see right panel in Fig. 2.3). However, it is not clear whether the oscillation leads the precursor to shrink again or to undergo a new linear expansion phase. We are not able to study this situation in detail because of the limited time range. In the same way, the maximum simulation time limits our conclusions concerning the extension of the precursor for the runs whose linear phase lasts for $t > 2000$.

To circumvent these issues and evaluate the extension of the precursor, we plot the electron pressure profile for different values of σ_0 at constant Γ_0 and for different values of Γ_0 at constant σ_0 at $t = 1000$. We do this only for *stable* and *linear* runs. In the left panel of Fig. 2.5 we show the three runs with $\Gamma_0 = 10$, namely RUN A, RUN B and RUN C, whereas in the right panel we show the three runs with $\sigma_0 = 10$, namely RUN A, RUN D1.2 and RUN H (for all runs $\Omega = 1.2$). In these cases, the region where the pressure adjusts from the upstream value $p = 10^{-2}$
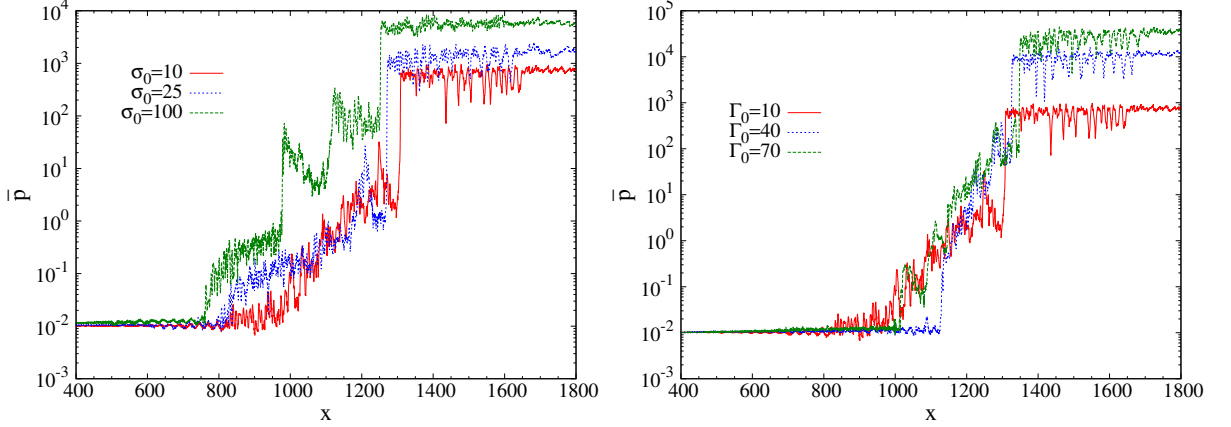
Figure 2.5: Electron pressure profile at $t = 1000$. Left panel: profile at constant $\Gamma_0 = 10$ for RUN A in red, RUN B in blue and RUN C in green. Right panel: profile at constant $\sigma_0 = 10$ for RUN A in red, RUN D1.2 in blue and RUN H in green. All the runs have $\Omega = 1.2$.
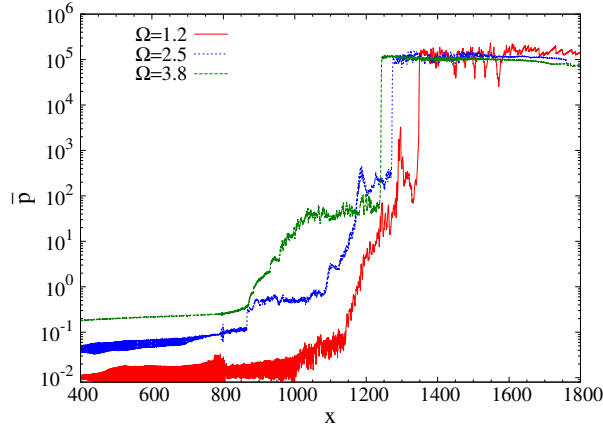
Figure 2.6: Electron pressure profile at $t = 1000$ for different values of the dimensionless frequency Ω at constant $\sigma_0 = 25$ and constant $\Gamma_0 = 100$. We plot RUN K1.2 in red, RUN K2.5 in blue and RUN K3.8 in green.

(set by the initial conditions on temperature and density) to the downstream value is $\Delta x \sim 200 - 500$ wide, where the minimum extension $\Delta x \sim 200$ is for $\sigma_0 = 10$ and $\Gamma_0 = 40$ (RUN D1.2) and the maximum extension is for $\sigma_0 = 100$ and $\Gamma_0 = 10$ (RUN C). The related precursor growth-rates are $\chi_{D1.2} = 0.16$ and $\chi_C = 0.43$, respectively, which explain the different sizes of the pre-shock at $t = 1000$. However, the maximum extension of the precursor is not only determined by the speed at which it expands upstream, but also by the time at which it breaks-out. In fact, we can observe in Figs. 2.2 and 2.3 that the linear phase does not start in all cases at the same time, so

that the same maximum extension of the precursor can correspond to fairly different values of χ. As for the case of the dimensionless precursor growth-rate, our sample is limited to extract a robust dependence of the precursor extension on σ_0 and Γ_0 at constant Ω and a more intense study of the parameter space is needed.

When we set $\Omega = 1.2$, the conversion of the magnetic shear into a superluminal wave occurs for $R \gtrsim 1$, where $R = 1$ is the critical condition for the conversion to take place and the cut-off radius for the propagation of superluminal waves [7]. Consequently, when Ω is small, the obstacle triggering the conversion (in this case the shock front) is close to the cut-off radius, whereas when Ω is large the non-MHD mode is generated further away from $R = 1$. Therefore, in the latter case, we expect the precursor to be more extended than in the former. This is exactly what we observe in Fig. 2.6, where the pressure profile is plotted for different values of Ω at constant $\sigma_0 = 25$ and $\Gamma_0 = 100$ (this corresponds to RUN K1.2, RUN K2.5 and RUN K3.8). For direct comparison with the plots in Fig. 2.5 we used the same spatial range. Given that the pressure far upstream is set by the initial conditions to be $p = 10^{-2}$, we see that the range Δx needed for the pressure to adjust from the upstream to the downstream values is more extended for larger Ω.

2.2.4   Dissipation of Poynting flux

The most important result obtained by [6] with the two-fluid code also used in this work concerns the dissipation of the Poynting flux carried by the incoming flow into particle kinetic energy. The energy transfer is mediated by the backwards propagating superluminal waves interfering with the subluminal mode. As already said, these non-MHD waves are generated in the interaction between the shock front and the incoming subluminal, magnetic shear wave[2]. When the conversion takes place, superluminal waves become unstable to various types of instabilities (e.g., [99, 10]) which cause their damping. In the present situation, the damping proceeds via stimulated Brillouin scattering which causes the waves to steepen and form small-scale shocks, visible for instance in both panels of Fig. 2.5 as sudden increases of the pressure. In these shocks, the plasma is heated up and in turn a pressure gradient establishes which slows down the incoming plasma and creates the observed shock precursor. Thus, the damping of the superluminal waves causes the dissipation of the Poynting flux carried by the wave itself into plasma kinetic energy.

In Fig. 2.7 we show the profile of the normalised Poynting flux $S(x)$ at $t = 1000$ for different runs which exhibit different behaviours. We define the normalised Poynting flux as the ratio of the wave energy density flux at location x to the same quantity measured far upstream

$$S(x) = \frac{|\mathbf{E} \times \mathbf{B}|}{B_0^2} \tag{2.19}$$

where B_0 is the wave magnetic field resulting from the input parameter of the simulation Γ_0 and σ_0. We notice that in all cases the Poynting flux is continuous across the shock ($x_{sh} = 1300$, represented by the vertical black line), meaning that the electromagnetic fields remain unchanged across it. This satisfies the Rankine-Hugoniot relations for a relativistic shock in an unmagnetised plasma [6]. As a consequence, the frozen-in condition breaks down, $\mathbf{E} \neq -\boldsymbol{\beta} \times \mathbf{B}$, and the MHD approximation is no more valid ($E/B > c$). For RUN A, for which both $\sigma_0 = 10$ and $\Gamma_0 = 10$ are in the low end of the respective ranges, the Poynting flux starts decreasing from $\langle S \rangle \sim 1$ at $x \sim 1000$ and slowly drops until it reaches its minimum value $\langle S \rangle \sim 0$ in the downstream. Given that the fields are highly

---

[2]As explained in Sect. 2.1, the rotating magnetic pattern of the shear wave is used to simulate the relativistic and magnetised wind launched by a pulsar.
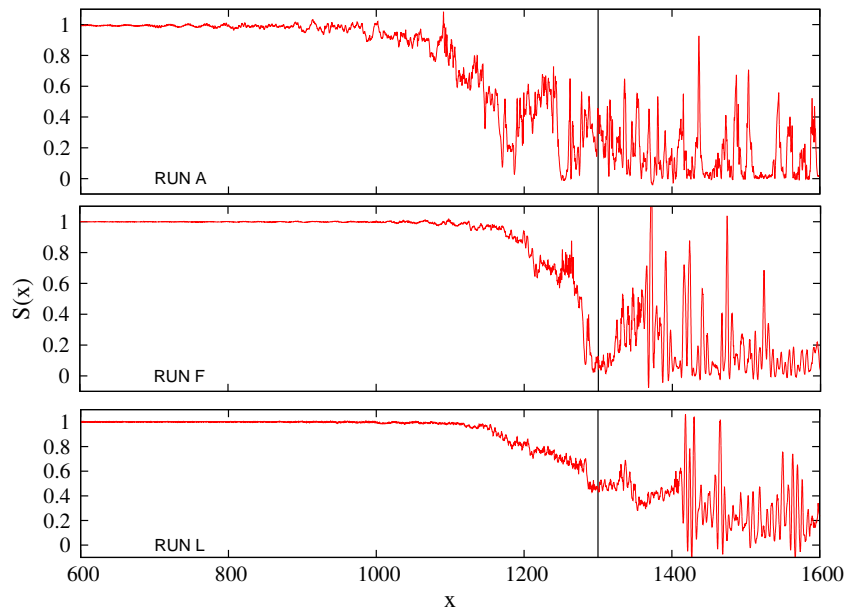
Figure 2.7: Normalised Poynting flux profile at $t = 1000$ for three different runs in the vicinity of the shock front, whose location ($x_{sh} = 1300$) is represented by the vertical black line.

Figure 2.8: Transverse magnetic field (dimensionless) at $t = 1000$ for different runs in a region across the shock, whose location ($x_{sh} = 1300$) is represented by the vertical black line.

Figure 2.9: Temperature profile at $t = 1000$ for different runs in proximity of the shock, whose location ($x_{sh} = 1300$) is represented by the vertical black line.

Figure 2.10: Effective plasma frequency at $t = 1000$ for different runs in proximity of the shock, whose location ($x_{sh} = 1300$) is represented by the vertical black line.

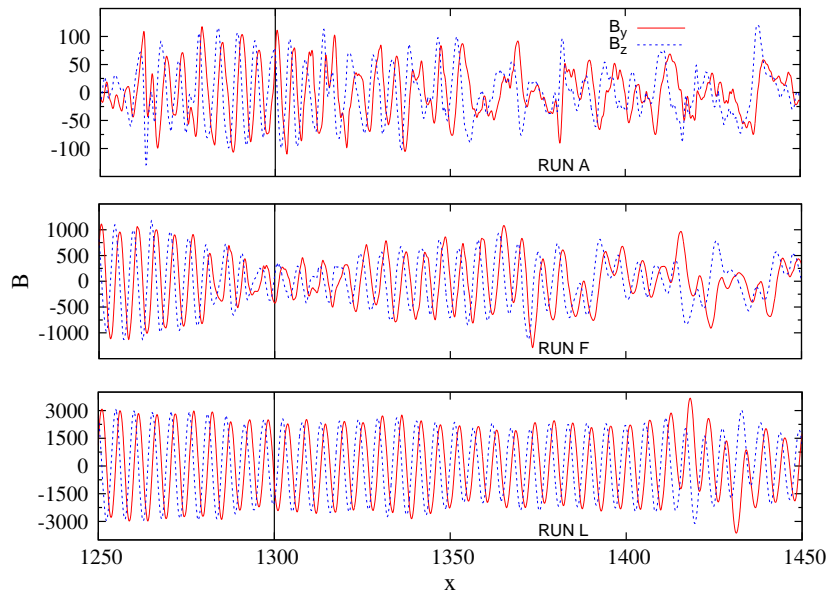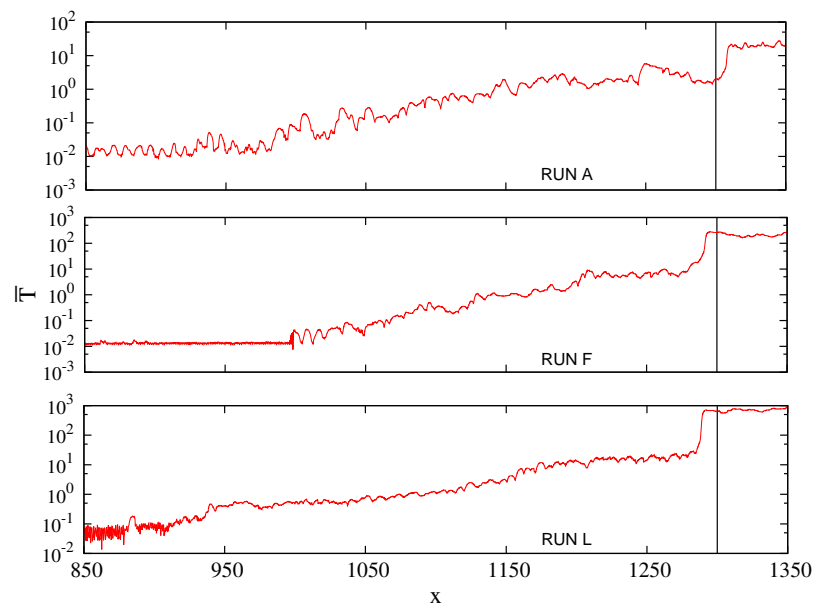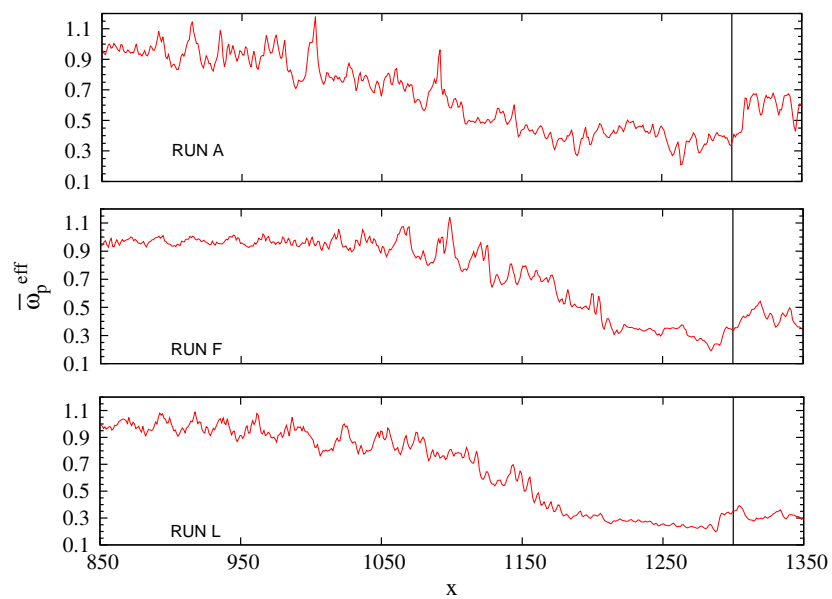turbulent, $\langle S \rangle$ must be understood as the average value about which $S(x)$ oscillates. Far downstream the Poynting flux completely vanishes, but immediately after the shock the electromagnetic fields are very turbulent and any residual of the circularly polarised shear wave is erased by the interaction with the superluminal waves. This can be observed in the upper panel of Fig. 2.8, where the components of the magnetic field are shown in the region across the shock at $t = 1000$. For RUN F, whose parameters $\sigma_0 = 25$ and $\Gamma_0 = 50$ are intermediate, the location where the drop in Poynting flux becomes appreciable is much closer to the shock, at $x \sim 1200$, and the decrease of $S(x)$ is much faster, even though in the downstream there seems to be a residual Poynting flux $\langle S \rangle \sim 0.1$ at $x \sim 1600$. Looking at the central panel in Fig. 2.8, it is clear that a larger portion of the ordered shear field survives in the downstream with respect to RUN A. Finally, for RUN L, whose initial parameters $\sigma_0 = 50$ and $\Gamma_0 = 100$ are more extreme, the Poynting flux starts decreasing at a similar location as for RUN F, but the drop is much smoother and shallower with respect to the previous cases and downstream it shows much less spikes, meaning that the fields are much less turbulent in the precursor and immediately downstream. This is confirmed in the lower panel in Fig. 2.8, where we see that the transverse magnetic field is still predominantly ordered, although $\sim 50\%$ of the Poynting flux has been dissipated at $x \sim 1400$ ($\langle S \rangle \sim 0.5$).

The reason for the observed different behaviours is probably related to the value of the effective plasma frequency. As explained in [76, 7], superluminal waves can be generated only when $\omega > \overline{\omega}_{p0}$, $\overline{\omega}_{p0}$ being the cut-off frequency in the cold fluid (*i.e.*, far upstream). Nevertheless, the conversion of the magnetic energy into particle kinetic energy leads to an increase of the temperature of the plasma, visible in Fig. 2.9 for the three runs considered in this section. This affects the effective plasma frequency, expressed in Eq. 2.9, which is the effective cut-off frequency for the propagation of superluminal waves. When the fluid is cold $\overline{\omega}_p^{\mathrm{eff}} = \overline{\omega}_{p0}$, but $\overline{\omega}_p^{\mathrm{eff}}$ decreases when the temperature increases because of the larger enthalpy of the plasma. This is shown in Fig. 2.10 for a snapshot at $t = 1000$. The profiles of the temperature, as well as those of the effective plasma frequency, are different for the considered runs. For RUN A and RUN F, the temperature at $x = 850$ is very close to the initial value of the temperature $\overline{T}_0 = 10^{-2}$, but the temperature at the shock for the two runs differs by about one order of magnitude. For Run L instead, at $x = 850$ the plasma temperature is already $\overline{T}_0 = 10^{-1}$, which then smoothly increases approaching the shock. This in turn makes the effective plasma frequency for RUN L on average smaller than for the other two runs, meaning that, for the parameters of RUN L, the range of allowed superluminal frequencies in the precursor is larger. Even more important, though, is that for RUN L the profile of $\overline{\omega}_p^{\mathrm{eff}}$ is smoother, with no sudden jumps like those visible for RUN A at $x \sim 1000$ or $x \sim 1100$. The position of these jumps, also visible in the central panel of Fig. 2.10 for RUN F, correspond to the location of the small-scale shocks discussed above (for RUN A this can be checked with the red curve in the left panel of Fig. 2.5). This means that a sharp increase of the pressure causes a sudden drop of $\overline{\omega}_p^{\mathrm{eff}}$. As a consequence, for a superluminal wave propagating leftwards, these peaks of $\overline{\omega}_p^{\mathrm{eff}}$ can prevent it to propagate further upstream by reflecting it again towards the shock. This creates a region ahead of the shock where superluminal waves are trapped and efficiently dissipate the Poynting flux and erase the ordered shear field.

2.3   Precursor steady state

As mentioned previously, for two runs in our sample, namely RUN D1.2 and RUN K1.2, the linear phase ends when the precursor region achieves a steady state during which its extension does not change with time. Given that in the following of this work we discuss particle acceleration in the background fields generated by these two runs, we devote the following sections to present more accurately their features.

2.3.1 RUN D: $\Gamma_0 = 40$, $\sigma_0 = 10$

Simulations for this set of initial parameters have been published in [6]. Here we confirm their findings for an even larger simulation box for $\Omega = 0.4$ and $\Omega = 1.2$ and we extend the comparison to $\Omega = 2.5$.

When the pulsar frequency is smaller than the proper plasma frequency, superluminal modes are not permitted. This means that the structure of the shock is almost the one of a normal relativistic, perpendicular shock where physical quantities suddenly change at the location of the shock front. This is shown by the red curves in the four panels of Fig. 2.11 for $\Omega = 0.4$, where the plasma density, the x-component of the four-velocity, the plasma temperature and the normalised Poynting flux are plotted as a function of the spatial coordinate at $t = 1000$. We notice, however, that a sizeable amount of Poynting flux is dissipated even in this case, meaning that the shock-like discontinuity observed in the plot is not an ordinary MHD shock, where the dissipation of the Poynting flux would be strongly suppressed. This is due to the fact that, even though ideal MHD provides a very good description of the flow both upstream and downstream of the discontinuity, this is not true very close to the discontinuity itself, where large amplitude non-MHD fields can be generated which provide an anomalous resistivity responsible for the drop in Poynting flux, as shown in [6].

When $\Omega = 1.2$, superluminal waves can be generated in the interaction of the shear wave with the shock. This case is plotted with blue curves in Fig. 2.11. The incoming flow is compressed and slowed down by a factor of ~ 10 in the precursor before reaching the shock-like interface. The corresponding increase in temperature results from the combined effect of adiabatic heating and Poynting flux dissipation which starts at the leading edge of the precursor.

The same remarks hold when $\Omega = 2.5$, plotted with green curves in Fig. 2.11, whose frequency corresponds to a

Figure 2.11: From top to bottom, density, x-component of the four-velocity, temperature and normalised Poynting flux profiles at $t = 1000$ as a function of the spatial coordinate for RUN D.

proper plasma density $\sim 77\%$ smaller than for $\Omega = 1.2$, for a fixed value of ω. The major difference between RUN D1.2 and RUN D2.5 is that in the latter the precursor extends much further into the upstream with respect to the former. To investigate this aspect, we plot the effective plasma frequency at $t = 1000$ for the three different wave frequencies in Fig. 2.12. As expected, when $\omega < \overline{\omega}_{p0}$ (red curve), the proper plasma frequency remains unchanged. For $\Omega = 1.2$, instead, the interaction between the flow and the shock triggers the generation of superluminal waves. However, despite the finite temperature effect, the region where they can propagate is limited to a small range of x very close to the shock, delimited by a sharp increase of $\overline{\omega}_p^{\text{eff}}$. Superluminal waves are trapped between this boundary and the dense region downstream of the shock where their propagation is not permitted. This is probably responsible for the achievement of the precursor steady state, which, on the contrary, is not observed when $\Omega = 2.5$. The reason is twofold: (1) the profile of the effective plasma frequency is smooth, so that trapping of non-MHD waves is probably not very efficient; (2) the region where $\overline{\omega}_p^{\text{eff}} < 1$ is much wider for $\Omega = 2.5$, meaning that superluminal modes are allowed very far away from the shock. The effects of point (1) are similar to those discussed during the comparison of RUN A, RUN F and RUN L in Sect. 2.2.4 (see Fig. 2.10). The sharp increase of $\overline{\omega}_p^{\text{eff}}$ in correspondence of small-scale shocks where the incoming plasma is efficiently heated (the sharp spikes in the blue curve in Fig. 2.12) can result in the reflection of the superluminal waves travelling leftwards. This stops their propagation in the upstream and consequently the expansion of the precursor. On the other hand, the smooth profiles of $S(x)$ and $\overline{\omega}_p^{\text{eff}}$ for RUN D2.5 (green curves in Figs. 2.11 and 2.12) suggest that the dissipation of the Poynting flux, although efficient, occurs in a different regime with respect to the previous case, since the fluctuations due to the small-scale shocks are much less pronounced. A detailed spectral analysis of the precursor region, as the one performed by [6], is probably needed to investigate this aspect, which is beyond the scope of this work. As for point (2), this was expected since a large value of Ω corresponds to the fact that the conversion of the subluminal wave into a superluminal wave is triggered at a large value of the dimensionless

Figure 2.12: Effective plasma frequency at $t = 1000$ for RUN D in proximity of the shock ($x_{\text{sh}} = 1380$ for RUN D0.4, $x_{\text{sh}} = 1335$ for RUN D1.2 and $x_{\text{sh}} = 1300$ for RUN D2.5).
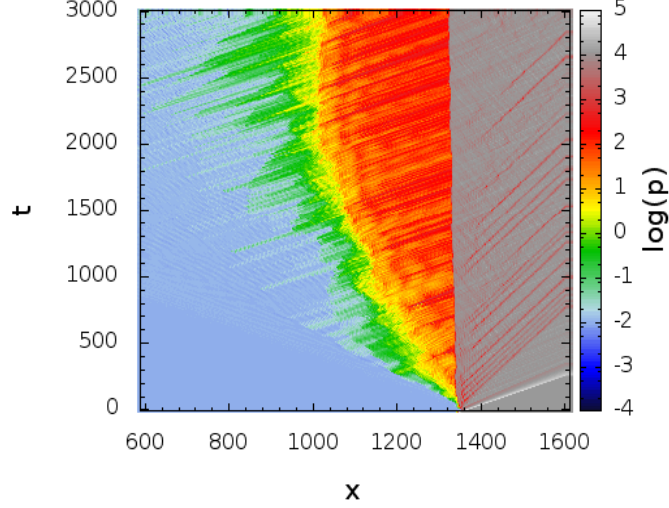
Figure 2.13: Time evolution of the electron pressure profile for RUN D1.2.

radial distance R, rather than at $R \gtrsim 1$ as for $\Omega = 1.2$. Thus, once superluminal waves are generated for $\Omega = 2.5$, they can propagate backwards into the upstream until they reach the cut-off radius $R = 1$, which is much further away from the conversion point than in the case of $\Omega = 1.2$. This effect is even more pronounced for RUN K3.8 (see Sect. 2.3.2 and Fig. 2.15).

In RUN D2.5 the shock precursor expands linearly in the upstream with $\chi_{D2.5} \sim 0.27$ for the entire duration of the simulation ($t = 2000$). This value of χ must be compared with the superluminal wave group velocity $\beta_> \sim 0.92$ for $\Omega = 2.5$. Thus, $\chi_{D2.5} < \beta_>$ in agreement with our conclusions in Sect. 2.2.2 for *linear* runs. On the other hand, for RUN D1.2, the linear phase lasts $\Delta t \sim 1800$ and expands at $\chi_{D1.2} \sim 0.16$ ($\beta_> \sim 0.55$ for $\Omega = 1.2$) until it ends up in a steady state of the precursor lasting for a time interval $\Delta t \sim 1200$. In order to extend the time duration to $t = 3000$, we increased the size of the simulation box to $x\,[0 : 3200]$, to avoid the influence of the boundaries. In Fig. 2.13 we show the time evolution of the electron pressure profile for RUN D1.2.

2.3.2   RUN K: $\Gamma_0 = 100$, $\sigma_0 = 25$

We perform the same analysis carried out for RUN D on RUN K, for which a steady state of the precursor is found for $\Omega = 1.2$. Here, instead of presenting the case of $\Omega = 0.4$, which gives very similar results to RUN D0.4, we focus on $\Omega = 3.8$, which corresponds to a proper plasma density $\sim 90\%$ smaller than that for $\Omega = 1.2$, for a fixed value of ω. In Fig. 2.14 we compare the density, the x-component of the four-velocity, the temperature and the normalised Poynting flux for the different frequencies at $t = 1000$. Despite the diverse set of initial parameters for RUN D and RUN K, if we compare the curves for the same frequency in Figs. 2.11 and 2.14, we notice that the main trends are the same and that the analysis presented in the previous section holds true, the main difference being the larger extension of the precursor region for RUN K. More complex is the situation for $\Omega = 3.8$, for which
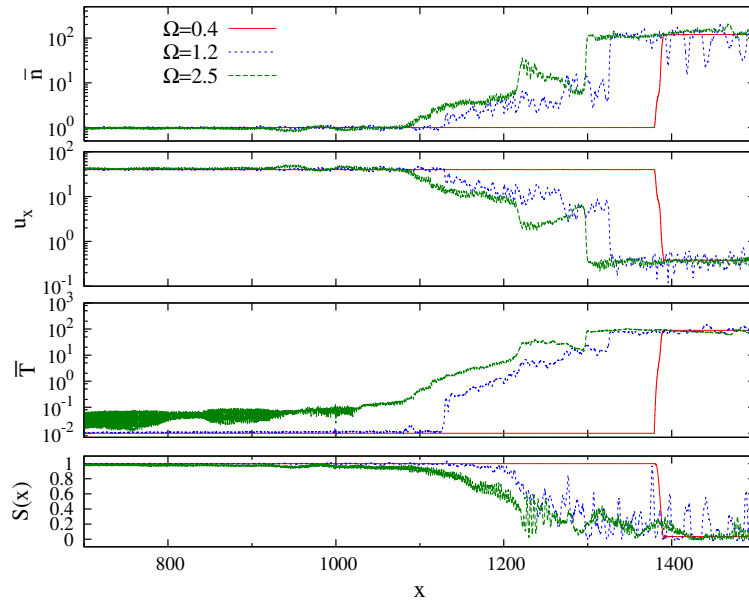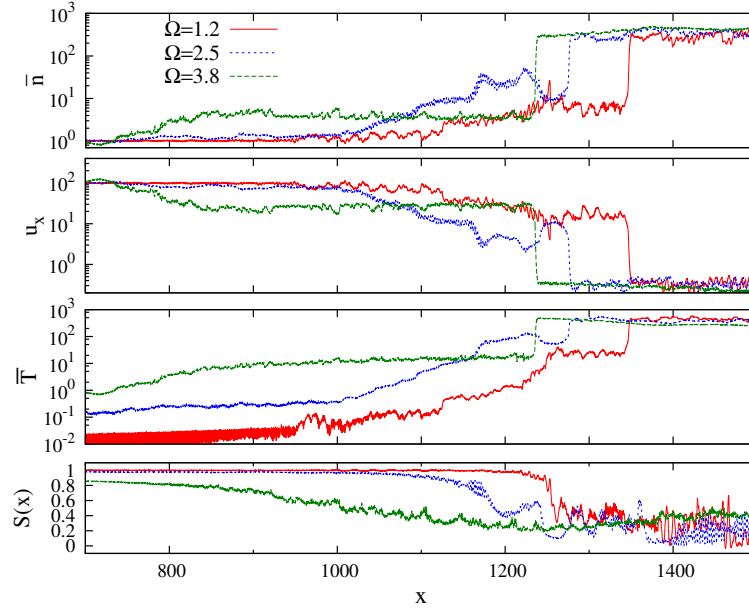
Figure 2.14: From top to bottom, density, x-component of the four-velocity, temperature and normalised Poynting flux profiles at $t = 1000$ as a function of the spatial coordinate for RUN K.

$\overline{n}$, u_x and $\overline{T}$ seem to adjust from the far upstream value to the downstream value into a three steps evolution, *i.e.*, slowly changing up to $x \sim 850$, settling on a *plateau* between $x \sim 850$ and $x \sim 1210$ and then suddenly jumping to the downstream value at the location of the shock ($x_{\text{sh}} = 1240$ for RUN K3.8). In addition, the normalised Poynting flux profile is very shallow for $\Omega = 3.8$, reaching in the downstream $\langle S \rangle \sim 0.4$ at $x = 1500$, meaning that only $\sim 60\%$ of the magnetic energy has been dissipated. Looking also in this case at the effective plasma frequency at $t = 1000$ plotted in Fig. 2.15, we confirm what we found for RUN D, namely that when the frequency of the magnetic shear wave increases (or, equivalently, the conversion takes place at a larger value of R), the profile of $\overline{\omega}_{\text{p}}^{\text{eff}}$ becomes shallower, allowing superluminal waves to propagate much further upstream. This effect is enhanced when Γ_0 and σ_0 are larger, as already suggested by the analysis carried out in Sec. 2.2.4 (see in particular Fig. 2.10).

As a last comparison between RUN D and RUN K, we present in Fig. 2.16 the components of the magnetic field at $t = 1000$ for $\Omega = 1.2$ and $\Omega = 3.8$, in a region across the shock (notice that the location of the shock is different for the three runs, see caption of Fig. 2.16). In the top panel we observe that the shear wave pattern is erased in RUN D1.2 and that the field is highly turbulent in the downstream. For RUN K1.2, in the middle panel, the magnetic field is instead still ordered to some extent. This is in agreement with the level of Poynting flux which is dissipated in the two runs at $x = 1400$, which is ~ 0.8 for RUN D1.2 and 0.7 for RUN K1.2, as can be seen looking at the bottom panels in Figs. 2.11 and 2.14, respectively. On the contrary, for RUN K3.8 (bottom panel in Fig. 2.16) the field downstream is predominantly ordered, which justifies the large value of $\langle S \rangle$ in the bottom panel in Fig. 2.14 for this run.

The above analysis suggests that not only the generation and propagation of superluminal waves are fundamental for the efficient dissipation of the Poynting flux and the formation of a steady precursor, but also their trapping in
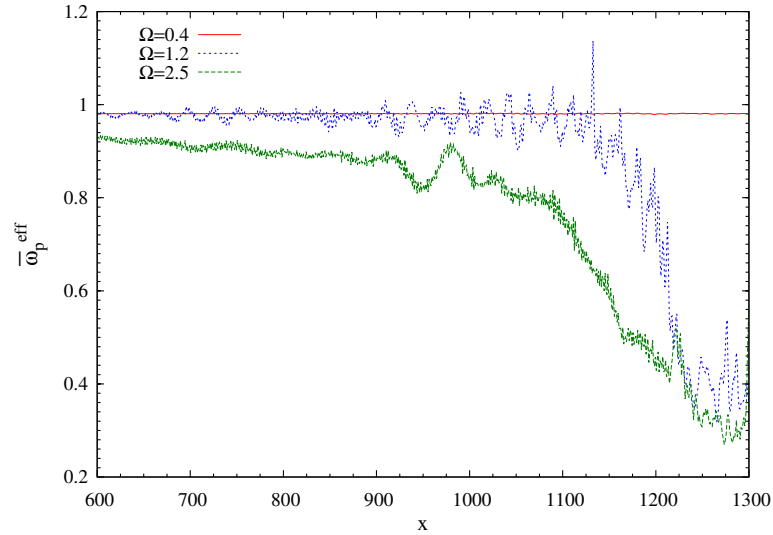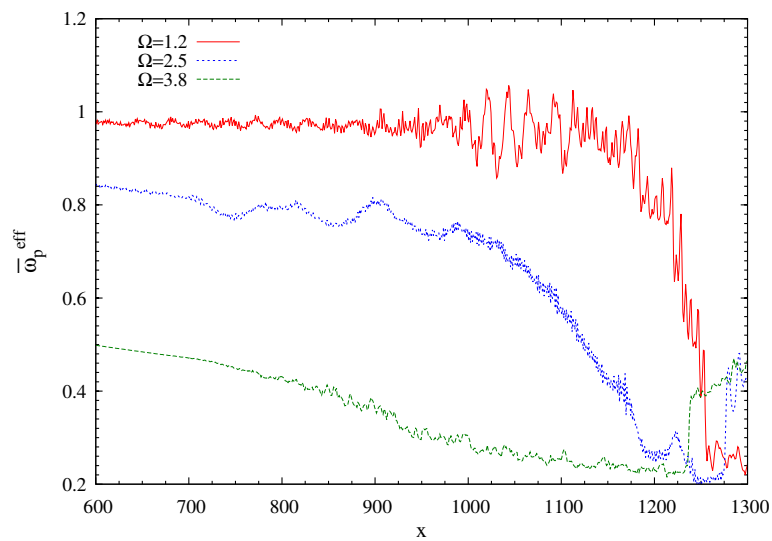
Figure 2.15: Effective plasma frequency at $t = 1000$ for RUN K in proximity of the shock ($x_{sh} = 1335$ for RUN K1.2, $x_{sh} = 1280$ for RUN K2.5 and $x_{sh} = 1240$ for RUN K3.8).
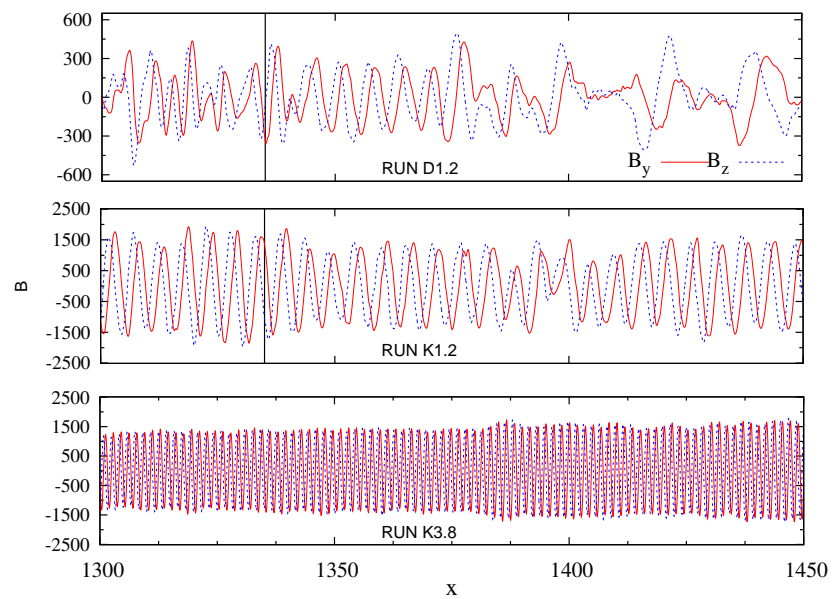
Figure 2.16: Transverse magnetic field at $t = 1000$ for different runs in a region across the shock, whose location for RUN D1.2 and RUN K1.2 $x_{sh} = 1335$ is represented by the vertical black line. For RUN K3.8 ($x_{sh} = 1240$) we focus instead on the downstream region for direct comparison with the other two runs.
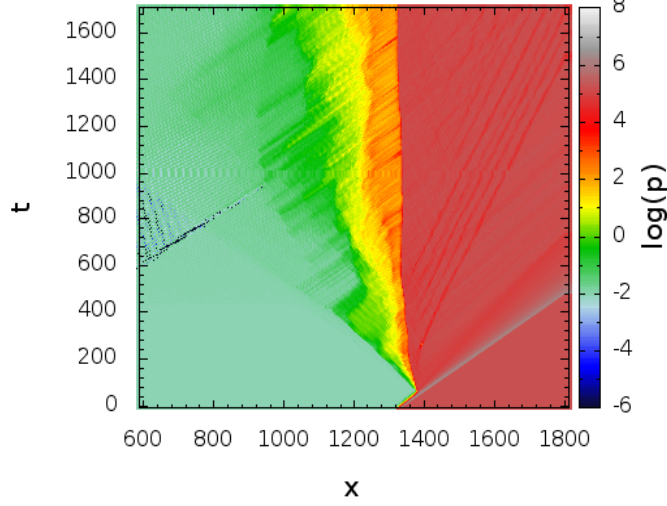
Figure 2.17: Time evolution of the electron pressure profile for RUN K1.2.

a region close to the shock. This follows in particular from what we show in Figs. 2.12 and 2.15. For $\Omega = 1.2$, the $\overline{\omega}_{p}^{eff}$ profile undergoes a steep variation at $\Delta x \sim 100$ from the shock both for RUN D and RUN K, which prevents superluminal waves to propagate further upstream and trap them in the steady precursor. This in turn causes efficient dissipation of the magnetisation of the wave into plasma thermal energy. On the other hand, when the effective proper plasma frequency profile becomes smoother and shallower, superluminal waves can propagate further into the upstream without being reflected back towards the shock front. As a result, the precursor keeps expanding upstream and the wave damping proceeds on a larger length-scale with respect to the low-frequency case. Consequently, the stationary shock precursor state is more likely to form for values of the wave frequency close to the cut-off frequency $\overline{\omega}_{p0}$, rather than for $\omega \gg \overline{\omega}_{p0}$.

Runs RUN K2.5 and RUN K3.8 are both *linear* and their precursors expand with $\chi_{K2.5} \sim 0.41$ ($\beta_> \sim 0.92$ for $\Omega = 2.5$) and $\chi_{K3.8} \sim 0.78$ ($\beta_> \sim 0.96$ for $\Omega = 3.8$) in agreement with the results of Sect. 2.2.2. For RUN K1.2, we obtain a steady state of the precursor for a time interval $\Delta t \sim 1000$ in a simulation with x [0 : 2000] and t [0 : 1700]. The linear phase lasts $\Delta t \sim 700$ during which the precursor expands at $\chi_{K1.2} \sim 0.5$ ($\beta_> \sim 0.55$ for $\Omega = 1.2$). In Fig. 2.17 we show the time evolution of the electron pressure profile for this run. RUN D1.2 and RUN K1.2, for which the stationary state of the shock precursor is achieved, are the benchmark runs for the following chapters.

Chapter 3

Particle acceleration: test-particle approach

The present and the following chapters are devoted to the investigation of the acceleration process of electrons and positrons (henceforth electrons) at the termination shock (TS) in pulsar wind nebulae (PWNe). Our aim is to obtain the steady state energy spectrum and angular distribution of accelerated particles at the location of the shock front. This is achieved in two steps. Firstly, we study the injection process, namely the interaction between electrons and the turbulent fields at the TS during the first shock encounter. This produces a population of pre-accelerated particles which can undergo further acceleration. Secondly, we investigate the details of the following shock crossings, which constitute the full acceleration mechanism (see Chapt. 4).

In this chapter, we focus on the injection mechanism. We implement a test-particle simulation to follow the orbits of a large number of electrons in the background electromagnetic fields modeled with the two-fluid code presented in Chapt. 2. The different configurations of the fields are obtained for various values of the Lorentz factor Γ_0 and magnetisation σ_0 of the incoming flow and of the frequency Ω of the stripes[1]. To reproduce a stationary injection process, we exploit the background fields obtained for RUN D1.2 ($\Gamma_0 = 40$, $\sigma_0 = 10$, $\Omega = 1.2$) and RUN K1.2 ($\Gamma_0 = 100$, $\sigma_0 = 25$, $\Omega = 1.2$), for which a steady configuration of the shock precursor is attained. For both runs, the duration of this configuration is $\sim 1000/\overline{\omega}_{p0}$, which corresponds to a time interval longer than 10^2 pulsar periods.

In Sect. 3.1, we present the set of equations describing the test particle trajectories. The only force acting on these particles is the Lorentz force and since test particles do not feel the fluid pressure, they are decoupled from the fluid. The back-reaction of these electrons on the background fields is neglected under the assumption that the fraction of the total energy carried by the test particles remains limited. In Sect. 3.2, we briefly describe the technique used to numerically integrate the trajectories, which includes a Runge-Kutta method and a 2-dimensional cubic spline routine [117], and in Sect. 3.3, we discuss the initial conditions for initialising the trajectories. The trajectories are followed from the starting point until they reach either one of the two spatial boundaries of the two-fluid simulation box, since the time domain is extended arbitrarily by the implementation of periodic boundary conditions, as presented in Sect. 3.4.

---

[1] $\Omega = \omega/\overline{\omega}_{p0}$ is the wave frequency in units of the proper plasma frequency far upstream, see Sect. 2.2.

The last three sections are dedicated to the detailed analysis of the results of this chapter. From the study of the evolution of typical electron trajectories and related particle energies presented in Sect. 3.5, we infer that electrons gain quite substantial energy in the shock precursor. However, only the turbulent fields surviving in the downstream are able to deflect the particles towards the upstream. In Sect. 3.6 we measure the fraction of trajectories which end up on the upstream boundary of the simulation box and we extrapolate the injection probability at the pulsar wind TS. Finally, in Sect. 3.7 we present the energy spectrum and angular flux of particles transmitted and reflected at the shock front.

3.1   Equations of motion

We only consider trajectories of electrons and positrons, henceforth referred to as electrons, and we neglect heavier ions. This approach is justified by the fact that electrons constitute the bulk of the pulsar wind whereas the ion number density contributes at most $1/\kappa$ to the total number density, where κ is the value of the electron-positron pairs multiplicity in the magnetosphere (see Sect. 1.1.1). If $\kappa \approx 10^1 - 10^5$ as suggested by pair production models (e.g., [8, 62, 63, 135]), ions contribution is negligible both in number and energy density content.
The trajectory is treated classically. The electron is taken to be a point-like particle moving in prescribed external electromagnetic fields, which are provided by the two-fluid code presented in Chapt. 2. Specifically, we use the background fields of RUN D1.2 and RUN K1.2. Although the two-fluid simulation is 1-dimensional and the background fields only depend on the spatial coordinate x, the field components and consequently the trajectories are defined in a 3-dimensional space. Test particles immersed in these fields are only subject to the Lorentz force $\dot{\mathbf{p}} = q[\mathbf{E} + \boldsymbol{\beta} \times \mathbf{B}]$, where q is the electric charge of the particle ($q_p = -q_e = e$, where e is the elementary charge) and $\mathbf{E}$ and $\mathbf{B}$ are the electric and magnetic field respectively. Unlike the fluid elements, test particles do not feel a pressure force, which is assumed to arise from turbulence at small scales that these particles do not see. As a consequence test particles are decoupled from the fluid particles. Energy losses are neglected throughout this work. The straightforward implementation of this force in an algorithm to numerically integrate trajectories might lead to momentum accumulation. With this we mean that, even for a particle moving in a magnetic field with vanishing electric field, the energy would increase because of round-off errors during the numerical procedure. Following [78], we adopt a form of the Lorentz force suitable to avoid this issue:

$$\frac{d\mathbf{n}}{dt} = \pm \frac{e}{m\gamma\beta}\left(\mathbf{E}_\perp + \boldsymbol{\beta} \times \mathbf{B}\right) \tag{3.1}$$

$$\frac{d\gamma}{dt} = \pm \frac{e}{mc}\beta\, \mathbf{n} \cdot \mathbf{E} \tag{3.2}$$

where m, $\mathbf{p} = p\mathbf{n}$ ($p = m\gamma\beta c$) and $\gamma = (1-\beta^2)^{-1/2}$ are the particle mass, momentum and Lorentz factor, respectively, and $\mathbf{E}_\perp$ is the component of the electric field perpendicular to the unit vector in the direction of motion $\mathbf{n}$. Essentially, we split the Lorentz force into one component only affecting the direction of momentum (Eq. 3.1), and one component only affecting the magnitude of momentum (Eq. 3.2). With this form of the equations of motion, when the electric field is null, the magnitude of momentum is less susceptible to error, as it is clear from Eq. 3.2. The set of equations to be integrated also includes $d\mathbf{x}/dt = \boldsymbol{\beta}$, where $\mathbf{x}$ is the position vector. Thus, the advancement of the solution at every time step requires seven equations. Furthermore, the condition $|\mathbf{n}| = \sqrt{n_x^2 + n_y^2 + n_z^2} = 1$ must be fulfilled at all times, adding one degree of freedom for which a dedicated control sequence must be implemented.

This can be avoided transforming to spherical coordinates. Hence, the full set of equations to be solved to describe the trajectory of electrons (including Eq. 3.2) becomes:

$$\dot{x} = \beta \cos \theta \tag{3.3}$$

$$\dot{y} = \beta \sin \theta \cos \phi \tag{3.4}$$

$$\dot{z} = \beta \sin \theta \sin \phi \tag{3.5}$$

$$\dot{\theta} = -\frac{e}{m\gamma\beta} \frac{1}{\sin \theta} \Big[- E_{\perp,x} + \beta \sin \theta \big(B_y \sin \phi - B_z \cos \phi \big) \Big] \tag{3.6}$$

$$\dot{\phi} = -\frac{e}{m\gamma\beta} \frac{1}{\sin \theta} \Big[- E_{\perp,y} \sin \phi + E_{\perp,z} \cos \phi + \beta \big(- B_x \sin \theta + B_y \cos \theta \cos \phi + B_z \cos \theta \sin \phi \big) \Big] \tag{3.7}$$

where θ and ϕ are the polar and azimuthal angles with respect to the x-axis. The components of the electromagnetic fields are still expressed in cartesian coordinates because this is the way they are stored from the two-fluid simulation. Equations 3.6 and 3.7 have two poles for $\theta = 0, \pi$ which can cause errors in the numerical integration if during the evolution of the trajectory one of these two values of the polar angle is met. However, this happens only for $1 - 2\%$ of the trajectories which are then neglected in the following analysis.

3.2   Numerical integration

The set of Eqs. 3.2-3.7 presented above is a system of six coupled first order ordinary differential equations (ODEs) of the kind

$$\frac{dh_i}{dt} = f_i(t, h_1, .., h_6) \quad i = 1, .., 6 \tag{3.8}$$

for the functions h_i in the independent variable t, where the functions f_i are the derivatives of h_i. The easiest way of numerically solving this set is Euler's method (the material in this section is adapted from [117]), which consists in rewriting dh_i and dt in the previous formula as finite steps Δh_i and Δt and multiplying the equations for Δt. This provides algebraic relations for the step in the quantity h_i corresponding to the step in the independent variable t, which are given by

$$h_{n+1} = h_n + \Delta t \cdot f(t_n, h_n) + O(\Delta t^2) \tag{3.9}$$

for the i-th component. The truncation error[2] in Euler's method is of the second order in the quantity Δt. Consequently, the direct implementation of this formula in a computing algorithm is not suitable because it introduces a large uncertainty in the solution at every step of the integration. However, all methods for the numerical integration of ODEs are based on Euler's formula (Eq. 3.9). In this work, we make use of the Runge-Kutta (RK) method to advance the solution of our system of equations of one increment Δt, which combines the information of several Euler-like steps in a Taylor series expansion of the solution up to the fifth order. An adaptive step-size routine is also implemented to keep track of the truncation error at every step. Since the components of the position vector $\mathbf{x}$ are computed using $\boldsymbol{\beta}$, and thus γ, θ and ϕ, we set an accuracy criterion only for these last three quantities, and we require that the truncation error is $< 10^{-3}$. It is worth saying that each step in the procedure is treated

---

[2]The truncation error is the uncertainty introduced by the integration routine assuming the perfect knowledge of the solution at the previous step.

identically, meaning that prior behaviour of the solution does not affect the computation in the following. The RK method is applied to advance the solution of Eqs. 3.2-3.7 from t_n to t_{n+1}. The fifth order algorithm requires eleven independent evaluations of the right-hand side for each equation. Practically, this means that the values of the electromagnetic fields **E** and **B** must be provided to the RK routine every time the right-hand side fs are needed.

In Chapt. 2 we neglected the technical point concerning the way the background fields are stored by the two-fluid code, but now this issue deserves some attention. In the two-fluid simulation, a fixed space-time mesh is defined at which the values of the electromagnetic fields and all other relevant physical quantities (electron and positron pressure, density and velocity) are computed. For the results to be accurate, the mesh must be refined enough, but the rate at which the physical quantities are computed (both in space and time) does not necessarily correspond to the rate at which they are stored in a data file, for obvious reasons of time and computer storage. For the entire sample summarised in Tab. 2.1, the grid size of the simulation is $\Delta x = 0.05$ and $\Delta t = 0.005$, while the grid size of the saved data is $\widehat{\Delta x} = 0.05$ and $\widehat{\Delta t} = 1$. In this chapter we use the same normalisations for space and time that we used in Chapt. 2, namely $c/\overline{\omega}_{p0}$ for space and $1/\overline{\omega}_{p0}$ for time, where $\overline{\omega}_{p0}$ is the proper plasma frequency in the far upstream defined in Sect. 2.1. We define *snapshot* the ensemble of values of all physical quantities stored at every position in the simulation box at a given time $\widehat{t}$. In general, the integration time step computed with the adaptive step-size routine in our code is smaller than $\widehat{\Delta t}$ and consequently the values of **E** and **B** are needed at a time different from the values at the time grid points. The same applies to the spatial coordinate.

To cope with this situation we build two arrays, one for the values of the time component $\hat{t}$ and one for the spatial component $\hat{x}$ at which the background fields are saved by the two-fluid code. Each trajectory starts and evolves on space-time points (t, x) which satisfy $t\,[\hat{t}_n : \hat{t}_{n+1}]$ and $x\,[\hat{x}_n : \hat{x}_{n+1}]$. For each specific point (t, x) of the trajectory, we compute the six components of the electromagnetic fields by interpolating their grid points values, both in time and space, with a cubic spline, which ensures not only the continuity and differentiability of the interpolated function, but also of its first derivative. In addition, the spline method avoids oscillations between grid points, which might occur using high degree polynomial interpolation, making the resulting function smooth. Given that the behaviour of the fields is not particularly pathological, in the sense that they do not show jumps or kinks even in the most turbulent regions, we exploit the grid points in the ranges $\hat{t}\,[\hat{t}_{n-2} : \hat{t}_{n+3}]$ and $\hat{x}\,[\hat{x}_{n-2} : \hat{x}_{n+3}]$, resulting in twelve grid points. We sketch the situation in Fig. 3.1, where the black dots are the grid points and the red dot is the particular point of the trajectory under consideration. The red, dashed line represents the trajectory. It is clear that, if the integration time-step Δt is small enough, the trajectory occupies many points in the plot between $\hat{t}_n$ and $\hat{t}_{n+1}$ and $\hat{x}_n$ and $\hat{x}_{n+1}$. In this case, a new interpolation is performed every time to compute the six components of the fields and to account for their variations over the interval.

We briefly resume the structure of the code which performs the numerical integration of test particle trajectories:

- the RK algorithm – it advances the solution of each dependent variable h_i in Eqs. 3.2-3.7 from h_n to h_{n+1} while the independent variable is incremented from t_n to $t_{n+1} = t_n + \Delta t$;

- cubic spline interpolation – it provides, at each location (t, x), the value of the electromagnetic field components interpolated from twelve grid points values computed with the two-fluid code;

- stepper – it calls the RK routine and, according to a pre-determined accuracy criterion, confirms the step and proceeds to the following phase for t_{n+1}, or rejects the step and reiterate the operation for t_n;

- driver – it starts and stops the integration according to initial conditions (to be defined in the next section) and stores the intermediate results.
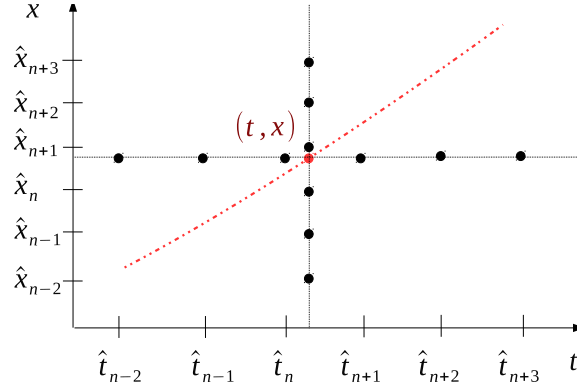
Figure 3.1: Sketch of the 2-dimensional cubic spline method. To interpolate the values of the six components of the fields at the specific space-time point (t,x), a total of twelve grid points is considered.

3.3   Initial conditions

The set of Eqs. 3.2-3.7 must be initialised in order to start a trajectory. The choice of the initial conditions depends on the physical scenario one wants to investigate and is related to the *injection* problem. By this, we mean the mechanism through which some particles are (1) decoupled from the rest of the plasma and (2) energised and driven into the full acceleration process. Point (1) has been addressed in the context of the acceleration of ultra-high energy cosmic rays (UHECRs) at strong shocks in γ-ray bursts (GRBs) by [137]. The author considered that in all collisional processes, like those taking place at astrophysical shock fronts, a Maxwell-Boltzmann distribution of particles likely forms, which extends to very high energies. For particles with energies in the tail of the distribution, the mean-free path between two following scattering events is much larger than that of particles whose energy is $\approx k_B T$, where k_B is the Boltzmann constant and T is the temperature of the fluid. These energetic particles can therefore decouple from the fluid. However, this process is not viable at collisionless shocks like the termination shock of pulsar wind nebulae. In this case, electromagnetic turbulence associated to the formation of the shock front is held responsible for the decoupling of a fraction of the particles from the background plasma (e.g., [122]), although this is probably more efficient for ions than for electrons. In fact, low-energy electrons have too small gyro-radii to resonantly interact with pre-existing magnetic fluctuations or ion-generated waves (e.g., [59]). Alternatively, electrons might be injected in the acceleration process by meandering magnetic field lines which allow them to travel back and forth across the shock and finally to be reflected into the upstream [58, 59]. Another possibility is that electrons are decoupled from the fluid and energised by whistler waves generated at the shock [123, 119]. All these mechanisms are envisaged for non-relativistic shocks.

In the situation considered here, the upstream flow is cold and thermalises in the downstream of an highly relativistic ($\Gamma_0 \gg 1$) shock. The speed of the downstream flow is still $\beta_\mathrm{d} \sim 1/3$ and the plasma is efficiently advected away from the shock. Actually, the efficient advection far away from the shock of the downstream fluid is the objection that is usually raised to argue against relativistic shocks as efficient particle accelerators (e.g., [110]).

In this work, we focus on the investigation of point (2), addressing point (1) with the following approach. We

assume that, in the rest frame of the cold upstream plasma, some particles are not totally at rest, but have a small spread in γ (hereafter Γ_0 identifies the Lorentz factor of the shock, while γ identifies the Lorentz factor of the particles). We also assume an isotropic angular distribution of the test particles in this frame as done in [58]. Although this idea does not really answer the question about the mechanism decoupling some particles from the bulk, at least it does not place any strong constraint on the their initial energy and angular distribution.

Hence, trajectories are initialised in the far upstream, where there is no turbulence and no precursor has established, with $\overline{\gamma}\,[1:1.2]$, $\overline{\theta}\,[0:\pi]$ and $\phi\,[0:2\pi]$ (over-lined quantities are expressed in the upstream fluid frame), according to the prescription given above, where all these quantities are expressed in the upstream fluid frame (for a detailed treatment of Lorentz transformations and the notation in different frames see Appen. A).

3.4 Periodic boundaries

The aim of the numerical integration of test particle trajectories is the investigation of the effects of the turbulent region in the proximity of the shock created by the interaction of the superluminal waves with the incoming pulsar wind. In particular, we want to investigate whether electrons gain energy during the first shock encounter and how many trajectories are reflected at the shock front in a stationary situation. To achieve this, we are not interested in the time dependent phases of the precursor break-out and linear phase presented in Chapt. 2. Rather, we focus on
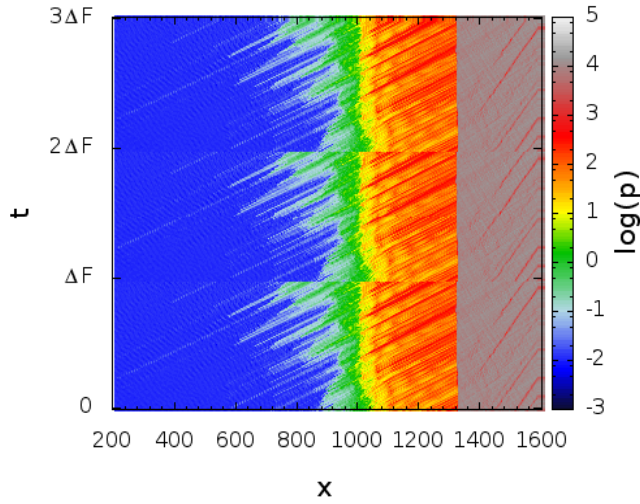
Figure 3.2: Electron pressure profile for an ensemble of time snapshots of period ΔF from RUN D1.2, in which the precursor is steady. The ensemble has been folded for three times to illustrate the implementation of the time domain periodic boundary conditions.

the steady state of the precursor region to study particle acceleration on a time-scale which is long compared to the wave (pulsar) period. In fact, for both RUN D1.2 and RUN K1.2 the duration of the steady configuration is ~ 1000, which corresponds to a time interval longer than 10^2 pulsar periods. However, in this time interval a relativistic particle flying with $\beta \sim 1$ covers a distance $x \sim 1000$, which is limited compared to the size of the simulation box to start trajectories far upstream and study their propagation all the way to the shock region. In order to extend
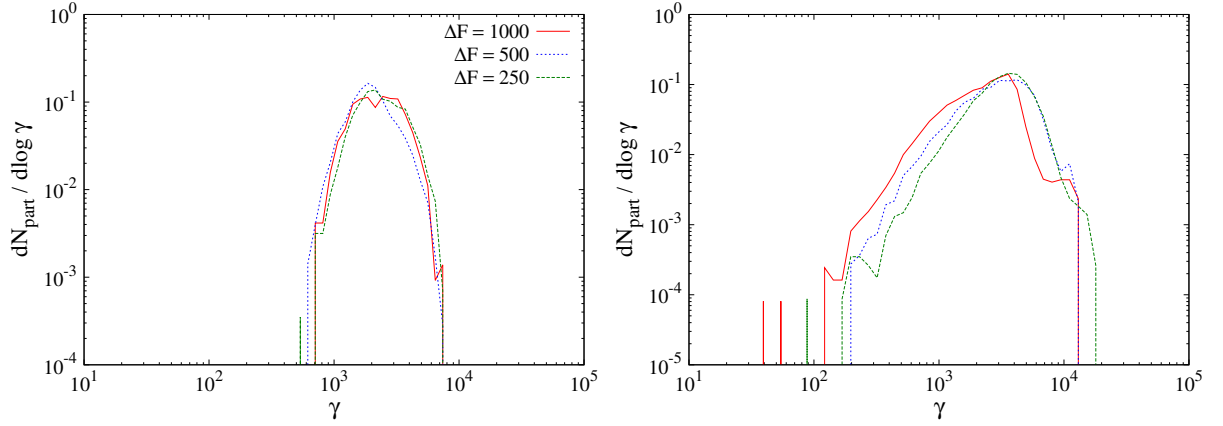
Figure 3.3: Energy spectrum, expressed in the shock frame, of reflected (left panel) and transmitted (right panel) trajectories integrated in the background fields of RUN K1.2 for different periods ΔF.
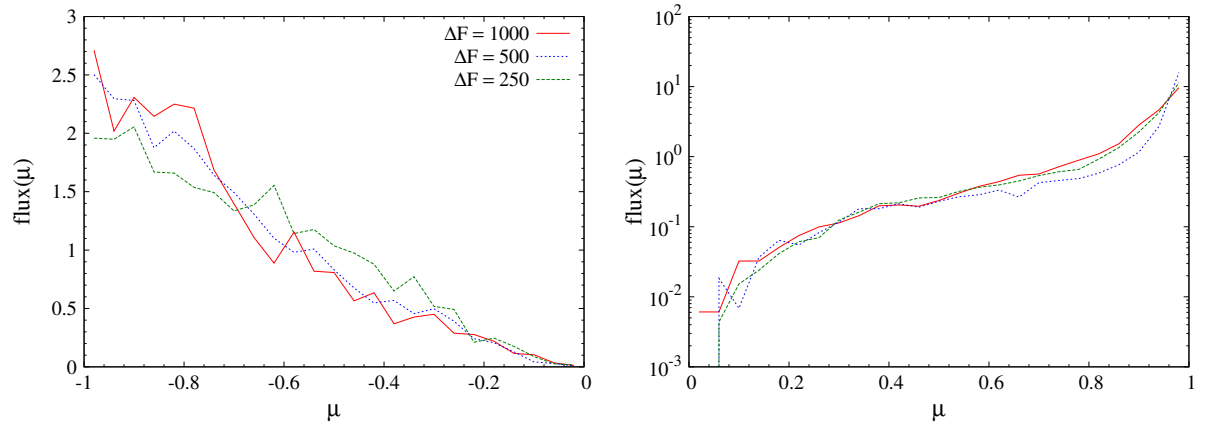
Figure 3.4: Angular flux, expressed in the shock frame, of reflected (left panel) and transmitted (right panel) trajectories integrated in the background fields of RUN K1.2 for different periods ΔF.

the available range of time, we create periodic boundaries in the time domain to reproduce for many foldings the steady state of the pre-shock. This approach is justified by the fact that we believe that the time range over which we observe the steady precursor is limited by the size of the simulation box and not by the physics, so that, in principle, with infinite computing power and storage capability, this structure would last much longer.

Hence, we select an ensemble of time snapshots of period ΔF that we fold for several times. We show the procedure in Fig. 3.2, where the electron pressure profile of the steady state of RUN D1.2 has been folded for three times [3]. Although this technique allows us to study the particle trajectories while they propagate in the background fields for a longer time, it also presents a drawback. In fact, the implementation of the time domain periodic boundaries essentially introduces an artificial wave of period ΔF, which in principle can affect our results. To make sure that the effect of this artifact is negligible, we integrate a large number of trajectories, starting them off with the prescription described in the previous section and following them until they reach either one of the two edges of the simulation box. The upstream and downstream edges of the simulation box are treated as absorbing boundaries removing particles from the simulation. Henceforth, we will refer to electrons absorbed at the downstream boundary as *transmitted*, and to electrons absorbed at the upstream boundary as *reflected*. We do this for different values of ΔF for both runs under consideration and we study the particle spectrum and angular flux, expressed in the shock frame, at the two boundaries. We compute the spectrum $dN_{\text{part}}/d\log\gamma$ binning the Lorentz factor of electrons (that hereafter we use as a synonym of energy) in equally spaced logarithmic bins of γ, integrating over angles and we normalise to the total number of trajectories N stopped at one given boundary. The spectra of reflected and transmitted particles are shown in Fig. 3.3, left and right panels respectively, for three values of ΔF for RUN K1.2 (the results do not differ for RUN D1.2). We obtain the angular flux simply binning $\mu = \cos\theta$ of electrons registered at one of the two boundaries in equally spaced bins of μ, integrating over energy and azimuthal angle. The angular fluxes of reflected and transmitted particles are shown in Fig. 3.4, left and right panels respectively, for three values of ΔF for RUN K1.2 (the results do not differ for RUN D1.2). We plot the angular flux of transmitted particles on a logarithmic scale to improve the resolution for small values of μ, where there are only few particles per bin. In the shock frame, particles travelling towards the upstream (left-hand side of the simulation box) have μ in the interval $[-1:0]$, while particles travelling towards the downstream (right-hand side of the simulation box) have μ in the interval $[0:1]$.

As can be seen from these plots, neither the energy spectrum nor the angular flux show remarkable differences for different values of ΔF. So we feel confident that our approach allows us to extend the range of time over which we can study the evolution of test particles, without imprinting any artificial feature on the energy spectrum and angular distribution. In the following, the benchmark value $\Delta F = 1000$ is used both for RUN D1.2 and RUN K1.2.

3.5   Trajectories and energy

The trajectories of test particles are integrated using the background electromagnetic fields provided by the two-fluid simulation in the runs RUN D1.2 [$\Gamma_0 = 40$, $\sigma_0 = 10$, $\Omega = 1.2$] and RUN K1.2 [$\Gamma_0 = 100$, $\sigma_0 = 25$, $\Omega = 1.2$]. These trajectories are regulated by the interaction with the background electromagnetic fields expressed by the Lorentz force (Eqs. 3.1 and 3.2) and the only difference between the equations of motion of a test particle and a fluid particle is the lack of the pressure term in the test particle case. As a result, test particles are decoupled

---

[3] We remark that we plot the pressure profile because it makes the folding evident, but all the physical quantities of the interested snapshots are folded in the same way.

from the rest of the fluid.

The trajectories are initiated far upstream of the shock, where the ideal-MHD condition (Eq.1.3) holds, and the propagation is followed until they are absorbed at either one of the two absorbing boundaries, placed one upstream and one downstream of the shock. Because of the implementation of the periodic boundaries in the time domain, there is no constraint on the duration of the trajectory from the starting to the ending point. Unless otherwise stated, the absorbing boundaries coincide with the spatial edges of the simulation box. Typical trajectories and the evolution of the respective Lorentz factors are plotted in the left and right panels of Figs. 3.5 for RUN D1.2 and 3.6 for RUN K1.2, respectively, in a region close to the termination shock. Time, position and energy are expressed in the shock frame.

Provided that the trajectories are initiated far upstream of the shock and of the leading edge of the precursor, all trajectories look similar in the early times. If we consider in the upstream fluid frame the initial part of the trajectory, where the frozen-in condition holds, electrons are only subjected to the magnetic field because the electric field vanishes in this frame. Thus, when a trajectory is started with a Lorentz factor slightly larger than unity, the particle starts gyrating about the magnetic field lines. The orbit is not a perfect helix since the field vector is not uniform, rather it rotates in space with constant magnitude. In fact, the pattern of the magnetic field far upstream is a magnetic shear wave, as presented in Chapt. 2. The wavelength of the field is $\overline{\lambda} = 2\pi\beta_0\Gamma_0/\Omega$, where Γ_0 is the Lorentz factor of the upstream fluid, β_0 is the related speed and Ω is the wave frequency in units of the proper upstream plasma frequency (over-lined quantities are expressed in the upstream frame, see Appen. A). On the other hand, the gyro-radius of a quasi-thermal particle with $\overline{\gamma} \gtrsim 1$ is $\overline{r}_g = m\overline{\gamma}/e\overline{B}_0 \propto \overline{\gamma}/\sqrt{\sigma_0} \ll \overline{\lambda}$ since $\overline{B}_0 = B_0/\Gamma_0 \propto \sqrt{\sigma_0}$ as shown in Sect. 2.2. Hence, the deviation of the orbit from a spiral is negligible. The energy remains constant in the upstream frame. The helical motion in the upstream fluid frame causes the particle to move alternately with the bulk, at a slightly larger speed, and against the bulk, as seen in the shock frame. This produces the *bouncing* behaviour of γ in the early times of the trajectories (see right panels in Figs. 3.5 and 3.6). In particular, the kinks of the particle Lorentz factor, dropping to $\gamma \sim 1$, are due to the nearly perfect anti-parallel motion between the test particle and the upstream fluid. The duration of the rising part of the γ profile is much larger than the decreasing part because the bulk speed is ultra-relativistic ($\Gamma_0 = 40$ for RUN D1.2 and $\Gamma_0 = 100$ for RUN K1.2) and the range of directions $\overline{\mu}$ for which the Lorentz factor in the shock frame diminishes is limited (see App. A).

Between the leading edge of the pre-shock and the shock, the frozen-in condition ceases to be valid and the fields become turbulent because of the presence of the superluminal waves interfering with the pulsar wind. Here, electrons are scattered by the turbulence and gain energy. The fate of the test particles is well represented in the plots in the left panels of Figs. 3.5 and 3.6: they can either fly across the shock and reach the downstream boundary (transmission) or scatter off electromagnetic waves and reach the upstream boundary (reflection). Both scenarios can proceed smoothly, with very few changes of sign of $\dot{x}$ (total deflections), e.g., trajectory n. 2 in Fig. 3.5 and trajectory n. 3 in Fig. 3.6, or undergoing many total deflections, e.g., trajectory n. 3 in Fig. 3.5 and trajectory 1 in Fig. 3.6. From the examples reported here, it is clear that most of the energy is gained in the precursor and most of the deflection occurs in the turbulent post-shock region (see Figs. 2.11 and 2.14 in Chapt. 2 and related discussion). However, it is possible that particles cross the shock many times, being deflected by electromagnetic disturbances upstream and downstream of the shock, before reaching either one of the two boundaries. It is worth mentioning that, in all the several thousands trajectories that we have studied, we have never obtained a trajectory which is recorded at the upstream boundary without having crossed the shock front at least twice. This means that,
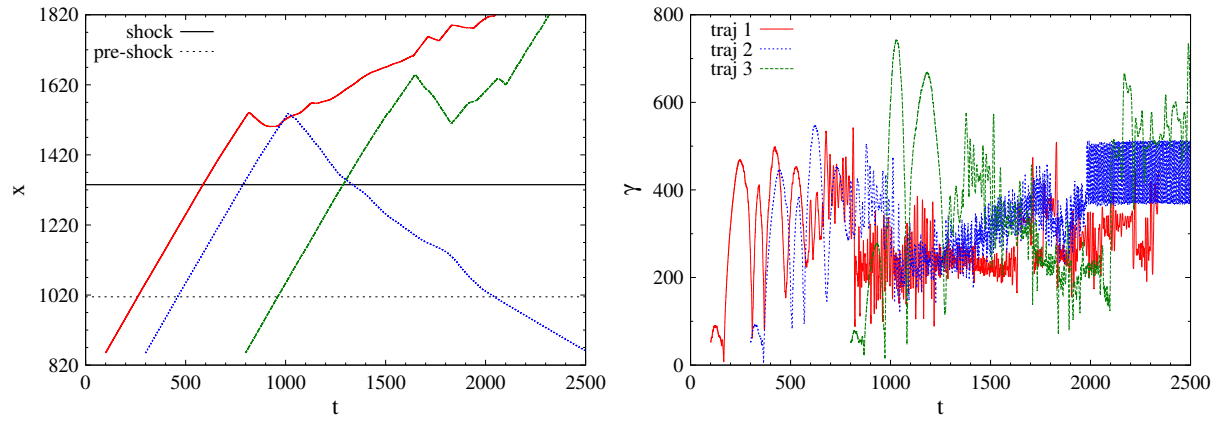
Figure 3.5: Time evolution of the trajectory (left panel) and respective Lorentz factor (right panel) for three particles in the background fields of RUN D1.2 in the region close to the leading edge of the precursor (dashed black line) and the shock front (solid black line).
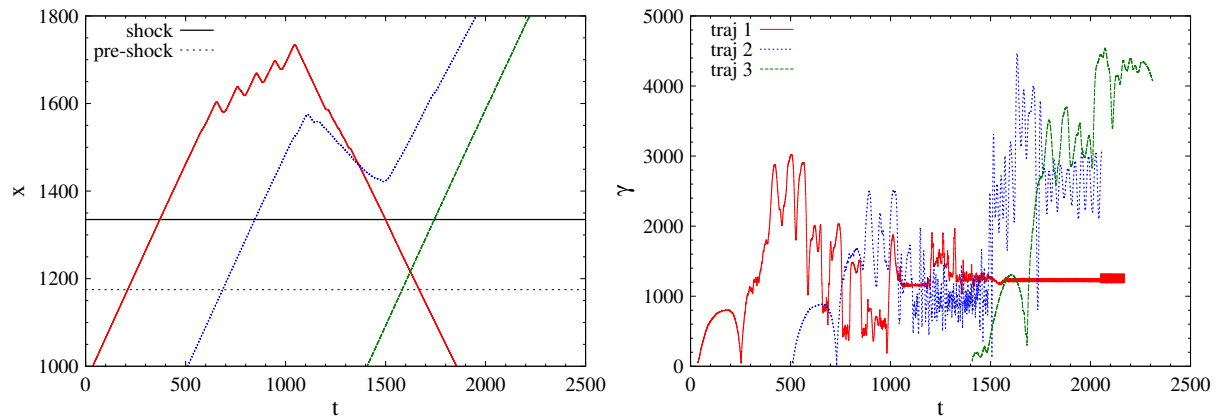
Figure 3.6: Time evolution of the trajectory (left panel) and respective Lorentz factor (right panel) for three particles in the background fields of RUN K1.2 in the region close to the leading edge of the precursor (dashed black line) and the shock front (solid black line).

despite the large degree of turbulence present in the precursor and the deflection taking place there, particles can only be reflected towards the upstream boundary by the residual turbulent fields surviving in the downstream. We also stress that, in the test particle approach, particles reflected towards the upstream boundary have negligible chances to be deflected once more in the opposite direction when they are upstream of the leading edge of the

pre-shock. This is due to the fact that superluminal waves are completely damped at some distance from the termination shock, as discussed in the previous chapter, so that the field configuration is completely ordered and has the magnetic shear wave form. In this idealised model, the field is not able to turn these trajectories around towards the downstream. This is visible for example for trajectory n. 2 in Fig. 3.5 and trajectory 1 in Fig. 3.6.

3.6   Injection probability

The electrons which are reflected back into the upstream at the shock form a population of particles which can undergo a full acceleration process, such as the Fermi mechanism which is normally invoked to explain the presence of very energetic particles in the proximity of shock fronts (e.g., [45, 79] for reviews). Thus, the region of turbulent fields generated in proximity of the shock, both upstream and downstream, by the propagation of superluminal waves can inject electrons in the subsequent acceleration mechanism. To investigate this mechanism, it is crucial to understand what is the fraction of trajectories which are reflected in the upstream at this electromagnetically modified relativistic, perpendicular shock, or in other words, what is the injection probability.

The physically relevant quantity called *injection probability* P_{inj} is the reflection probability for boundaries placed far from the shock. To estimate it from the simulation, we compute the ratio of the number of trajectories absorbed at the upstream absorbing boundary to the total number of trajectories as a function of the position of the boundaries. We then extrapolate the obtained behaviour as the boundaries are asymptotically far away from the shock. Hereafter, we will refer to the upstream boundary as UB, and to the downstream boundary as DB.

We start by placing both boundaries very close to the shock front and then we repeatedly move DB away from the shock by a fixed step $\xi = 50$. For each position of DB, we record how many trajectories are absorbed at both boundaries. Next, we move UB away from the shock by the same step ξ and we repeat the procedure. We do this for x_{UB} [835 : 1285] and x_{DB} [1485 : 1935] for RUN D1.2, and for x_{UB} [935 : 1285] and x_{DB} [1385 : 1885] for RUN K1.2, the shock being at $x_{sh} = 1335$ for both runs. The different choice for the ranges of UB and DB is justified by the different features of the precursors in RUN D1.2 and RUN K1.2.

With this technique, we are able to construct a grid of reflection probability values at different locations in the simulation box. This is showed in the top and bottom panels of Fig. 3.7 for RUN D1.2 and RUN K1.2, respectively. In these plots, the position of the boundaries recedes from the shock moving leftwards on the x-axis and upwards on the y-axis. We also stress that the normalisation of the colour scale is different in the two plots to better show the variation of P_{inj} in the bottom panel. We notice that when DB is close to the shock front $\Delta x \lesssim 150 - 200$, the reflection probability is almost negligible. This was already anticipated in Figs. 3.5 and 3.6, where we observed that in general electrons are not reflected immediately after crossing the shock. Thus, the close proximity of the absorbing boundary to the shock stops the trajectories before they have the chance to be scattered and reflected by the magnetic turbulence. When DB is further away from the termination shock, for a fixed location of UB, P_{inj} increases up to some level (different for RUN D1.2 and RUN K1.2) and then stabilises to an almost constant value. This is a consequence of the fact that far downstream the amplitude of the residual fields diminishes until they completely vanish, so that they are less efficient in deflecting the electron trajectories. At some point, the field fluctuations are so small that particles which are transmitted up to that point cannot come back to the shock. The situation is opposite for a particle travelling towards the upstream. In fact, instead of a region of electromagnetic fields with decreasing amplitude, it encounters a region of electromagnetic fields with increasing amplitude which is efficient in deflecting particles. Consequently, as UB recedes from the shock, the injection probability decreases
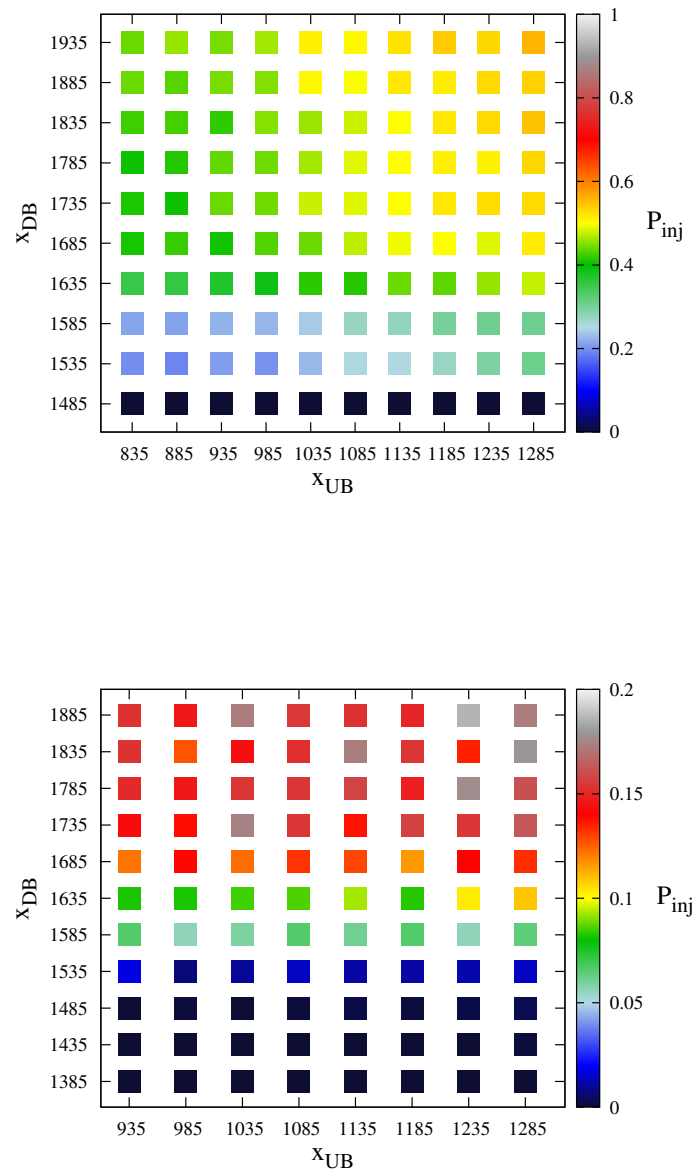
Figure 3.7: Injection/reflection probability map for RUN D1.2 (top panel) and RUN K1.2 (bottom panel). The shock position is $x_{\rm sh} = 1335$ for both runs. The absorbing boundaries recede from the shock front moving leftwards on the x-axis and upwards on the y-axis. Notice the different normalisation of the colour scale in the two panels.

for a fixed position of DB. For RUN D1.2 (top panel) the decrease of P_{inj} stops when UB moves from $x_{UB} = 1035$ to $x_{UB} = 985$, which coincides with the approximate location of the leading edge of the precursor (see left panel in Fig. 3.5). The asymptotic value of the injection/reflection probability is $P_{inj} \sim 0.40$. In the case of RUN K1.2 the situation is less clear since on average the injection probability is much smaller. However, one can see that for $x_{UB} = 1285$ and $x_{UB} = 1235$, $P_{inj} \sim 0.18 - 0.19$ (with some fluctuations), but when $x_{UB} \lesssim 1235$ the injection probability stabilises at $P_{inj} \sim 0.15$.

In principle, one could expect the injection probability for these two runs to be the same when UB is $\xi = 50$ away from the termination shock and DB is very far, given the fact that the fraction of dissipated Poynting flux is comparable for RUN D1.2 and RUN K1.2 at $x \sim 1500$ (see bottom panel in Figs. 2.11 and 2.14). Hence, the less extended precursor in RUN K1.2, where particles travelling towards the upstream have the chance to be deflected once more towards the downstream, would imply a larger asymptotic value of P_{inj} with respect to RUN D1.2. Nonetheless, this is not what we obtained since, as we have already noticed in Fig. 2.16, the residual fields in the region across the shock in RUN K1.2 are much less turbulent than those in RUN D1.2 and the more ordered the field, the less efficient the particle scattering and deflection.

Normally, the issue concerning the injection mechanism into an acceleration process is overlooked, as well as the location of the injection (e.g., [112, 46]). In this work we try to answer these questions. The values that we obtain for the injection probability at the termination shock for the two cases must be compared with $P_{inj} \approx 0.12$ found by [2] for ultra-relativistic ($\Gamma = 100 - 1000$), oblique shocks. These authors considered the following source of scattering: magnetic waves (Alfvén's waves) in the downstream and a combination of waves supported by a uniform magnetic field upstream (this approach has been introduced in [140] and will be treated in more detail in the next chapter). We infer that, at least in the situations that we investigate, the turbulence generated by the propagation of the superluminal wave are more efficient in deflecting particles than Alfvén's waves. This is true for both RUN D1.2 and RUN K1.2.

The value $P_{inj} \sim 0.40$ obtained for RUN D1.2 might be too large for the test particle limit to be valid. In fact, the current of energetic particles streaming from downstream to upstream would probably severely affect the shock structure like in a cosmic-ray modified shock [47]. On the other hand, we believe that $P_{inj} \sim 0.15$ that we obtain for RUN K1.2 is more consistent with the test particle approach, since in this case the energy density flux streaming upstream is much lower. However, it is difficult in both situations to estimate what is the combined effect of electromagnetic waves and energetic particles on the stability of the shock and its precursor and a dedicated and self-consistent study (such as Particle-In-Cell simulation) is probably needed to address this issue.

3.7 Energy spectrum and angular flux

We now compute the spectrum and angular flux of transmitted and reflected particles at the location of UB and DB where the injection probability reaches the asymptotic value, both for RUN D1.2 and RUN K1.2. This means $x_{UB} = 935$ and $x_{DB} = 1935$ for RUN D1.2 and $x_{UB} = 985$ and $x_{DB} = 1885$ for RUN K1.2. In Fig. 3.8 we plot the energy spectrum of transmitted (blue points) and reflected (red points) particles for RUN D1.2 (left panel) and for RUN K1.2 (right panel) for the benchmark configuration of our simulation. The spectrum is plotted in the downstream fluid frame for transmitted particles and in the upstream fluid frame for reflected particles. The vertical solid black lines represent the energy values $\Gamma_{0,i}(\sigma_{0,i} + 1)$ and $\Gamma_{0,i}^2(\sigma_{0,i} + 1)$, where $i = D, K$ and the extra Lorentz factor in the latter expression comes from the transformation in the upstream rest frame. The dotted lines
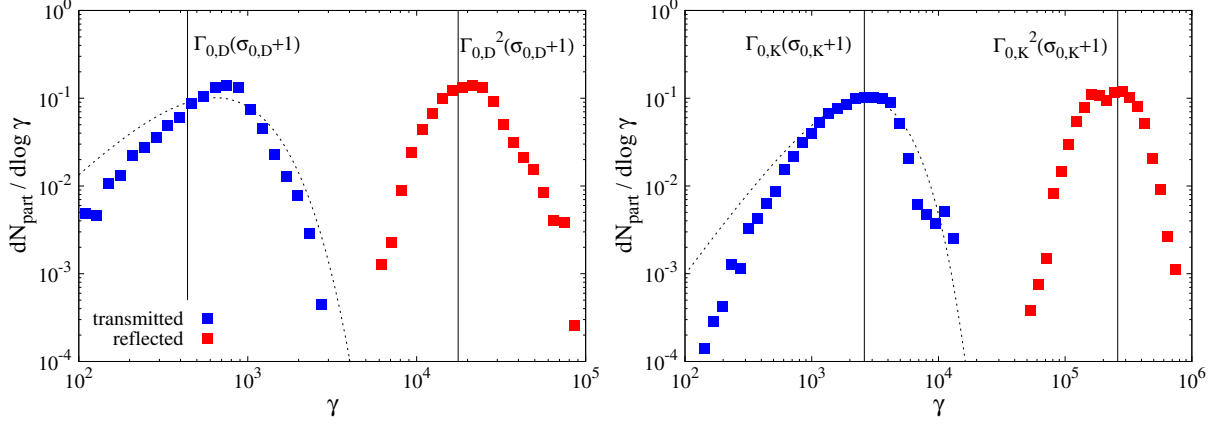
Figure 3.8: Energy spectrum of transmitted and reflected particles for RUN D1.2 (left panel) and RUN K1.2 (right panel). The vertical solid black lines represent the energy values $\Gamma_{0,i}(\sigma_{0,i} + 1)$ and $\Gamma_{0,i}^2(\sigma_{0,i} + 1)$, where $i = D, K$. The dotted lines in both panels represent a relativistic Maxwellian distribution peaked at $\Gamma_{0,i}(\sigma_{0,i} + 1)$.

in both panels represent two relativistic Maxwellian distributions [124]

$$f(\gamma) \propto \gamma \sqrt{\gamma^2 - 1} \, e^{-\gamma/\Delta\gamma} \tag{3.10}$$

whose average energy is $\langle\gamma\rangle = \Gamma_{0,i}(\sigma_{0,i} + 1)$ and $\Delta\gamma \sim 300$ for RUN D1.2 and $\Delta\gamma \sim 1300$ for RUN K1.2 (we stress that the dotted lines do not represent a fit to the data points). Our results are similar for the two runs. The spectra of transmitted electrons peak at $\approx \sigma_{0,i}\Gamma_{0,i}$ and those of reflected electrons peak at $\approx \sigma_{0,i}\Gamma_{0,i}^2$, meaning that test particles interacting with the electromagnetic turbulence in the proximity of the termination shock basically gain the energy which is dissipated by the incoming pulsar wind. As far as reflected particles are concerned, the fact that during the first shock encounter the energy gain is $\propto \Gamma_0^2$ is a classic result (e.g., [137, 2]). However, here we show that the electromagnetically modified shock is able to convey an extra σ_0 factor due to the dissipation of the striped wind.

Hence, we find that not only the precursor ahead of the shock and the turbulent region downstream of it are able to generate a population of particles travelling towards the upstream, but they can also energise this population. This constitutes the seed for the subsequent full acceleration process.

Acceleration of particles in superluminal electromagnetic waves has already been studied in the context of pulsar winds by [134] using a test particle approach. The authors assume that in the proximity of the termination shock, the turbulent electromagnetic fields can be described by a superposition of electromagnetic waves: a primary wave generated by the striped wind (entropy mode) moving in the same radial direction and isotropically distributed secondary waves. They also find that test particles are pre-accelerated in this environment via the interaction with the superluminal waves. Remarkably, our spectra for transmitted electrons are in good agreement with the results of [134] for a situation in which the amplitude of the secondary waves is about the same of the primary wave. In our 1-dimensional simulation, of course, the secondary waves are not isotropically distributed, but their amplitude
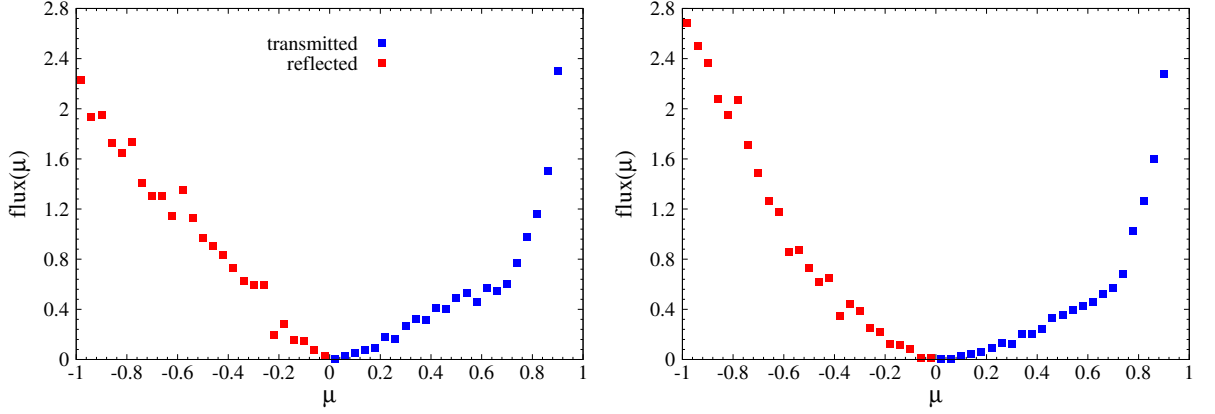
Figure 3.9: Angular flux of the particles transmitted across the shock (blue points) and injected in the acceleration process (red points) are shown in Fig. 3.9 for RUN D1.2 (left panel) and RUN K1.2 (right panel) expressed in the shock frame.

is comparable with that of the primary wave (see the wave spectral analysis published in [6]).

Interestingly, 1-dimensional [114] and 2-dimensional [125] Particle-In-Cell simulations show that electrons accelerated during driven magnetic reconnection at the TS of a pulsar striped-wind are also distributed in a Maxwell-like distribution peaked at $\approx \sigma_0 \Gamma_0$. This strengthens the argument that the magnetic reconnection and the dissipation of the magnetic field driven by the propagation of superluminal waves are two aspects of the same phenomenon, taking place at relatively large plasma density (the former) and low plasma density (the latter). Furthermore, none of these two processes is able to produce the power-law spectrum of particles necessary to explain the Synchrotron radiation observed for example from the Crab nebula.

The angular flux of the particles transmitted across the shock (blue points) and injected in the acceleration process (red points) are shown in Fig. 3.9 for RUN D1.2 (left panel) and RUN K1.2 (right panel). Quantities are expressed in the shock frame, for direct comparison of the two components. We see that, in this frame, the angular distribution is far from being isotropic. On the contrary, the distribution of transmitted particles is strongly peaked in the forwards direction $\mu = 1$, while the distribution of reflected particles is broader, but strongly directed anti-parallel with respect to the shock normal. Specifically, if we look at the flux of reflected particles in the upstream fluid frame, we obtain a very peaked and narrow distribution in the direction $\overline{\mu} = -1$, with a half width at half maximum of $\sim 5 \cdot 10^{-4}$.

The test particle approach used in this chapter allows us to study the mechanism of pre-acceleration of a population of particles at the TS in PWNe. The pre-acceleration process consists of two phases. Firstly, particles gain energy in the turbulent region formed ahead of the shock by the interaction between superluminal waves and the striped pulsar wind, where non-vanishing electric fields can accelerate particles in the direction perpendicular to the propagation of the flow. Secondly, these particles scatter off electromagnetic turbulence surviving downstream

of the termination shock and a fraction of them is reflected upstream. The energy distribution, expressed in the upstream rest frame, of particles reflected in the upstream at the first shock encounter peaks at $\overline{\gamma} \approx \sigma_0 \Gamma_0^2$. Their angular flux, also expressed in the upstream frame, is directed in a very narrow cone about the direction anti-parallel to the normal to the shock front $\overline{\mu} = -1$. Reflected particles are then injected in a full Fermi-like acceleration process.

Chapter 4

Particle acceleration: Monte Carlo approach

In Chapt. 3 we have shown that the electromagnetic turbulence generated by the interaction between the striped pulsar wind and its termination shock produce a population of non-thermal (pre-accelerated) particles travelling against the wind in the direction of the upstream. In the idealised model studied there, no further acceleration of these particles is possible when they leave the shock precursor since they travel in the unperturbed magnetic shear wave. However, if the incoming striped-wind contains magnetic irregularities capable of acting as elastic scattering centres (such as Alfvén's waves or turbulence generated by energetic particles streaming upstream of the shock), escaping particles have the possibility of returning to the shock, *i.e.*, of undergoing additional acceleration in the same way as in the conventional picture of Diffusive Shock Acceleration (e.g., [12, 18, 22]) or Fermi-like acceleration (e.g., [79]). The present chapter is devoted to the study of this acceleration process, in particular in the environment of a pulsar wind, with numerical methods.

In Sect. 4.1 we revise the theory of first and second order Fermi acceleration and in Sect. 4.2 we briefly introduce the main techniques used to simulate first-order Fermi acceleration at relativistic shocks. In this work, the presence of magnetic turbulence on both sides of the shock is simulated with the standard technique of *pitch-angle* scattering (e.g., [53, 2, 128]). This routine is implemented in a Monte Carlo code which integrates particle trajectories and simulates the Fermi acceleration process in different situations. We present the details of the Monte Carlo code in Sect. 4.3. The features of the population of accelerated particles are expressed in terms of the energy spectrum and angular distribution, which determine the phase-space distribution function as explained in Sect. 4.4. In Sect. 4.5 we present the results of our simulations in different situations. In Sects. 4.5.1 and 4.5.2 we test our code in two cases for which an analytical or numerical solution already existed: (1) the only source of particle deflection both upstream and downstream is pure scattering off magnetic inhomogeneities [81]; (2) the source of particle deflection upstream is a static and uniform magnetic field whose direction is perpendicular to the shock normal [2]. For both cases, we obtain an excellent agreement with the results published in the literature for different speeds of the shock front. In Sect. 4.5.3 we introduce the set-up used to simulate the pulsar striped-wind in the upstream of the shock and the magnetic fluctuations which are not resolved in the two-fluid simulations presented in Chapt. 2. Downstream of the shock only turbulence is present since the average magnetic field vanishes. We show that in this environment the acceleration proceeds in two regimes, according to the relative magnitude of the particle

gyro-radius and of the wavelength of the stripes. Finally, in Sect. 4.6 we study the effects of a limited acceleration region on the spectrum and angular distribution.

4.1 Fermi acceleration

The mechanism which is usually held responsible for particle acceleration at relativistic shocks is Fermi-like acceleration (e.g., [112, 14, 83]). The basic idea dates back to Enrico Fermi [54], who suggested in 1949 that charged cosmic rays gain energy when they are scattered during the encounter with a galactic cloud. The picture is the following. A charged particle of energy γ (and speed β) and momentum $\mathbf{p}$ in the lab. frame enters a cloud moving in the negative x- direction with speed β_c (Γ_c is the respective Lorentz factor). The Lorentz factor of the particle is supposed to be large compared with the thermal energy of the background plasma. In the reference frame of the cloud (primed quantities are expressed in this frame, K') the electric field vanishes. We assume that the magnetic field is strong enough to reflect the particle. In K', the energy of the particle before being reflected is

$$\gamma'_{\text{before}} = \Gamma_c(\gamma + \beta_c p_x) = \Gamma_c(\gamma + \beta_c p \mu) \tag{4.1}$$

where μ is the cosine of the angle between $\mathbf{p}$ and the x-axis Accordingly, the momentum in the frame of the cloud is given by

$$p'_{x,\text{before}} = \Gamma_c(p_x + \beta_c \gamma). \tag{4.2}$$

Given that the deflection is elastic in K', the energy is unchanged when the particle leaves the cloud, $\gamma'_{\text{before}} = \gamma'_{\text{after}}$, whereas the momentum is in the opposite direction $p'_{x,\text{after}} = -p'_{x,\text{before}}$. Now, transforming back to the laboratory frame, we have that the energy after the reflection is

$$\gamma_{\text{after}} = \Gamma_c(\gamma'_{\text{after}} - \beta_c p'_{x,\text{after}}) = \Gamma_c(\gamma'_{\text{before}} + \beta_c p'_{x,\text{before}}) \tag{4.3}$$

and the substitution of Eqs. 4.1 and 4.2 in the last expression yields

$$\gamma_{\text{after}} = \Gamma_c^2 \gamma(1 + 2\beta_c \beta \mu + \beta_c^2). \tag{4.4}$$

The speed of these clouds is always much smaller than the speed of light $\beta_c \ll 1$, so we expand Eq. 4.4 in the small parameter β_c and we only retain terms up to second order. Thus, using $\Gamma_c^2 \sim 1 + \beta_c^2$, we obtain

$$\frac{\Delta\gamma}{\gamma} \approx 2\beta_c \beta \mu + 2\beta_c^2 \tag{4.5}$$

where we see that the energy gain contains a term which depends on the first power of the speed of the scattering agent (the magnetic field of the cloud) β_c and one term which depends on the second power of this small quantity. We also realise that, because of the presence of μ, a head-on collision leads to a positive contribution to the energy gain by the first-order term, while a tail-on collision leads to a negative contribution. The number of collision events per unit time is proportional to the relative speed between the particle and the cloud in the direction of $\mathbf{p}$

$$\beta_{\text{rel}} = \frac{\beta + \beta_c \mu}{1 + \beta_c \beta \mu} \tag{4.6}$$

and to the element of solid angle $d\Omega/4\pi = d\mu/2$. We can expand the expression for β_{rel} in terms of β_c and keep only the leading terms as we did above

$$N_{\text{coll}} \propto \beta_{\text{rel}} \frac{d\mu}{2} \approx \frac{1}{2}(\beta + \beta_c \mu)(1 - \beta_c \beta \mu)d\mu \approx \frac{1}{2}(1 + \beta_c \mu)d\mu = P(\mu)d\mu \tag{4.7}$$

where we exploit the fact that the speed of energetic particles is $\beta \sim 1$ and explicitly write the value of the collision probability as a function of μ. Now, assuming that the velocities of clouds are isotropically distributed, if we average the energy gain (Eq. 4.5) over the collision probability over all possible angles, we obtain two second order contributions summing up to give

$$\langle \frac{\Delta\gamma}{\gamma} \rangle = \frac{8}{3}\beta_c^2 \tag{4.8}$$

from which the process is called second-order Fermi acceleration, since the average energy gain is proportional to the second power of the small quantity β_c.

The situation is different if, instead of clouds reflecting energetic particles, we consider the situation at a non-relativistic shock front (e.g., [18, 45] for reviews). Let us consider the case depicted in Fig. A.1, where a planar, infinite shock front divides the upstream and downstream fluids which move along the x-axis in the positive direction with speeds $\overline{\beta}_s$ and $\widetilde{\beta}_s$, respectively, as seen in the Shock Rest Frame (SRF). In the following of this work, k is a quantity expressed in the SRF, $\overline{k}$ is a quantity expressed in the Upstream Rest Frame (URF) and $\widetilde{k}$ is a quantity expressed in the Downstream Rest Frame (DRF) (see Appen. A for a sketch of the shock geometry and for the full set of Lorentz transformations between these three reference frames). The speeds $-\overline{\beta}_s$ and $-\widetilde{\beta}_s$ are the speeds of the shock front in the URF and DRF, respectively. An energetic particle crossing the shock from upstream to downstream (from left to right in our picture) sees the downstream fluid approaching at a speed β_{rel} given by Eq. A.17, which in the non-relativistic limit tends to $\beta_{rel} = \overline{\beta}_s - \widetilde{\beta}_s$. For this crossing to take place, the projection of the particle velocity, whose magnitude is $\overline{\beta} \sim 1$, onto the x-axis must be larger than the shock speed $\overline{\beta}\,\overline{\mu} > -\overline{\beta}_s$. In the non-relativistic situation under consideration, this condition can be written as $\overline{\mu} \gtrsim 0$. Analogously, for a particle to cross the shock from downstream to upstream, the condition $\widetilde{\mu} \lesssim 0$ must be fulfilled. In DRF, the energy of the particle is $\widetilde{\gamma}$, which does not change in case the downstream magnetic field is able to deflect the particle once more into the upstream. The energy after one cycle upstream $\rightarrow$ downstream $\rightarrow$ upstream is given by

$$\overline{\gamma}_{after} = \Gamma_{rel}^2 \overline{\gamma}(1 + 2\beta_{rel}\overline{\beta}\overline{\mu} + \beta_{rel}^2). \tag{4.9}$$

The flux of particle crossing the shock from upstream to downstream with $\overline{\mu}$ is $\overline{J}(\overline{\mu}) = \overline{n}c\overline{\mu}$, where $\overline{n}$ is the spatial density of energetic particles expressed in URF, and the total flux is

$$\overline{J}_{tot} = \int_0^1 \frac{d\overline{\Omega}}{4\pi} \overline{n}c\overline{\mu} = \frac{\overline{n}c}{4}. \tag{4.10}$$

where we take into account the constraint on $\overline{\mu}$ discussed above. The probability of a particle crossing the shock from left to right with specific $\overline{\mu}$ is given by the ratio $\overline{J}(\overline{\mu})/\overline{J}_{tot} = 4\overline{\mu}$, multiplied by the element of solid angle. If we assume gyrotropy, this leads to $P(\overline{\mu})d\overline{\mu} = 2\overline{\mu}d\overline{\mu}$. Averaging Eq. 4.9 on this probability distribution yields

$$\langle \frac{\Delta\overline{\gamma}}{\gamma} \rangle = \frac{4}{3}\beta_{rel} + 2\beta_{rel}^2 \tag{4.11}$$

from which the mechanism is called first-order Fermi acceleration, since the leading term is of first order in the small quantity β_{rel} ($\Gamma_{rel} \sim 1$). The efficiency of this acceleration process is determined by the balance between the energy gain at each cycle about the shock and the probability that a particle in the downstream escapes from the vicinity of the shock. As a consequence, the time-independent phase-space density $f(\mathbf{x}, \mathbf{p})$ has a power-law spectrum $\propto p^{-s}$, whose spectral index $s = 3r/(r-1)$ only depends on the shock compression ratio $r = \overline{\beta}_s/\widetilde{\beta}_s$ [79]. This derivation is based on the assumption that particles on both sides of the shock are elastically scattered by

magnetic turbulence embedded in the fluid, normally produced by Alfvén's waves [18, 22]. This causes the distribution function to be almost isotropic in the fluid frame, situation that is described by the spatial diffusion equation [12, 22, 45]

$$\frac{\partial f}{\partial t} + u_{\mathrm{x}} \frac{\partial f}{\partial x} = \frac{\partial}{\partial x} D_{\mathrm{xx}} \frac{\partial f}{\partial x} + \frac{1}{3} \frac{\partial u}{\partial x} p \frac{\partial f}{\partial p} \tag{4.12}$$

where u_{x} is the speed of the fluid, D_{xx} is the spatial diffusion coefficient and f is the proper frame phase-space density. The first-order Fermi acceleration process in the non-relativistic, diffusive regime is called Diffusive Shock Acceleration (DSA). However, in this work we are interested in the relativistic counterpart of this mechanism.

4.2 First-order Fermi acceleration at relativistic shocks

When the flow speed is relativistic, the picture changes substantially from the non-relativistic case. The relative speed β_{rel} between the upstream and downstream sides of the shock is of the order of the speed of light and of the speed of energetic particles. The Lorentz boost linking the URF and DRF introduces strong anisotropies in the angular distribution, as we shall see in the following.

For the particular case of relativistic and perpendicular[1] shocks, like the termination shock of pulsar winds (at the TS the magnetic field is predominantly toroidal), the Fermi acceleration process is supposed to be inefficient (e.g., [17, 124]). In fact, the guiding centres of particle trajectories are connected to the magnetic field lines which are parallel to the shock front and are advected far downstream, increasing the escape probability. Strong cross-field diffusion is required to compensate the effective advection experienced by particles in the downstream of the shock, where the flow speed is a sizeable fraction of the speed of light. However, the speed of the downstream fluid does not increase indefinitely as the Lorentz factor of the shock increases. For strong shocks, it reaches a maximum value $\widetilde{\beta}_{\mathrm{s}} \sim 1/3$ for $\overline{\Gamma} \gg 1$, given by the jump conditions for a strong shock with the Jüttner/Synge equation of state [81]. This sets a limit on the increase of the downstream escape probability as the shock becomes faster. In addition, the decrease of the acceleration efficiency in the relativistic regime is also partly compensated by the energy gain per cycle, which is enhanced as the shock becomes faster.

A thorough study of the angular distribution and energy spectrum of particle accelerated by the first-order Fermi process at a relativistic shock can be conducted in two different approaches.

The first approach consists in the solution of the relativistic transport equation in the upstream and downstream media separately. The two solutions must then be matched at the shock front. The time-dependent, fully relativistic transport equation is a Fokker-Planck type equation and reads as follows

$$\Gamma_{\mathrm{f}}(1 + \beta_{\mathrm{f}}\mu) \frac{\partial f}{\partial t} + \Gamma_{\mathrm{f}}(\beta_{\mathrm{f}} + \mu) \frac{\partial f}{\partial x} = \frac{\partial}{\partial \mu} D_{\mu\mu} \frac{\partial f}{\partial \mu} \tag{4.13}$$

where β_{f} and Γ_{f} are the fluid speed and Lorentz factor, respectively, and $D_{\mu\mu}$ is the *pitch-angle* diffusion coefficient[2]. Here, the Lorentz factor of the particles is assumed to be much larger than that of the fluid and consequently their speed have been replaced with the speed of light $c = 1$. The relation is expressed in the mixed coordinate

---

[1]A shock is defined to be perpendicular when the magnetic field is perpendicular to the shock normal (*i.e.*, the magnetic field lies in the plane of the shock.)

[2]In this specific example the magnetic field is directed along the x-axis, so that $\mu = \cos\theta$, where θ is the angle between the particle momentum and the x-axis.

system and μ is alternately expressed in URF and DRF[3]. Equation 4.13 is solved using an eigenfunction method [85, 81], which expands the solution in spherical harmonics and allows to compute the power-law spectral index of accelerated particles.

The second approach consists in the numerical integration of particle trajectories. This can be done by specifying the electromagnetic fields in the relevant spatial region (e.g., [15, 111]), where all kinds of waves and power-spectra can be prescribed and trajectories are integrated directly. A complementary technique, which is also used in this work, consists in the simulation of the transport properties of the fields themselves. This is realised with a Monte Carlo method which builds a stochastic trajectory whose distribution obeys the desired transport equation. Repeating the procedure for a large number of trajectories allows to approximately build the energy spectrum and the angular distribution. This approach has been extensively used to investigate particle acceleration at relativistic, hydrodynamic and magnetohydrodynamic shocks (e.g., [53, 52, 128]). This is done here by following the Ito prescription presented in [3], namely exploiting the correspondence between the Fokker-Planck type equation (Eq. 4.13) and a set of stochastic differential equations (SDEs) [56].

4.3 Details of Monte Carlo simulation

We develop a Monte Carlo code to simulate electron (and positron) acceleration at relativistic shocks. The set-up is the following. The shock front is a 2-dimensional infinite interface in the yz-plane, whose normal is parallel to the x-axis. The speed of the upstream and downstream, as measured in the shock frame, are $\overline{\beta}_s$ and $\widetilde{\beta}_s$, respectively, and are directed along the x-axis in the positive direction. The associated Lorentz factors are $\overline{\Gamma}_s = (1 - \overline{\beta}_s^2)^{-1/2}$ and $\widetilde{\Gamma}_s = (1 - \widetilde{\beta}_s^2)^{-1/2}$. The polar angle θ and azimuthal angle ϕ are measured from the x-axis and $\mu = \cos\theta$. The particle trajectories are described as in Chapt. 3 by the set of equations Eqs. 3.2-3.7, where some of them are supplemented by a stochastic term. The resulting SDEs are of the kind

$$h_{i+1} = h_i + f_i \Delta t + b_i (W_{i+1} - W_i) \tag{4.14}$$

where the solution for the dependent variable h is advanced from the step i to the step i+1 by summing a deterministic contribution f_i, as in Eq. 3.9, and a stochastic contribution $\Delta W = W_{i+1} - W_i$. This comes from the difference between two steps in a Wiener process multiplied by a coefficient b_i. In the specific problem treated here, the Wiener process corresponds to *pitch-angle* scattering off magnetic turbulence embedded in the background plasma, during which the direction of the momentum vector changes, while its magnitude does not. Here we use the term *pitch-angle* rather loosely to define the angle between the particle momentum and the x-axis, which is the symmetry axis in our scheme (see Fig. A.1 in Appen. A).

Operatively, the only equations in our set to be modified are Eqs. 3.6 and 3.7, which compute the polar angle θ and the azimuthal angle ϕ, respectively. This is done under the assumption that the scattering is elastic in the plasma rest frame. For these two relations, the deterministic part of the increment is always due to the Lorentz force and computed as before, where the average values of the electric and magnetic fields are defined according to the physical environment to simulate. On the other hand, the stochastic contribution is computed allowing the momentum vector to be isotropically deflected within a small cone of aperture

$$\delta\theta_{\max} = \alpha \sqrt{\Delta t} \tag{4.15}$$

---

[3]In the mixed coordinate system of phase-space coordinates momentum-space variables **p** are expressed in the local fluid frame and position-space variables **x** are expressed in the lab. frame

about its *deterministic* direction at each time step during the integration of the trajectory. In this expression, Δt is the time step of the integration and α is a proportionality constant. The sum of several of these steps corresponds to a random motion of the tip of the momentum vector on the surface of a sphere. This approach simulates the properties of the scattering operator [129]

$$\frac{\partial}{\partial \mu} D_{\mu\mu} \frac{\partial f}{\partial \mu} + \frac{1}{1 - \mu^2} \frac{\partial^2 f}{\partial \phi^2} \tag{4.16}$$

describing the continuous deflection undergone by a charged particle immersed in electromagnetic fields. In our treatment, the stochastic increment ΔW for θ and ϕ corresponds to the difference between the *stochastic* and *deterministic* values of the angle, where $b_i = 1$ (the details of the method to obtain the stochastic increment for the angles θ and ϕ can be found in Appen. B).

The value of the aperture angle of the scattering cone $\delta\theta_{max}$ determines the resolution that our numerical method can attain when we reconstruct the angular and spectral distributions of accelerated electrons. At a relativistic shock, the angular distribution is expected to present structures on the scale of the loss-cone. The definition of loss-cone in the URF stems from the condition $\overline{\mu} < -\overline{\beta}_s$ which confines a particle upstream of the shock. As a consequence, the aperture angle of the upstream loss-cone is

$$\overline{\theta}_c \sim \sin \overline{\theta}_c = \sqrt{1 - \overline{\beta}_s^2} = \frac{1}{\overline{\Gamma}_s} \tag{4.17}$$

since the shock is relativistic. If the simulation is performed in the large-angle scattering regime $\delta\theta_{max} \gtrsim \overline{\theta}_c$, a particle can cross the shock into the downstream only few steps upon entering the upstream. This results in a poor approximation of the continuous deflection process and possibly in unrealistically large deflection angles, and consequently energy gain, in one single Fermi cycle [53]. Thus, to correctly resolve structures on the scale of $\overline{\theta}_c$, we select $\delta\theta_{max} \ll 1/\overline{\Gamma}_s$ for our entire set of Monte Carlo runs. The value of the maximum aperture of the scattering cone determines the diffusion properties through the diffusion coefficient [140]

$$D_\theta = \frac{1}{2} \frac{\langle \delta\theta_{max}^2 \rangle}{\Delta t} \tag{4.18}$$

which is constant with energy in our prescription. The integration time step, and consequently the maximum scattering angle and the diffusion coefficient, have different definitions in URF and DRF, to combine the fulfillment of the precision criterion expressed above with the rapidity of the numerical integration.

The set of equations resulting from the implementation of the stochastic increment is integrated with an explicit first-order Euler's scheme as in [3], which is very fast, even though the discretisation error is only of the second order in Δt. However, the intrinsic stochastic nature of the error and the choice of a small integration time step help keeping this error under control (see Sect. 3.2).

The Monte Carlo simulation is performed as follows. A large number of trajectories are started at the shock front with the angular distribution and initial energy obtained with the test particle approach, namely $\overline{\mu}_{inj} = -1$ and $\overline{\gamma}_{inj} = \sigma \overline{\Gamma}_s^2$. The particle integration is carried out in URF until the particle is overtaken by the shock front. As already said, this can happen only if $\overline{\mu} > -\overline{\beta}_s$. Upon shock crossing, magnitude and direction of the momentum of the electron are stored and then Lorentz boosted to DRF, where the trajectory is integrated until it either crosses back into the upstream, or until it reaches the location of an absorbing boundary placed far away from the shock front, where the return probability is negligible. The former occurrence, similarly to the upstream → downstream

transition, can only occur if $\widetilde{\mu} < -\widetilde{\beta}_s$, in which case the energy and direction are again saved and then transformed in URF, where the integration is carried on. In the latter case, particles are removed from the simulation. The distance of the absorbing boundary d_{abs} from the shock is defined to be 500 times the downstream scattering length $\widetilde{L}_{scat} = c\widetilde{t}_{scat} = 1/2\widetilde{D}_\theta$ ($c = 1$), which is the average distance over which a particle is deflected by an angle $\widetilde{\theta}_c \sim 1/\widetilde{\Gamma}_s$ [140]. This ensures that the presence of the boundary affects neither the energy spectrum nor the angular distribution at the shock front.

Because of the loss of particles at the absorbing boundary, the number of particles returning into the upstream diminishes when the number of complete cycles upstream → downstream → upstream becomes large. To cope with the loss of statistics and increasing Poisson's noise at high energy stemming from this, we implement a particle splitting routine which activates when a given particle performs C complete cycles (usually $C = 4 - 5$). When this happens, the values of $\widetilde{\gamma}$ and $\widetilde{\mu}$ at the shock front upon entering the downstream are stored as initial conditions for N copy particles, each one having statistical weight $w_{stat} = 1/N$. All copy particles are evolved independently, starting with these initial conditions, using the procedure outlined above. The number of copy particles we use in this work is $N = 10 - 50$.

We run several, statistically independent realisations of this prescription and we record energy and direction of particles upon shock crossing. This procedure allows us to simulate a steady state situation and to construct the time independent phase-space distribution function $f(\mathbf{x}, p, \mu)$ at the location x_{sh} of the shock front, which we call $f(p, \mu)$, in all relevant frames of reference.

4.4 Phase-space distribution function

All the features of the population of accelerated electrons are collected in the Lorentz invariant phase-space distribution function $f(p, \mu)$ [121]. The dependence of the phase-space density on the azimuthal angle ϕ will be studied only for few cases (see Sects. 4.5.2 and 4.5.3), whereas in general we will focus on the behaviour of f with respect to the momentum p and direction $\mu = \cos\theta$. We can separate the energy and angular dependencies of $f(p, \mu)$ as explained below.

4.4.1 Energy spectrum

The electrons (and positron) energy spectrum is obtained integrating the time independent phase-space distribution function $f(p, \mu)$ over angles. In the first-order Fermi acceleration process, the spectrum is generated by a competition between the escape rate of particles from the proximity of the shock and the amount of energy gained at every cycle across the shock. This acceleration mechanism has long been known to produce a power-law distribution $f(p, \mu) = p^{-s}g(\mu)$, where s is the spectral index and $g(\mu)$ carries the angular dependence. Given that $p = mc\beta\gamma$ ($m = 1$ in this work), we use the following notation $f(\gamma, \mu) = \gamma^{-s}g(\mu)$. The energy dependent spatial density of particles is $n(\gamma) = 4\pi\gamma^2 f(\gamma) \propto \gamma^{2-s}$, computed expressing the phase-space volume element as $d\mathcal{V} = d^3 p d\mu d\phi \propto \gamma^2 d\gamma d\mu d\phi$ and integrating over angles. Now, the number of particles with energy in the range $[\gamma : \gamma + d\gamma]$ is

$$N_{part} \propto \int_\gamma^{\gamma+d\gamma} n(\gamma)d\gamma \propto \int_\gamma^{\gamma+d\gamma} \gamma^{2-s}d\gamma \,. \tag{4.19}$$

If we multiply and divide the integrand by γ, we recognise $d \log \gamma = d\gamma/\gamma$, which yields the differential spectrum

$$\frac{dN_{part}}{d \log \gamma} \propto \gamma^{3-s} = \gamma^{-s'} \tag{4.20}$$

meaning that s' is the slope of the spectrum when the energy of each particle is binned in equally spaced logarithmic bins. This is the quantity that we plot in Figs. 3.3 and 3.8. The spectral slope is obtained by fitting the energy spectrum with a non-linear least-squares Marquardt-Levenberg algorithm [92, 98].

The energy range over which we perform the fit is selected according to two criteria: (1) avoidance of the influence of the initial conditions; (2) rapid and robust determination of the spectral index. Criterion (1) is met by considering the contribution of electrons which have performed least 5 complete cycles about the shock front. In most of the cases studied in this work, this corresponds to setting the minimum energy for the fit to $\overline{\gamma}_{\min} \gtrsim 30 \, \overline{\gamma}_{\mathrm{inj}}$. This ensures that there is no memory of the conditions at injection (the same criterion is used by [2]). As for criterion (2), the robust determination of the value of s would require high statistics over the widest possible energy range. However, in the Monte Carlo simulation the energy of one particle undergoing Fermi acceleration can become arbitrarily large, if energy losses are neglected and if the size of the acceleration region is much larger than the scattering length, as in this case. On average, the number of steps forming an excursion upstream is large when the electron Lorentz factor is large, so that the numerical integration of the trajectories of very energetic particles becomes computationally expensive. In this work, to constrain the spectrum over many orders of magnitude in energy without increasing unreasonably the computational time, we remove from the simulation electrons which have performed 25 complete cycles about the shock front. The maximum energy is usually $\overline{\gamma}_{\max} \sim 10^6 \, \overline{\gamma}_{\mathrm{inj}}$

Although a fit of the differential spectrum directly measures the spectral index s', in the following we will always provide our results in terms of $s = s' + 3$, spectral index of the energy dependence of the phase-space density. In addition, the spectrum is always normalised to the total number of electrons recorded at the shock and expressed in URF, for direct comparison with published results, e.g., [2]. To do so, a simple Lorentz boost to URF of the energy of particles crossing the shock from downstream to upstream is required.

4.4.2   Angular distribution

The construction of the angular distribution $g(\mu)$ is slightly more complicated and one needs to consider some subtle points. In fact, dimensionally, $g(\mu)$ is the density of particles in the range $[\mu : \mu + d\mu]$, but in the simulation we measure a number of events, rather than a density. Specifically, in URF the total number of recorded events in a steady state is

$$\overline{N}_{ev} = \int d^3 \overline{p} \, \overline{f}(\overline{x}, \overline{p}, \overline{\mu})(\overline{\mu} + \overline{\beta}_{\mathrm{s}}) \overline{\Delta t} \, dA \tag{4.21}$$

where $(\overline{\mu} + \overline{\beta}_{\mathrm{s}}) \overline{\Delta t}$ is the column of particles which is able to cross the shock front in a time interval $\overline{\Delta t}$ as it moves with speed $-\overline{\beta}_{\mathrm{s}}$ and dA is the shock surface element. Events are collected over the entire surface of the shock and during the total simulation time. The integration over these two quantities provides a normalisation factor which is unimportant for extracting the angular distribution and is consequently dropped in the following as we are interested in the functional form of the distribution and not in its absolute normalisation. Carrying out the integration on energy and on the azimuthal angle, we obtain

$$\overline{N}_{ev} \propto 2\pi \frac{\overline{\gamma}^{3-s}}{s-3} (\overline{\mu} + \overline{\beta}_{\mathrm{s}}) \overline{g}(\overline{\mu}) d\overline{\mu} \,. \tag{4.22}$$

When we compute the contribution of each event to $\overline{g}(\overline{\mu})$, we must also include the factor w_{stat} accounting for the statistical weight of the electron which generated the shock crossing event under consideration.

The last detail to take into account concerns the way particles are injected into the Monte Carlo simulation. In fact, in a steady state we want to reproduce a stationary injection rate at the shock front. This is realised starting N_0 trajectories at $x_{\text{sh}} = 0$ in SRF, which simulates the injection rate $Q_0 = N_0/\Delta t$. This is an additional weighting factor carried by each electron. However, given that the simulation is performed alternately in URF and DRF, we must accordingly transform Q_0 into $\overline{Q}_0$ using $\overline{\Delta t} = \overline{\Gamma}_s \Delta t$ (and into $\widetilde{Q}_0$ using $\widetilde{\Delta t} = \widetilde{\Gamma}_s \Delta t$). Eventually, the density of particles with $\overline{\mu}$ is given by the sum of events in the range $[\overline{\mu} : \overline{\mu} + \Delta\overline{\mu}]$, weighted over all previous factors. Explicitly, it reads

$$\overline{g}(\overline{\mu}) = \sum_{\Delta\overline{\mu}} \frac{1}{2\pi(\overline{\mu} + \overline{\beta}_s)\overline{\Gamma}_s} \frac{s-3}{\overline{\gamma}^{3-s}} \frac{w_{\text{stat}}}{\Delta\overline{\mu}} . \tag{4.23}$$

The same treatment and the same final formula for $\widetilde{g}(\widetilde{\mu})$ hold true for events generated in DRF, with all the quantities expressed in DRF.

The previous relation allows us to construct the angular dependence of the phase-space density in URF, for particles crossing the shock from upstream to downstream, and in DRF for particles crossing the shock in the opposite direction. For direct comparison with published results, in the following we will plot the total angular distribution (for particles crossing the shock from upstream to downstream and *viceversa*) in DRF. This is done considering the Lorentz invariance of the function $f(\gamma, \mu)$, which allows us to write

$$\overline{\gamma}^{-s}\overline{g}(\overline{\mu}) = \widetilde{\gamma}^{-s}\widetilde{g}(\widetilde{\mu}) . \tag{4.24}$$

Using the appropriate transformation for $\overline{\gamma}$ in Appen A (Eq. A.20), we can express in DRF the angular distribution of particles travelling from upstream into downstream with

$$\widetilde{g}(\widetilde{\mu}) = \Gamma_{\text{rel}}^{-s}(1 - \beta_{\text{rel}}\widetilde{\mu})^{-s} \overline{g}(\overline{\mu}) . \tag{4.25}$$

With the treatment presented above, we show that the entire procedure to construct the angular distribution from the Monte Carlo simulation results, in all relevant frames of reference, requires the value of the spectral index s, so that the first step in the analysis must be the extraction of the spectrum. However, it is worth saying that the different angular distributions at the shock determine the spectrum and not *viceversa*, as we shall see in the next section.

Only crossing events generated by electrons which have executed at least 5 complete cycles across the shock front are included in the construction of the angular distribution. We take this precaution to avoid the influence of the injection conditions.

4.5   Results of Monte Carlo simulation

With the code described in the previous section, we simulate the first-order Fermi acceleration process at a relativistic shock front in different regimes. With this, we mean that we investigate different situations in which the scattering agent in the shock upstream is either magnetic fluctuations or an ordered magnetic field, or a combination of the two. In the downstream, instead, we always assume magnetic turbulence to be the only source of particle deflection. The relative importance of the ordered and turbulent part of the magnetic field produces different angular distributions and different spectral slopes.

4.5.1 Pure scattering

Firstly we investigate a situation in which pure scattering off magnetic turbulence is the only source of particle deflection on both sides of the shock. The electric field vanishes both upstream and downstream. The presence of irregularities in the magnetic structure is simulated via *pitch-angle* scattering as presented above. Such a situation has been studied by [81] with a semi-analytical approach from mildly to ultra-relativistic shock speeds. The reason for this study is the test of our Monte Carlo code.

We run the simulation for different Lorentz factor of the shock $\overline{\Gamma}_s\overline{\beta}_s = 0.1, 0.5, 1.0, 2.0, 10.0, 100.0$ and for each case we compute the speed of the downstream plasma $\widetilde{\beta}_s = \overline{\beta}_s/r$ using the shock compression ratio r given by the Jüttner/Synge equation of state for a strong shock [81]. In Fig. 4.1 we show the results of our Monte Carlo code (red points and curves) compared with the results of the eigenfunction approach used by [81] (black solid curves). The results of the Monte Carlo simulation for $\overline{\Gamma}_s\overline{\beta}_s = 100.0$ are compared with the curve obtained for $\overline{\Gamma}_s\overline{\beta}_s = 10.0$ since for $\overline{\Gamma}_s\overline{\beta}_s \geq 10.0$ the eigenfunction results are essentially indistinguishable from the asymptotic solution at $\overline{\Gamma}_s\overline{\beta}_s \to \infty$. This feature is also reproduced by our code. Our results, obtained starting 4000 trajectories for each value of $\overline{\Gamma}_s\overline{\beta}_s$, are in excellent agreement with the results of the semi-analytical approach. The only large discrepancy is in correspondence of the vertical black dashed line, which represents the value of the speed of the shock in DRF $\widetilde{\beta}_s$. This line divides electrons crossing from downstream to upstream on the left-hand side from electrons crossing from upstream to downstream on the right-hand side. This is a sampling error inherent to the Monte Carlo technique also noticed by [2]. It is due to the fact that particles take finite steps in angle. Thus, there are few particles in the simulation that can cross the shock in both directions after only few time steps and few deflections. In this case, the Monte Carlo approach is not very efficient in simulating the continuous deflection undergone by particles. However, this is limited to a very narrow range of $\widetilde{\mu}$ and does not affect the overall reconstruction of the angular distribution or of the energy spectrum.

In the top left panel of Fig. 4.1, we see that the angular distribution for a mildly relativistic shock $\overline{\Gamma}_s\overline{\beta}_s = 0.1$ is almost isotropic. Electrons efficiently diffuse in $\widetilde{\mu}$ and the density of particles grazing the shock front ($\widetilde{\mu} \sim -\widetilde{\beta}_s = -0.07$) and running against it ($\widetilde{\mu} \sim -1$ for electrons downstream and $\widetilde{\mu} \sim +1$ for electrons upstream) is about the same (see Fig. A.1 in Appen. A for a sketch of the simulated geometry). When the shock speed increases, instead, large anisotropies are introduced in the angular distribution. The reason is twofold. Firstly, even if scattering is able to isotropise the distribution of particles downstream, it becomes more difficult to fulfill the condition $\widetilde{\mu} < -\widetilde{\beta}_s$ to cross into the upstream, because $\widetilde{\beta}_s$ increases and, upon shock crossing, the particles and the shock travel in opposite directions. Secondly, in the upstream particles have less time to diffuse before they are overtaken by a fast shock. This reduces the average deflection to an angle of the order of $1/\overline{\Gamma}_s$ in URF and, consequently, it is less likely that a particle hits the shock head-on. When boosted into DRF, this results in the lack of particles at $\widetilde{\mu} \sim +1$ for the ultra-relativistic cases. The bottom right plot in Fig. 4.1 constitutes the asymptotic form of the angular distribution of electrons accelerated at relativistic shocks where the only source of deflection is scattering on both sides of the shock. We see in fact that the result of the Monte Carlo simulation for $\overline{\Gamma}_s\overline{\beta}_s = 100.0$ are in very good agreement with the semi-analytical result for $\overline{\Gamma}_s\overline{\beta}_s = 10.0$. This means that the angular distribution does not change if we increase the shock Lorentz factor $\overline{\Gamma}_s\overline{\beta}_s$. This result indeed confirms the finding of [2].

The effect of the changes in the angular distribution on the spectral slope are shown in the left panel of Fig. 4.2, where the red points are the results of our numerical code, while the black solid curve represents the results of [81]. We see that when the shock is only mildly relativistic and its speed slightly increases ($\overline{\Gamma}_s\overline{\beta}_s \lesssim 1.0$) the loss of
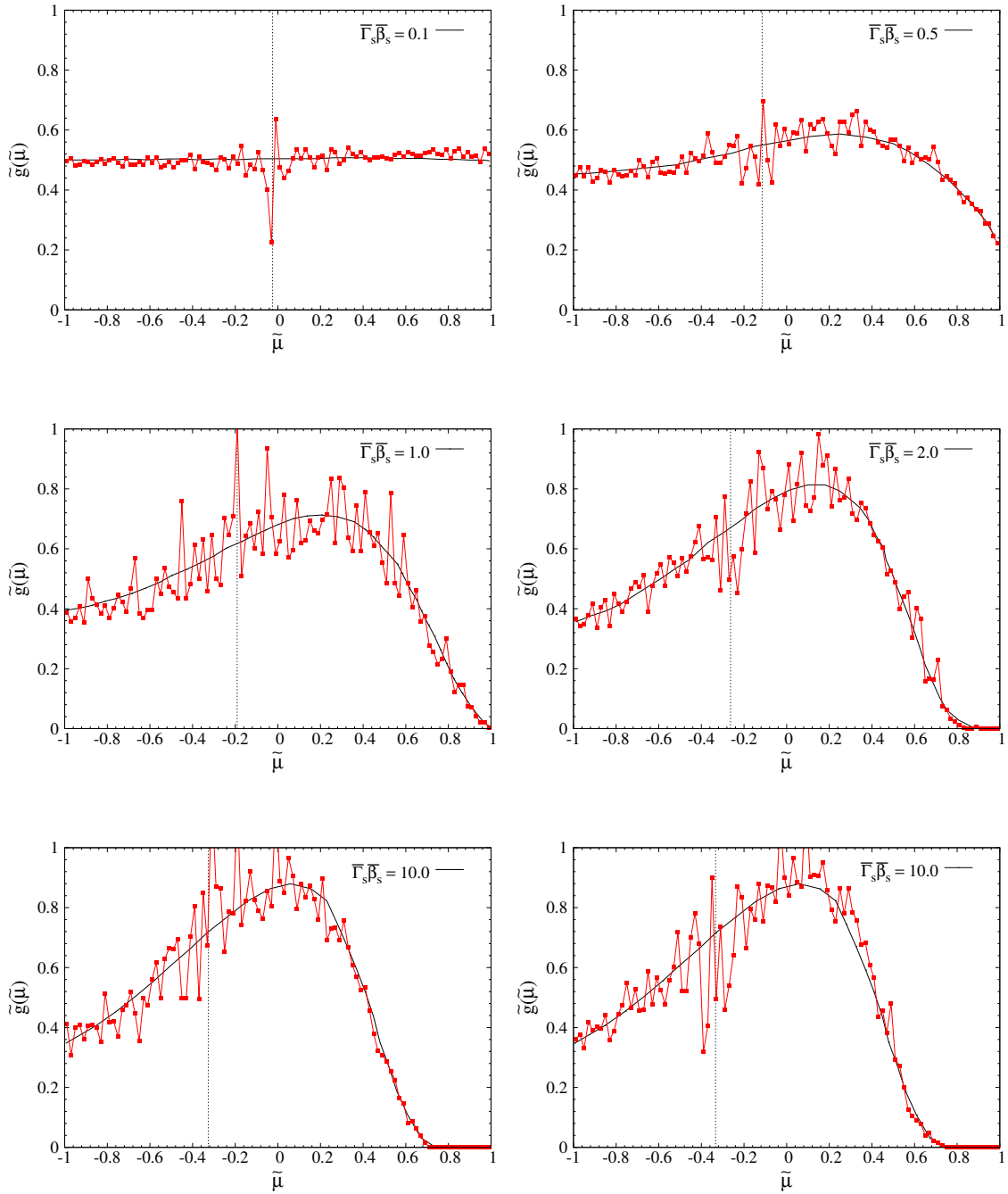
Figure 4.1: Total angular distribution expressed in DRF for different values of $\overline{\Gamma}_s \overline{\beta}_s$. The results of the simulation (red points and curves) are compared with the semi-analytical results of [81] (black solid curves). The vertical black dotted line represents the speed of the shock in DRF $\widetilde{\beta}_s$, dividing electrons crossing from downstream to upstream on the left-hand side from electrons crossing from upstream to downstream on the right-hand side.
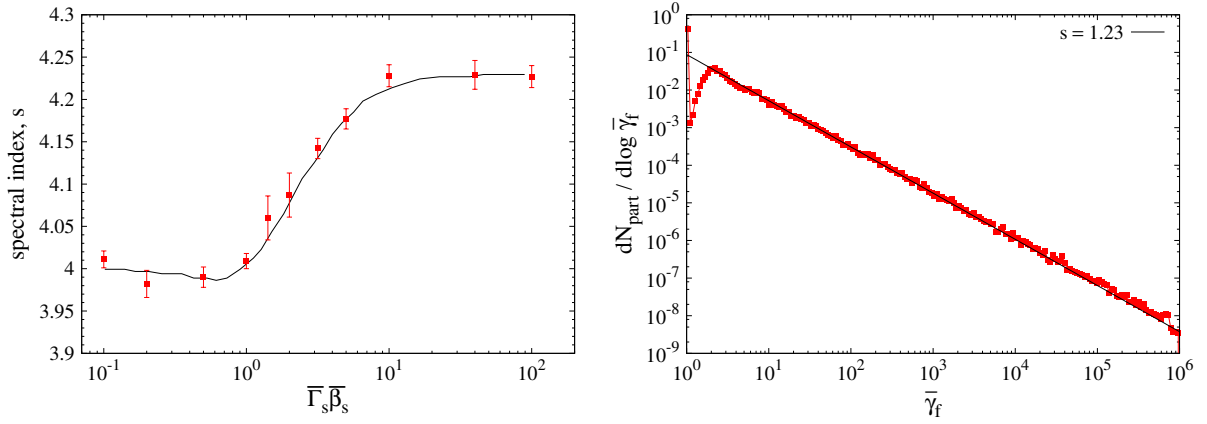
Figure 4.2: Left panel: Spectral index s as a function of the speed of the shock $\overline{\Gamma}_s \overline{\beta}_s$; the red points are the results of our Monte Carlo simulations, the black solid curve curve is the result of [81]. Right panel: Energy spectrum for the specific case of $\overline{\Gamma}_s \overline{\beta}_s = 10.0$; the black solid line is the fit to the red data points.

particles encountering the shock head-on is compensated by the larger energy gain per shock crossing, so that the acceleration mechanism is more efficient and the resulting spectrum slightly flattens. On the other hand, when the speed of the shock becomes fully relativistic, the variation of the angular distribution is more substantial due to the increased loss of particles downstream and to the smaller average deflection allowed upstream. As a consequence, the efficiency of the acceleration drops and the spectrum softens. However, the softening does not proceed indefinitely for two reasons. Firstly, the loss probability downstream depends on the speed of the shock in DRF, and this tends to the asymptotic value $\widetilde{\beta}_s \sim 1/3$ for a strong shock [79]. Secondly, the large energy boost that particles crossing from upstream to downstream would experience when the Lorentz factor is very large is compensated by the smaller deflection that these very same particles can undergo before they are overtaken by the shock front (see Eq. 4.17).

In the right panel of Fig. 4.2 we show as an example the energy spectrum obtained for $\overline{\Gamma}_s \overline{\beta}_s = 10.0$, which is plotted as a function of the ratio of the energy recorded upon shock crossing to the injection energy $\overline{\gamma}_f = \overline{\gamma}/\overline{\gamma}_{inj}$. In this way, we stress that the spectral slope does not depend on the injection energy of the particles undergoing the acceleration process, as long as $\overline{\gamma} > \overline{\Gamma}_s$. The deviation from a pure power-law that we observe for low values of $\overline{\gamma}_f$ is produced by the first shock crossing events, which are still affected by the initial conditions. To avoid this influence, the fit of the energy spectrum is performed for $\overline{\gamma}_f > 30$ as done in [2]. The energy range over which we fit the spectrum encompasses almost five orders of magnitude, up to $\overline{\gamma}_f = 10^6$.

4.5.2   Regular deflection by magnetic field

Another interesting case to investigate is one in which the electric field vanishes on both sides on the shock and there is a static and uniform magnetic field in the upstream, whose direction is perpendicular to the shock normal.

Note that we are not saying that magnetic turbulence are not present. Rather, we assume that the relative strength of the ordered and turbulent part of the magnetic field is such that the dominant source of particle deflection is the ordered component of the field. On the downstream side only scattering is simulated. We again run the Monte Carlo simulation for different values of the Lorentz factor of the shock, and we compare our results with [2]. In Tab. 4.1 we collect the values of the spectral index we find for two values of the shock Lorentz factor. Our results are

$\overline{\Gamma}_s \overline{\beta}_s$	s^a	s^b
10	4.28 ± 0.01	4.28 ± 0.01
100	4.30 ± 0.01	4.30 ± 0.01

[a] this work

[b] Achterberg *et al.* (2001) [2]

Table 4.1: Power-law index *s* for different values of the shock Lorentz factor for a situation in which a static and uniform magnetic field perpendicular to the shock normal deflects electrons upstream of the shock. Downstream the source of deflection is pure scattering.

in very good agreement with our reference. In the left panel of Fig. 4.3 we show, as an example for the simulated conditions, the angular distribution we construct for $\overline{\Gamma}_s \overline{\beta}_s = 100.0$ (red points and curve) in comparison with the results of Monte Carlo simulation from [2] (blue points and curve) and the semi-analytical results of [81] (solid
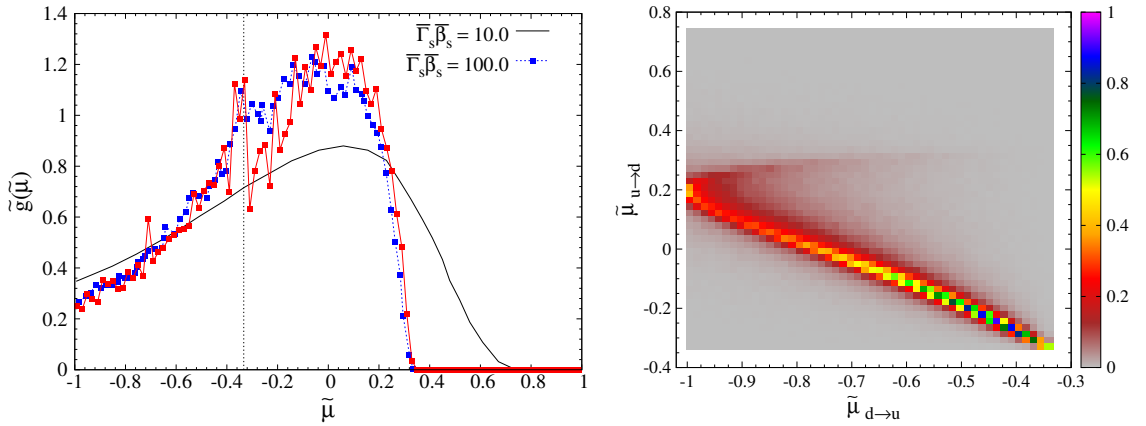
Figure 4.3: Left panel: Total angular distribution at the location of an ultra-relativistic, perpendicular shock front for $\overline{\Gamma}_s \overline{\beta}_s = 100.0$; the source of electron deflection is magnetic field upstream and scattering downstream. Our results (red points and curve) are compared with those of [2] (regular deflection, blue points and curve) and [81] (pure scattering, black curve). Right panel: Map of the probability a particle has to cross the shock front from upstream to downstream with $\widetilde{\mu}_{u \to d}$, provided that it entered the upstream with $\widetilde{\mu}_{d \to u}$.

black curve[4]). The angular distribution generated by the ordered magnetic field shows remarkable differences with respect to the previous case, in particular for electrons crossing from upstream to downstream (on the right-hand side of the vertical black dotted line). These particles tend to accumulate in the range $\widetilde{\mu}[-0.333 : 0.2]$ and the number of electrons which experience large deflections is severely reduced. This turns in the harder spectral index computed in this situation (see Tab. 4.1) as compared to the pure scattering case.

An alternative and complementary way to study the angular distribution is given in the right panel of Fig. 4.3, where we plot the probability a given electron has to cross the shock from upstream to downstream with $\widetilde{\mu}_{u \to d}$ as a function of $\widetilde{\mu}_{d \to u}$ with which the particle entered the upstream, as expressed in DRF. The plot can be understood in the following way. Let us assume, without loss of generality, that in our picture of the shock front (Fig. A.1) the magnetic field $\overline{B}$ in URF is directed along the y-axis. A particle in the upstream travels with $\overline{\beta} \sim 1$ and $\overline{\mu} < -\overline{\beta}_s$, but the component of the momentum vector contributing to the gyration about the magnetic field lines is $\overline{\mathbf{p}}_\perp = \overline{p}\,\overline{\mathbf{n}}_\perp$, where $\overline{\mathbf{n}}_\perp$ is the component of $\overline{\mathbf{n}}$, unitary vector in the direction of the momentum (see Eq. 3.1) perpendicular to $\overline{B}$. The magnitude of this component is

$$\overline{n}_\perp = \sqrt{\overline{n}_x^2 + \overline{n}_z^2} = \sqrt{\overline{\mu}^2(1 - \sin^2 \phi) + \sin^2 \phi} \tag{4.26}$$

where ϕ is the angle between the y-axis and the projection of $\overline{\mathbf{n}}$ onto the shock surface. The minimum and maximum values of $\overline{n}_\perp$ are $\overline{n}_\perp = \overline{\mu}_{d \to u}$ for integer multiples of $\phi = \pi$ and $\overline{n}_\perp = 1$ for integer multiples of $\phi = \pi/2$, respectively (in URF we always have $\overline{n}_\perp > \overline{\beta}_s$). According to the initial value of $\overline{\theta}$ when the particle enters the upstream, the gyration about the field can lead the electron to run either directly towards the shock or in front of it. In fact, the projection of the direction of motion onto the x-axis can initially increase or decrease. This is shown in Fig. 4.4, where we emphasise the difference in magnitude between $\overline{\beta}_s$ and 1. We consider a simple situation in which the magnetic field in the upstream is largely dominant with respect to the magnetic fluctuations generating the *pitch-angle* scattering. In this case, the modifications to the unperturbed trajectory of an electron (or positron) moving in the magnetic field are negligible. Thus, we can analytically compute $\overline{\mu}_{u \to d}$ knowing $\overline{\mu}_{d \to u}$. At time $\overline{t} = 0$, when the particle enters the upstream, the position of the particle coincides with the location of the shock front $\overline{x}_e = \overline{x}_{sh} = 0$. Then, the particle starts the (unperturbed) orbit about the magnetic field, while the shock travels into the upstream medium. The time evolution is given by

$$\begin{cases} \overline{x}_e(\overline{t}) = -r \sin(\overline{\theta}_{d \to u} - \overline{\omega}_g \overline{t}) + r \sin \overline{\theta}_{d \to u} \\ \overline{x}_{sh}(\overline{t}) = -\overline{\beta}_s \overline{t} \\ \overline{\mu}_{u \to d}(\overline{t}) = \overline{n}_\perp \cos(\overline{\theta}_{d \to u} - \overline{\omega}_g \overline{t}) \end{cases} \tag{4.27}$$

where $\overline{\omega}_g \propto \overline{B}/\overline{\gamma}$ and $r = \overline{n}_\perp/\overline{\omega}_g$ are the gyro-frequency and the gyro-radius of the orbit, respectively. The second term on the right-hand side of the first relation in Eq. 4.27 accounts for the initial position on the orbit due to the initial $\overline{\theta}$. The angular frequency comes with the minus sign because the calculations are performed for a positron, which gyrates clockwise about the magnetic field, but the procedure is analogous for an electron. Equating the first two expressions in Eq. 4.27 and setting $\psi = (\overline{\theta}_{d \to u} - \overline{\omega}_g \overline{t})$, gives us

$$\sin \psi + K(\psi - \overline{\theta}_{d \to u}) - \sin \overline{\theta}_{d \to u} = 0 \tag{4.28}$$

where $K = \overline{\beta}_s/\overline{n}_\perp$. The solution of Eq. 4.28 allows us to compute $\overline{\mu}_{u \to d}$ independently of the specific values of $\overline{B}$ and $\overline{\gamma}$ for different values of $\overline{\theta}_{d \to u}$ and $\overline{\beta}_s$. We solve this transcendent equation for ψ with a bisection numerical

---

[4]These are the results of [81] for $\overline{\Gamma}_s \overline{\beta}_s = 10.0$, for pure scattering.
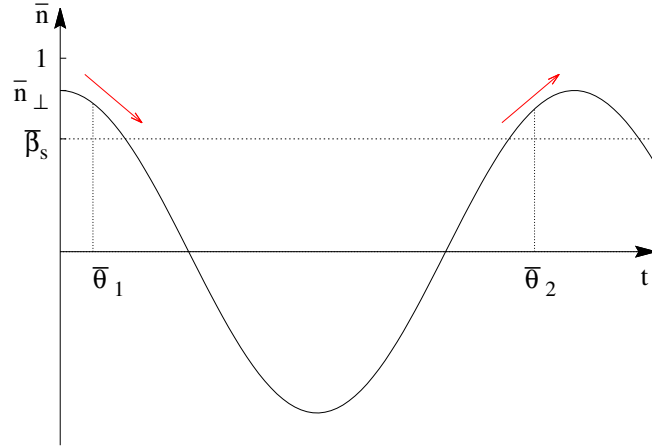
Figure 4.4: Sketch of the behaviour of the projection $\overline{n}_\perp$ of the direction of motion $\overline{\mathbf{n}}$ onto the plane perpendicular to $\mathbf{B}$ (in this case xz-plane). According to the initial angle $\overline{\theta}$, the gyration leads the electron to travel towards the shock (for $\overline{\theta}_1$) or in front of it (for $\overline{\theta}_2$).

algorithm and we finally obtain $\overline{\mu}_{u\to d}$ plugging the result in the third relation of Eq. 4.27. The solution is obtained for all $\overline{\theta}_{d\to u}$ satisfying $\overline{\mu}_{d\to u} < -\overline{\beta}_s$ ($\overline{\Gamma}_s\overline{\beta}_s = 100.0$) and for ϕ [0 : 2π]. The result is then boosted in DRF. The region occupied in the $\widetilde{\mu}_{d\to u} - \widetilde{\mu}_{u\to d}$ probability map by the solution of Eq. 4.28 is shown in Fig. 4.5. We can see that, although the crossing events in the plot in the right panel of Fig. 4.3 populate a region of the map which is allowed by Eq. 4.28, the two plots are far from being compatible. This is due to the combined actions of the fast shock
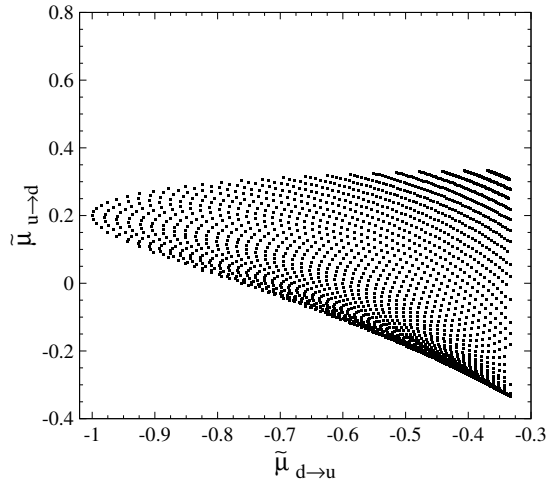
Figure 4.5: Allowed region for the solution of the transcendent Eq. 4.28 in the $\widetilde{\mu}_{d\to u} - \widetilde{\mu}_{u\to d}$ probability map.
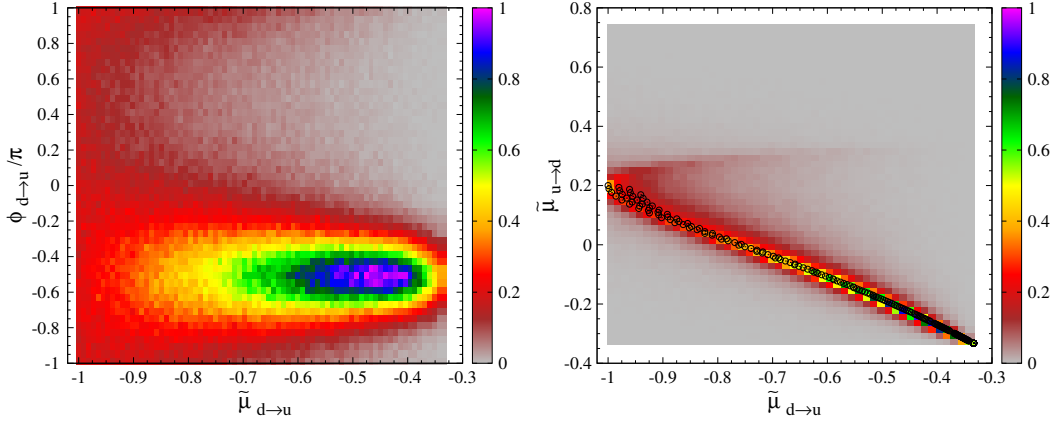
Figure 4.6: Left panel: Phase ϕ about the y-axis, in units of π, plotted against the cosine of the polar angle for positrons crossing the shock from downstream to upstream. Right panel: Solution of Eq. 4.28 for the appropriate values of $\overline{\theta}_{d\to u}$ and $\phi_{d\to u}$ for deflection in magnetic field over-plotted in black circles to the right panel of Fig. 4.3.

overtaking the electrons and of the magnetic field selecting specific phases ϕ of particles gyrating about the field lines. The picture is the following. At the very beginning of the simulation, electrons and positrons are injected at the shock (in URF) with randomly distributed ϕ. Both species gyrate about the magnetic field (in opposite directions) and they cross into the downstream. At this point, in case they cross the shock into the upstream once more, the average value of the new phase depends on the time they spend in the excursion downstream. In general, if they cross very soon, they do not have a long time to diffuse and both $\overline{\theta}$ and ϕ do not change significantly, so that $\overline{\mu}_{d\to u} \lesssim -\overline{\beta}_s$ and $\phi_{d\to u} \sim \phi_{u\to d}$. In the subsequent excursion upstream, then, the phase is such that the particle immediately gyrates towards the shock, rather than away from it (Fig. 4.4 helps visualising this). Through this mechanism, the phases of electrons and positrons tend to accumulate around a specific value. On the other hand, if particles spend a long time in the downstream before re-crossing the shock, the value of both $\overline{\theta}$ and ϕ can change by a larger amount. The picture that we describe here is shown for positrons in the left panel of Fig. 4.6, where we plot the phase of particles crossing the shock from downstream to upstream $\phi_{d\to u}$ against $\widetilde{\mu}_{d\to u}$. We see that the distribution is fairly narrow about $\phi_{d\to u} \sim -\pi/2$ (the situation is analogous for electrons, whose distribution peaks at $\phi_{d\to u} \sim \pi/2$). The value of $\phi_{d\to u}$, combined with the information on $\overline{\mu}_{d\to u}$, allows us to compute the polar angle $\overline{\theta}_{d\to u}$, which is the polar angle of a particle upon entering the upstream. Now, solving Eq. 4.28 for the appropriate values of $\overline{\theta}_{d\to u}$ and $\phi_{d\to u}$, we obtain a much better agreement between the analytical approach and the results of the Monte Carlo simulation. We show this in the right panel of Fig. 4.6, where the analytical solution is over-plotted in black circles to the results of the simulation plotted in the right panel of Fig. 4.3. It is still possible to see a small deviation of the simulation data from the expected behaviour for $\widetilde{\mu}_{u\to d} \gtrsim 0.2$, which seems to form a secondary branch in the map. The reason for this is that, as mentioned above, particles with $\widetilde{\mu}_{d\to u}$ close to -1 have usually spent a long time in the downstream, so that their phase upon crossing is not constrained in a small range about $-\pi/2$ (see left panel in Fig. 4.6). For these specific positrons, the gyration about the magnetic field lines makes

them fly away from the shock, before driving them towards it.

4.5.3 Deflection in pulsar wind

The investigation of first-order Fermi acceleration in known situations provided an excellent testbed for our Monte Carlo code. Now, we study the effects of the striped pulsar wind on this acceleration process.
The set-up is similar to that used for the simulation of the previous cases and is suitable to simulate electron acceleration in a stationary state at the pulsar wind termination shock. Downstream of the TS, the source of particle deflection is pure scattering, while upstream we prescribe both ordered and disordered field components. The shock front lies in the *yz*-plane and its normal is directed along the *x*-axis, as shown in Fig. A.1. In the SRF, the upstream and downstream flows move in the positive *x* direction with $\overline{\beta}_s$ and $\widetilde{\beta}_s$, respectively. The magnetic fluctuations on both sides of the shock are realised through the *pitch-angle* scattering, in the way described above. The ordered magnetic field structure is defined in SRF via Eqs. 2.12 and 2.13, *i.e.*, the analytic form of the transverse, circularly polarised, magnetic shear wave. Given that the simulation is performed in the local fluid frame, we Lorentz transform the two relations into URF using Eqs. A.34 and A.35, which give

$$\overline{B}_y = +\overline{B}_0 \cos(\overline{k}_0 \overline{x} + \Phi) \tag{4.29}$$

$$\overline{B}_z = -\overline{B}_0 \sin(\overline{k}_0 \overline{x} + \Phi) \tag{4.30}$$

where $\overline{B}_0 = B_0/\overline{\Gamma}_s$ and $\overline{k}_0 = k_0/\overline{\Gamma}_s$ are the dimensionless magnetic field and wavenumber in URF, respectively, and Φ is an initial phase set to a different random value every time an electron enters into the upstream. We do this under the assumption that the scattering length in the DRF, *i.e.*, the average distance over which a particle is deflected by an angle $\widetilde{\theta}_c \sim 1/\widetilde{\Gamma}_s$, is much larger than the wavelength of the wave expressed in the same frame $\widetilde{L}_{scat} \gg \widetilde{\lambda}$. This means that the phase of the wave when a particle ends an excursion downstream is completely unrelated to the phase of the wave when the same excursion starts. Such an assumption is justified if the level of turbulence downstream is limited and particle deflection is not very efficient on the length-scale of the field wavelength. In the URF, the electric field vanishes because of the frozen-in condition (see Eqs. A.36-A.38 in Appen. A). Equations 4.29 and 4.30 determine a stationary magnetic pattern which rotates in space with wavelength

$$\overline{\lambda} = \frac{2\pi}{\overline{k}_0} = \frac{2\pi}{\Omega}\overline{\beta}_s\overline{\Gamma}_s \tag{4.31}$$

in the plane of the shock, so that the shock is perpendicular. To be fully consistent with the discussion and the results of Chapt. 2, we use the same normalisations for time, space, velocity, density and magnitude of the magnetic field as presented in Sect. 2.2.
Upstream of the shock front there are three characteristic length scales, namely the field wavelength $\overline{\lambda}$, the scattering length $\overline{L}_{scat} = 1/2\overline{D}_\theta$ and the energetic particle gyro-radius $\overline{r}_g = m\overline{\gamma}/e\overline{B}_0$. However, it is worth mentioning that, since we are dealing with an acceleration mechanism, the gyro-radius is not constant at different stages of the process. At injection, the particle energy is minimum as well as the gyro-radius $\overline{r}_{g,min}$, but as the number of Fermi cycles increases, the gyro-radius grows larger. We define $\overline{r}_{g,max}$ the average gyro-radius of particles removed from the simulation when they complete the maximum number of cycles. The relative magnitude of these quantities determines different acceleration regimes, arising because of the competition between regular magnetic field deflection and scattering.
The first distinction can be done according to the values of $\overline{L}_{scat}$ and $\overline{\lambda}$. Here, we select $\overline{L}_{scat} \gg \overline{\lambda}$ for the following

reason. In Chapt. 3 we found that the turbulent electromagnetic fields at the pulsar TS generated by the dissipation of the Poynting flux are able to reflect a fraction of the test particles upstream and energise them up to energies $\overline{\gamma} \approx \sigma_0 \overline{\Gamma}_s^2$. In the idealised situation of the two-fluid simulation, once these particles propagate in the unperturbed magnetic shear wave, further acceleration is prevented by the lack of turbulence able to deflect them again towards the shock. In reality, however, some inhomogeneities are always present, although at a much lower level than in the precursor. The goal of this section is to simulate the presence of such a turbulence, which is not resolved in the two-fluid simulation and acts on a much longer scale with respect to $\overline{\lambda}$. Thus, we consider $\overline{L}_{scat} \gg \overline{\lambda}$ and we analyse the regimes arising for $\overline{r}_g \ll \overline{\lambda}$ and $\overline{r}_g \gg \overline{\lambda}$.

Even when the magnetic field of the shear wave is unperturbed by inhomogeneities, the trajectory of an electron in a circularly polarised, sinusoidal magnetic field has a complex pattern. In fact, when $\overline{r}_g \ll \overline{\lambda}$, an electron starting its trajectory at any given point does not travel deep enough into the magnetic structure to experience the rotation of the magnetic field vector. As a consequence, such an electron essentially gyrates about a uniform and static magnetic field. In this regime, particles are fully magnetised and the deflection of the trajectory due to the magnetic field is sufficient for a particle to cross into the downstream. However, when the gyro-radius and the field wavelength are comparable, the direction of the magnetic field changes substantially during the particle trajectory in such a way that, at some point during the orbit, the field has opposite direction with respect to the starting point. When the particle encounters the opposite phase of the field, it gyrates in the opposite direction. As a consequence, the electron gyrates about the rotating magnetic field in a wiggling pattern, without ever finishing one complete gyration. Eventually, when $\overline{r}_g \gg \overline{\lambda}$ this effect is maximised and the trajectory resembles a straight line with very little curvature. Hence, there is a critical value of the gyro-radius, and consequently of the particle energy, at which the magnetic field is no more able to deflect the electron enough for the shock front to overtake it. This happens when the ratio of the wavelength to the particle gyro-radius is

$$\frac{\overline{\lambda}}{\overline{r}_g} \approx \overline{\theta}_c \approx \frac{1}{\overline{\Gamma}_s} \, . \tag{4.32}$$

For the value of $\overline{r}_g$ satisfying Eq. 4.32 (or equivalently for the value of $\overline{\gamma}$), only scattering is able to provide the deflection necessary for a particle to cross the shock into the downstream. When $\overline{r}_g \gg \overline{\lambda}$, the magnetic field is unimportant and scattering dominates the particle trajectories. In this regime, particles are fully unmagnetised and only scattering is responsible for particle deflection.

The magnetic field-dominated and the scattering-dominated regimes are expected to produce spectra with different slopes. The energy of the spectral break between the two regimes is computed from Eq. 4.32 to be $\overline{\gamma}_{sb} \propto \overline{\Gamma}_s \overline{\lambda} \overline{B}_0$. A Monte Carlo run which encompasses the full range of gyro-radius from $\overline{r}_g \ll \overline{\lambda}$ to $\overline{r}_g \gg \overline{\lambda}$ is computationally expensive and does not allow to disentangle the contributions to the angular distribution coming from the two acceleration regimes. Thus, we investigate values of $\overline{B}_0$, Ω and α corresponding to the two regimes: regime I for $\overline{r}_g \ll \overline{\lambda}$ and regime II for $\overline{r}_g \gg \overline{L}_{scat}$. The parameter α (Eq. 4.15) determines the maximum aperture of the scattering cone in the *pitch-angle* scattering routine and consequently the diffusion coefficient (Eq. 4.18) and the scattering length $\overline{L}_{scat} = 1/2\overline{D}_\theta$. For each regime we present the resulting stable state angular distribution, the $\widetilde{\mu}_{d\to u} - \widetilde{\mu}_{u\to d}$ map and the spectral index. All the results are shown for a shock Lorentz factor $\overline{\Gamma}_s \overline{\beta}_s = 10.0$, which is a good approximation of the asymptotic behaviour in ultra-relativistic situations, as shown is Sec. 4.5.1.

Regime I: $\overline{r}_{g,max} \ll \overline{\lambda} \ll \overline{L}_{scat}$

In regime I the ordered part of the striped-wind configuration dominates over the fluctuations and the particle gyro-radius is the smallest length scale into play. In this regime, every electron entering the upstream essentially encounters an almost uniform and static magnetic field, since it does not travel far enough into the sinusoidal rotating magnetic pattern before the field deflects it towards the shock front. In principle, this situation is similar to the one presented in Sect. 4.5.2, but with an important difference. When the field is static and uniform in the upstream, every electron crossing the shock into the upstream encounters the same configuration of the magnetic field and gyrates in the same direction, and the results are shown in the two panels of Fig. 4.3. On the other hand, in this case electrons entering the upstream encounter a different phase Φ of the magnetic shear wave. This is due to the fact that we simulate a stationary state at the shock front. As a consequence, the phase ϕ of particles crossing and re-crossing the shock front does not accumulate about a specific value, as it was the case in Sec. 4.5.2 (see Fig. 4.6 and related text). Instead, it remains uniformly distributed, as it is shown in the left panel of Fig. 4.7, where the phase $\phi_{d\rightarrow u}$ of particles crossing the shock from downstream to upstream is plotted against $\widetilde{\mu}_{d\rightarrow u}$. In the right panel of Fig. 4.7 we plot the related $\widetilde{\mu}_{d\rightarrow u} - \widetilde{\mu}_{u\rightarrow d}$ map and we observe that, contrary to the case of normal magnetic field deflection presented above, the double branch structure is clearly visible. This is simply due to the fact that the distribution of the phase ϕ is uniform, so that it is equally probable, for a particle crossing into the upstream with $\widetilde{\mu}_{d\rightarrow u}$, to be on the falling or rising part of the curve plotted in Fig. 4.4. In other words, there is the same probability that the gyration of the trajectory leads the particle to run towards the shock or in front of it. Also in this case we can solve Eq. 4.28 for the appropriate values of $\overline{\theta}_{d\rightarrow u}$ and $\phi_{d\rightarrow u}$ to compute the expected behaviour. We obtain an excellent agreement between the analytic solution of Eq. 4.28 and the simulation data, as we show in the left panel of Fig. 4.8. The right panel in Fig. 4.8 shows the angular distribution obtained in regime I (red points and curve), compared with the results of the eigenfunction method of [81] for $\overline{\Gamma}_s \overline{\beta}_s = 10.0$ (case of pure scattering, solid black
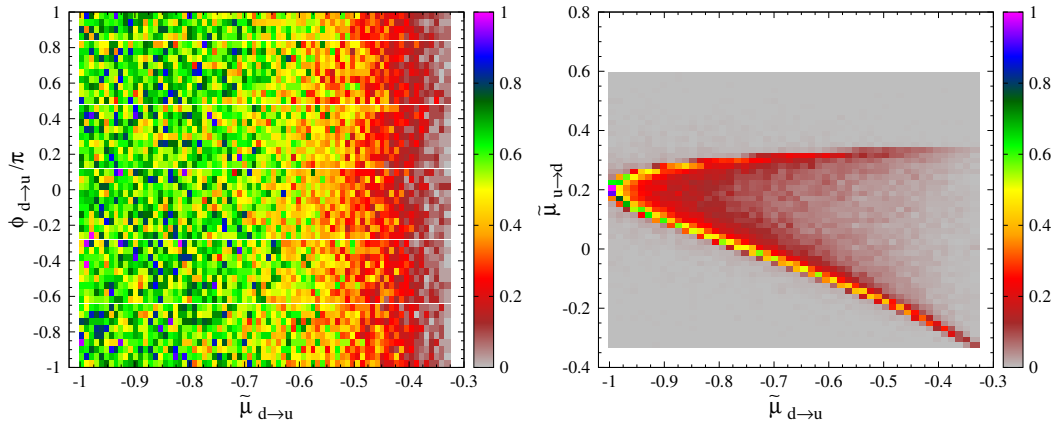

Figure 4.7: Left panel: Phase ϕ about the *y*-axis, in units of π, plotted against the cosine of the polar angle, for positrons crossing the shock from downstream to upstream. Right panel: $\widetilde{\mu}_{d\rightarrow u} - \widetilde{\mu}_{u\rightarrow d}$ map for regime I.
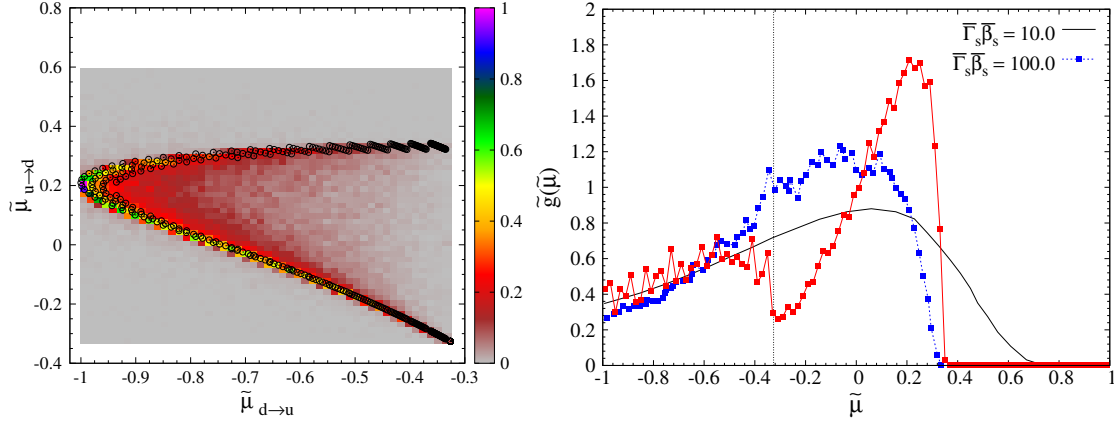
Figure 4.8: Left panel: Solution of Eq. 4.28 for the appropriate values of $\overline{\theta}_{d\to u}$ and $\phi_{d\to u}$ for regime I over-plotted in black circles to the right panel of Fig. 4.7. Right panel: Angular distribution for regime I (red points and curve) compared with the results of [81] (case of pure scattering, solid black curve) and those of [2] (case of regular deflection upstream, blue curve and points).

curve) and those of the Monte Carlo simulation of [2] for $\overline{\Gamma}_s\overline{\beta}_s = 100.0$ (case of regular deflection upstream, blue curve and points). We see that the distribution differs not only from the case of pure scattering, as expected, but also from the case of regular deflection, in particular in the part produced by particles crossing from upstream to downstream. The reason is that electrons populating the upper branch of the $\widetilde{\mu}_{d\to u} - \widetilde{\mu}_{u\to d}$ map reach larger values of $\widetilde{\mu}_{u\to d}$ with respect to the previous case. In fact they initially run in front of the shock and they have more time to gyrate about the field lines. The crossing events generated by this population generates a peak in the angular distribution at $\widetilde{\mu}_{u\to d} \sim 0.2$. At the same time, there are less particles initially travelling towards the shock front, that is why there is a dip in the region of small final deflection close to $\widetilde{\mu}_{u\to d} = -\widetilde{\beta}_s$. The resulting spectral index is $s = 4.29 \pm 0.01$, only slightly softer than, but still compatible to, the one obtained in Sect. 4.5.2 for $\overline{\Gamma}_s\overline{\beta}_s = 10.0$ (see Tab. 4.1).

For completeness, we also investigate the intermediate regime in which $\overline{r}_g \approx \overline{\Gamma}_s\overline{\lambda}$, corresponding to the energy of the spectral break. When injected, particles have $\overline{r}_g < \overline{\lambda}$ and are essentially in the same situation described above, namely they experience an almost uniform magnetic field. However, some particles are accelerated to high Lorentz factors and their gyro-radius becomes comparable and then larger than $\overline{\lambda}$. As explained above, these particles do not run a complete gyration about the field lines before the magnetic field changes direction. Consequently the resulting trajectory wiggles about the field, which becomes less efficient in deflecting electrons towards the shock as the energy increases. For this population of electrons the deflection due to magnetic fluctuations becomes more important, up to the point in which scattering is the only mechanism able to change enough $\overline{\theta}$, so that they can be over-run by the shock front. The effects of this intermediate regime can be observed in the $\widetilde{\mu}_{d\to u} - \widetilde{\mu}_{u\to d}$ map, plotted in left panel of Fig. 4.9. The low-energy electrons, which are in the field-dominated regime, still form the double branch pattern in the map. However, the pattern is blurred by the shock crossing events generated by the high-energy electrons, which are in the scattering-dominated regime. These events can deviate substantially from
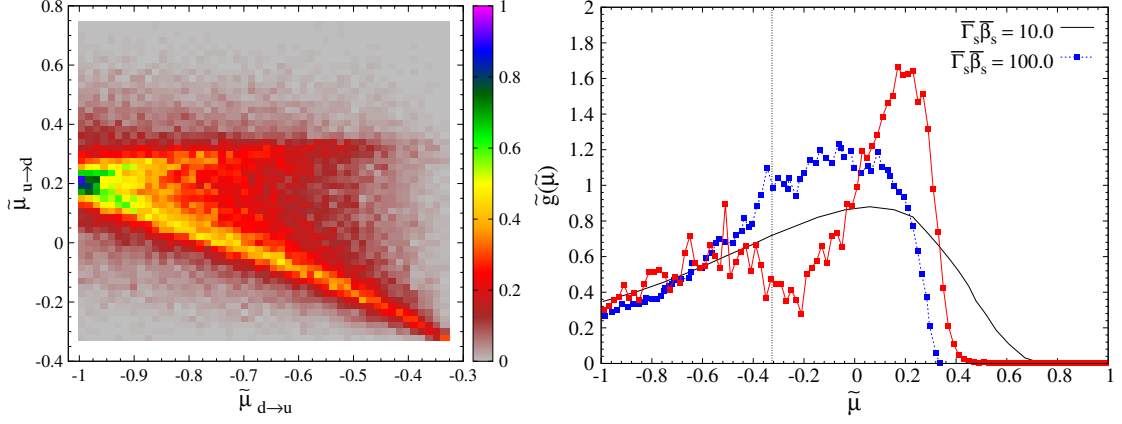
Figure 4.9: Left panel: $\widetilde{\mu}_{d\to u} - \widetilde{\mu}_{u\to d}$ map for the intermediate regime. Right panel: Angular distribution for the intermediate regime (red points and curve) compared with the results of [81] (case of pure scattering, solid black curve) and those of [2] (case of regular deflection upstream, blue curve and points).

the behaviour expected in the field-dominated case, as it is visible in the plot. We observe that the blur is mostly evident in the regions between the two branches and above the upper branch, for $\widetilde{\mu}_{u\to d} \gtrsim 0.3$, which are completely empty in regime I. As a result, in the angular distribution plotted in the right panel of Fig. 4.9, the dip close to $\widetilde{\beta}_s$ is less pronounced and the peak at $\widetilde{\mu}_{u\to d}$ is wider.

In this case we do not provide a spectral index for the particle spectrum, as this is the energy range where the spectral break between regime I and regime II is expected. In addition, the simulated energy range is not wide enough to resolve the change of spectral slope between the field-dominated and the scattering-dominated regimes.

Regime II: $\overline{\lambda} \ll \overline{L}_{\textbf{scat}} \ll \overline{r}_{\textbf{g,min}}$

In regime II the magnetic field of the pulsar wind is unimportant. Every particle performs a very small fraction of a complete gyration about the magnetic field before encountering the opposite phase of the wind pattern. The resulting trajectories are almost straight and the deviation from a straight line is not enough for the shock front to catch up with the electrons. Thus, the scattering off magnetic fluctuations is the only mechanism which is

regime	s
I	4.29 ± 0.01
II	4.23 ± 0.01

Table 4.2: Summary of spectral idexes obtained in the field-dominated regime (regime I) and scattering-dominated regime (regime II).
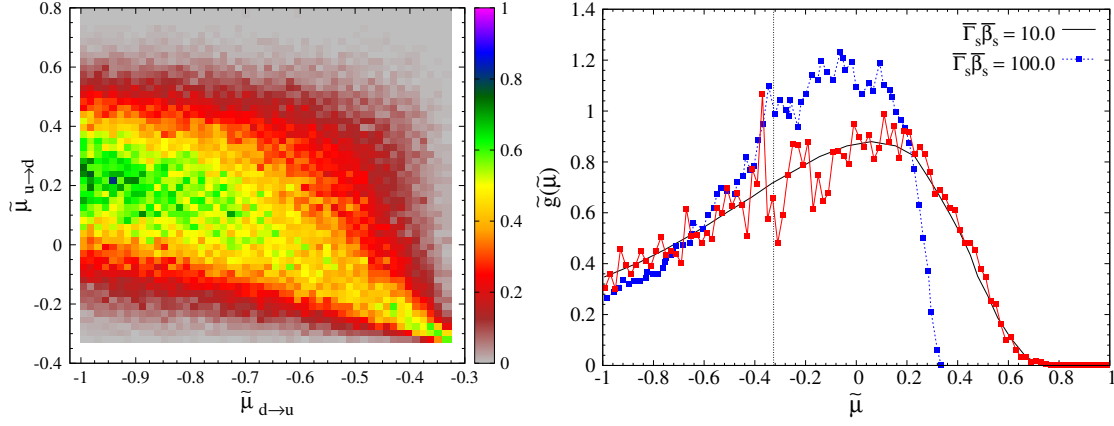
Figure 4.10: Left panel: $\widetilde{\mu}_{d\to u} - \widetilde{\mu}_{u\to d}$ map for regime II. Right panel: Angular distribution for regime II (red points and curve) compared with the results of [81] (case of pure scattering, solid black curve) and those of [2] (case of regular deflection upstream, blue curve and points).

effective in deflecting trajectories into the downstream. In Fig. 4.10 we observe that the double branch structure in the $\widetilde{\mu}_{d\to u} - \widetilde{\mu}_{u\to d}$ map is completely erased and that we obtain the asymptotic form of the angular distribution already presented in the bottom panels of Fig. 4.1. This form of the angular distribution also implies the spectral index $s = 4.23 \pm 0.01$, which is characteristic of a Fermi process driven by scattering on both sides of the shock, when energy losses are neglected. In Tab. 4.2 we summarise the spectral indexes obtained for the two regimes investigated in this work.

Realistic pulsar wind

As we specified above, the simulation parameters $\overline{B}_0$, Ω and α have been regulated to obtain the different acceleration regimes and to investigate the different forms of the $\widetilde{\mu}_{d\to u} - \widetilde{\mu}_{u\to d}$ map, angular distribution and spectrum. However, a part from the strength and spectrum of the magnetic fluctuations, which are difficult to know *a priori*, the definition of the other quantities depends on the features of the pulsar wind, namely the wind Lorentz factor, magnetisation and frequency. Thus, to understand which acceleration mechanism is likely to dominate in a realistic Pulsar Wind Nebula (PWN), we must use values of $\overline{\Gamma}_s$, σ and ω reasonable for this class of sources. Unfortunately, the only parameter that we can measure from observations with good precision is the pulsar frequency ω, whereas rough estimates of $\overline{\Gamma}_s$ and σ must be used to constrain the acceleration regime at the termination shock of a realistic pulsar wind.

We have seen in this section that the different acceleration regimes are determined by the ratio of the wavelength of the striped-wind to the gyro-radius of energetic particles. The striped-wind wavelength in URF is defined in Eq. 4.31. We remind that $\Omega = \omega/\overline{\omega}_{p0}$ is the pulsar frequency in units of the proper plasma frequency, which is expressed in Eq. 1.17, and that the main focus of this work is on frequencies $\Omega > 1$, for which the electromagnetic precursor can form ahead of the wind termination shock. Furthermore, the definition of σ in Eq. 2.10 allows us to

compute the magnitude of the dimensionless magnetic field in the far upstream, which we then transform in URF using Eq. A.39, as

$$\overline{B}_0 = \frac{B_0}{\overline{\Gamma}_{\rm s}} = \sqrt{8\pi\sigma}. \tag{4.33}$$

In this reference frame, the gyro-radius of an electron with energy $\overline{\gamma}$ is

$$\overline{r}_{\rm g} = \frac{m\overline{\gamma}}{e\overline{B}_0} = \frac{\overline{\gamma}}{\sqrt{\sigma}} \tag{4.34}$$

because of the normalisations used in this work[5]. From the results of Chapt. 3, we know that the energy at which electrons are injected in the Fermi acceleration process, *i.e.*, the minimum particle energy, is $\overline{\gamma} \approx \sigma\overline{\Gamma}_{\rm s}^2$. As a consequence, the minimum size of the gyro-radius is $\overline{r}_{\rm g,min} \approx \sqrt{\sigma}\,\overline{\Gamma}_{\rm s}^2$, which entails

$$\frac{\overline{\lambda}}{\overline{r}_{\rm g,min}} = \frac{2\pi\overline{\beta}_{\rm s}}{\Omega\,\sqrt{\sigma}\,\overline{\Gamma}_{\rm s}} \tag{4.35}$$

where σ and $\overline{\Gamma}_{\rm s}$ are the wind magnetisation and Lorentz factor far upstream and not at the termination shock. In fact, energetic electrons have large gyro-radii and can travel a long way into the upstream. In this region, the pulsar wind is Poynting flux dominated ($\sigma \sim 10^4 - 10^5$) and relativistic ($\overline{\Gamma}_{\rm s} \sim 10^2$, see e.g., [71, 23, 9, 40]) so that the ratio in Eq. 4.35 is much smaller than unity for the lower particle energy and hence $\overline{\lambda}/\overline{r}_{\rm g} \ll 1$ for every value of the particle Lorentz factor during the whole acceleration process. This means that, in a realistic pulsar wind, where electrons (and positrons) are injected in a Fermi acceleration process via the interaction with the perturbations in an electromagnetic precursor, the wavelength of the striped-wind pattern is always the smallest length scale into play, which is the condition of the acceleration regime II. Consequently, the dominant particle deflection mechanism is the scattering off magnetic fluctuations embedded in the flow, rather than the gyration about the magnetic field in the stripes. For this situation, when the energy losses are neglected, we know both the form of the angular distribution and the spectral slope at the shock front, which are those of regime II. This completely determines the phase-space distribution function at the shock.

In our framework, the particle acceleration is triggered by the conversion of the striped-wind into superluminal waves which drive the dissipation of the wind Poynting flux and the generation of a population of pre-accelerated electrons upstream of the TS (see Sects. 3.6 and 3.7). In the specific case studied in this work, the conversion takes place at $R \gtrsim 1$, where the dimensionless radial distance from the pulsar R is defined in Eq. 1.15 and $R = 1$ is the critical radius at which the wind density is no more sufficient to sustain an ideal MHD wave. Hence, for $R \gtrsim 1$ the values of σ ad $\overline{\Gamma}_{\rm s}$ are close to the respective values in the ideal MHD part of the wind (which are quoted above) and $\overline{\lambda}/\overline{r}_{\rm g} \ll 1$. However, this statement is more general. In fact, even if the conversion to superluminal waves occurs spontaneously at $R > 1$ and magnetic reconnection has partially dissipated the Poynting flux accelerating the bulk, the value of the magnetisation changes according to [95] as follows

$$\sigma = \frac{\hat{\mu}}{\overline{\Gamma}_{\rm s}} - 1 \tag{4.36}$$

where $\hat{\mu}$ is the mass-loading factor defined in Eq. 1.14, or in other words, the maximum Lorentz factor attained by the wind if all the spin-down power is converted into the bulk kinetic energy ($\hat{\mu} \sim 10^4 - 10^6$ for the Crab, e.g.,

---

[5]$c = m = \overline{\omega}_{\rm p0} = 1$, implying $e = 1/\sqrt{8\pi}$. See Sect. 2.2 for details.

[71, 86]). Consequently, in the denominator of the right-hand side of Eq. 4.35 we would have

$$\sqrt{\sigma}\,\overline{\Gamma}_{\rm s} = \sqrt{\overline{\Gamma}_{\rm s}\left(\hat{\mu} - \overline{\Gamma}_{\rm s}\right)} \qquad\qquad (4.37)$$

which means that $\overline{\lambda}/\overline{r}_{\rm g} \ll 1$ unless the magnetic reconnection has proceeded almost to completion. At this stage, however, the striped pattern of the pulsar wind would be completely erased and the conversion to superluminal waves would be anyway impossible.

4.6   Limited size of the acceleration region

In all the cases investigated so far, we have always placed the downstream absorbing boundary at a distance $d_{\rm abs} = 500\,\widetilde{L}_{\rm scat}$ from the shock. The absorbing boundary removes from the simulation those particles which have a negligible probability to return to the shock front and cross into the upstream. The reason for this implementation is to limit the computation time.

However, there are realistic situations in which the distance between the shock front and the absorbing boundary might be comparable to (or even smaller than) the scattering length, for example one in which the size of the acceleration region is limited and the scattering agent is not efficient enough to confine energetic particles in the proximity of the shock. Specifically, in the case of PWNe in binary systems, the interaction between the pulsar wind and the stellar wind creates a turbulent region across the contact discontinuity dividing the two flows, where the accelerating particles can be confined. The extension of this region, that we define acceleration region, is small compared to the orbital separation l of the two objects and depends on the pressure balance of the two winds, which is variable over the orbital period. For example, in [25] it was shown that for PSR B1259-63 the size of the acceleration region is $d_{\rm abs} = 0.1 - 0.15\,l$ for a post-termination shock magnetisation $\sigma = 0.003 - 0.1$ and for $\eta = 0.1$. The parameter η is the ratio of the pulsar wind pressure to the stellar wind pressure defined in Eq. 1.23. If the conditions for efficient scattering cease at the border of the acceleration region or the flow is such to drag particles away, the probability of returning to the shock front drops and the spectrum is expected to steepen.

We simulate this situation for a shock Lorentz factor $\overline{\Gamma}_{\rm s}\overline{\beta}_{\rm s} = 10.0$ by fixing the distance of the downstream absorbing boundary from the shock front to $d_{\rm abs} = 1000$, in arbitrary units. We then vary the parameter α downstream, and accordingly the diffusion coefficient $\widetilde{D}_{\theta}$, to obtain different values of the scattering length $\widetilde{L}_{\rm scat}$, and we integrate several thousand trajectories with the usual prescription for each case. The only source of particle deflection both upstream and downstream is magnetic turbulence. In Tab. 4.3, we summarise the investigated sample of scattering

$\widetilde{L}_{\rm scat}/d_{\rm abs}$	s
0.02	4.23 ± 0.01
0.10	4.26 ± 0.02
0.50	4.57 ± 0.01
1.50	5.38 ± 0.04
10.00	8.26 ± 0.04

Table 4.3: Scattering length in units of the size of the acceleration region $d_{\rm abs}$ and resulting spectral index.
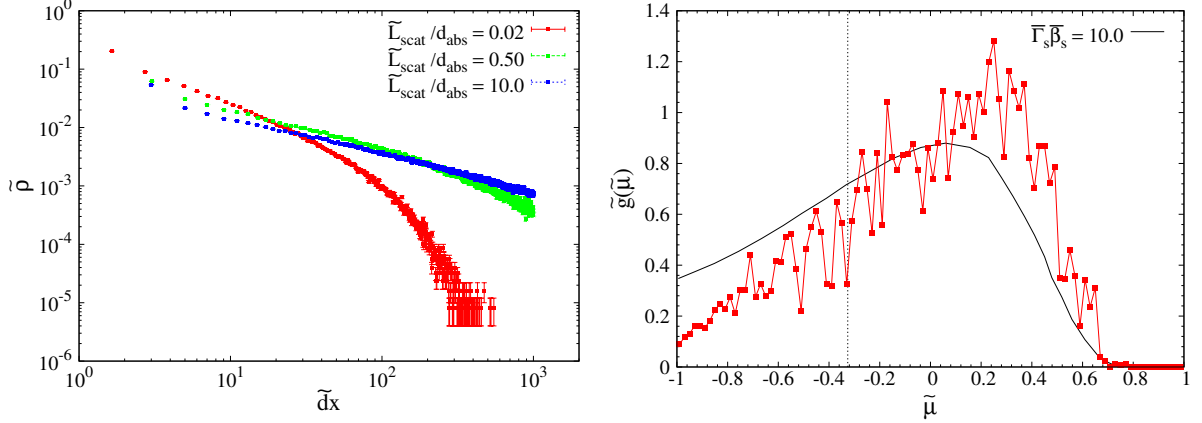
Figure 4.11: Left panel: Downstream particle number density measured as a function of the distance from the shock front $\widetilde{dx}$. The error bars are one standard deviation of a Gaussian distribution in each bin. Right panel: Angular distribution for $\widetilde{L}_{scat}/d_{abs} = 1.5$ (red points and curve) compared with the results of [81] (case of pure scattering and no limitation on the size of the acceleration region, solid black curve).

lengths, expressed in units of the size of the acceleration region d_{abs}, together with the resulting spectral index s. We see that, as long as $\widetilde{L}_{scat} \lesssim 0.02 \, d_{abs}$, we obtain the power-law spectral slope $s = 4.23 \pm 0.01$ that we measured in the previous sections. However, already when $\widetilde{L}_{scat}/d_{abs} \sim 0.1$, the spectrum steepens. The reason for this can be understood from the left panel of Fig. 4.11, where we plot the particle number density downstream of the shock, as a function of the distance $\widetilde{dx}$ from the shock front [6]. When the scattering length is much smaller than d_{abs}, the diffusion properties set by $\widetilde{D}_\theta$ determines the density profile, which drops before reaching $d_{abs} = 1000$. On the contrary, when $\widetilde{L}_{scat}$ increases, the density profile is cut because some particles leave the acceleration region. The effects of this cut on the angular distribution is visible in the right panel of Fig. 4.11 for the case $\widetilde{L}_{scat}/d_{abs} = 1.5$, which we plot for comparison along with the results of [81] (where $\widetilde{L}_{scat} \ll d_{abs}$). Although the red and black distributions are not substantially different, some discrepancies are evident for $\widetilde{\mu} \sim -1$ and $\widetilde{\mu} \sim 0.3$. The reason for the lack of crossing events characterised by $\widetilde{\mu} \sim -1$ is the following. On average, the electrons in the tail of the density distribution generate this kind of events since, in order to have a chance to cross into the upstream, it is more likely that they travel in the anti-parallel direction with respect to the shock front. When the density profile is cut because of particle escape from the acceleration region, the contribution to the angular distribution from this population of particles is missing. On the other hand, the angular distribution of particles crossing from upstream to downstream, on the right-hand side of the vertical black dashed line, does not change significantly. The difference visible in the plot is probably due to a difference in the relative weight between the two parts of the angular distribution.

In this section we point out that, even in absence of radiation losses, there are other physical mechanisms able

---

[6]The error bars in each bin are defined by one standard deviation of a Gaussian distribution of events.

to steepen the spectrum of particles accelerated via the Fermi-like process described in this chapter. We suggest that the scenario of an acceleration region limited in size might be relevant in the context of γ-ray binary systems, where the interaction of the pulsar wind with the stellar wind [25, 51] and the orbital motion [26] strongly affect the post-TS flow. However, a deeper inspection of this scenario is necessary to understand the extent of the modifications both to the angular distribution and to the spectrum.

Chapter 5

Implications for PSR B1259-63

In the previous chapters we have investigated a physical scenario in which the conversion of a pulsar striped-wind into strong superluminal waves leads to the establishment of an electromagnetically modified precursor ahead of the termination shock (TS). In this structure the Poynting flux carried by the pulsar wind is efficiently dissipated into direct kinetic particle energy. The plasma particles are scattered by the turbulent fields on both sides of the TS and a fraction P_{inj} of electrons and positrons is reflected upstream where it forms a population of pre-accelerated particles (Chapt. 3). This population is then accelerated in a full Fermi-like acceleration process (Chapt. 4). In the present chapter we analyse the implications of this scenario in the context of the γ-ray binary system PSR B1259-63.

We have seen in fact that the conversion into superluminal waves can take place only when the plasma density in the wind, which scales as $\propto 1/r^2$ as long as the wind is not accelerated (see Chapt. 1), is no more sufficient to sustain an ideal MHD wave [76, 7]. The condition on the maximum plasma density for which the propagation of superluminal waves is allowed can be expressed either in terms of the proper plasma frequency $\omega > \overline{\omega}_p$ [6], where $\overline{\omega}_p$ is defined in Eq. 1.17, or in terms of a dimensionless radial distance from the pulsar $R > 1$ [7], where R is defined in Eq. 1.15. If the γ-ray binary is formed by a Pulsar Wind Nebula (PWN) and a massive star, the condition for the conversion to superluminal modes can be periodically fulfilled because of the orbital motion. In Sect. 5.1 we briefly revise the paradigm of a PWN orbiting a Be star and in Sect. 5.2 we present the system PSR B1259-63/SS 2883 and the features of its high energy emission. In particular, we describe the episode known as the GeV flare (e.g., [1, 131]). This is a sudden enhancement of the emission in the $0.1 - 1$ GeV band occurring about thirty days after periastron passage which has been observed for two consecutive orbits. In Sect. 5.3, we use the duration of the GeV flare (~ 60 days) to construct a geometrical model to constrain the inclination ζ of the magnetic-axis with respect to the spin-axis. In Sect. 5.4 we employ the value of ζ and our assumption that the flare is triggered by the propagation of superluminal waves to estimate the density in the pulsar wind at the time of the flare. This value is then compared with the estimate of the pulsar wind density obtained with pair production model in the magnetosphere. Eventually, in Sect. 5.5, we check the consistency of our model verifying that the electrons energised in the electromagnetically modified preshock are able to produce the observed GeV flare upscattering disk and stellar photons.

5.1 Superluminal waves in γ-ray binaries

As already mentioned (Sect. 1.4), one of the possible scenarios proposed to explain sources known as γ-ray binaries involves a luminous pulsar powering a PWN in orbit around a massive main sequence star, normally associated with a Be star. This picture is illustrated in Fig. 5.1. Nowadays, five binaries are categorised as γ-ray binaries (see Sect. 1.4; for a complete review see [49]), although PSR B1259-63 is the only system for which the radio pulsations have been observed [65, 66]. Be stars are characterised by strong outflows modelled as two-component winds with a fast and low-density component from the polar region and a slow and high-density component from the equatorial region forming a disk-like flow [139, 87, 133]. The presence of the massive companion wind, absorbing and scattering the pulsed radio emission from the NS, is probably the cause of the non-observation of the pulsar in the remaining four γ-ray binaries and of the deficit of pulsar-massive star binaries [96, 65].

In the polar wind, the mass loss rate is $\dot{M} \sim 10^{-8} M_\odot \, yr^{-1}$ ($M_\odot$ is the solar mass) and the velocity profile of the radiatively driven wind is

$$v_{w,p}(r) = v_\infty \left(1 - \frac{r_\star}{r} \right) \tag{5.1}$$

where $v_\infty \sim 10^8 cm \, s^{-1}$ is the asymptotic value of the polar wind velocity and $r_\star \sim 10 \, r_\odot$ is the stellar radius [139, 132] ($r_\odot$ is the solar radius). On the other hand, the equatorial wind has a larger mass loss rate $\dot{M} \sim 10^{-7} M_\odot \, yr^{-1}$ and the velocity and density profiles are

$$v_{w,e}(r) = v_0 \left(\frac{r}{r_\star} \right)^{m-2}, \qquad \rho_{w,e}(r) = \rho_0 \left(\frac{r}{r_\star} \right)^{-m} \tag{5.2}$$

where $v_0 \sim 10^6 cm \, s^{-1}$ and $\rho_0 = \dot{M}/4\pi r_\star^2 v_0 \sim 10^{-10} - 10^{-13} g \, cm^{-3}$ are the velocity and density at the stellar surface, respectively, and $2 \leq m \leq 4$ depending on the star [138, 87, 132]. During the orbital motion, the pulsar wind can interact with different parts of the stellar wind, according to the inclination of the massive companion spin-axis with respect to the orbital plane, and whichever dominates depends on the parameters of the two winds. The
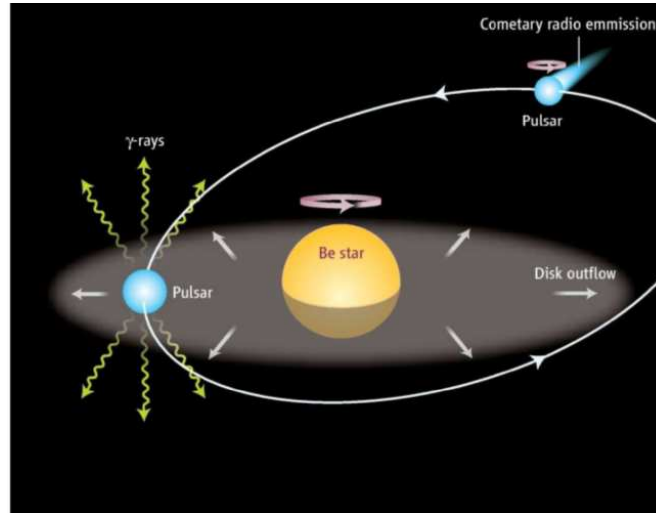

Figure 5.1: Sketch of a γ-ray binary system. Credits: adapted from Mirabel 2006 [106]

interaction is usually supersonic for both media, resulting in a double shock structure with the shocked material from each region separated by a contact discontinuity [48]. The shock of the pulsar wind is located on the line connecting the two stars where the pressure of the outflows balances. This is expressed via the dimensionless ratio of momentum fluxes η defined in Eq. 1.23 which determines which is the dominant wind. The distance of the TS from the pulsar as a function of the orbital separation l is then computed with [48]

$$\frac{r_{\text{TS}}}{l} = \frac{\eta^{1/2}}{\eta^{1/2} + 1} \, . \tag{5.3}$$

Even when η is constant and the Be star wind is isotropic, the distance from the pulsar to the TS changes along the orbit, remaining however much smaller than the distance to the TS in an isolated PWN. For PSR B1259-63, for example, the orbital distance changes by a factor larger than 14 between periastron and apastron (e.g., [132]), and assuming that the TS is halfway between the stars, this means that $r_{\text{TS}} < 7 \times 10^{13} cm$, which is at least four orders of magnitude smaller than r_{TS} of the Crab. We stress that in the context of binary systems, we use r_{TS} to define the distance of the TS from the pulsar at the apex of the bow-like nebula, while on the opposite side the nebula can be more extended.

The periodic variation of r_{TS} affects the density in the pulsar wind, which is larger (smaller) in the proximity of periastron (apastron). Thus, somewhere along the orbit, the pulsar wind density can be low enough for the conditions for the launch of superluminal waves to be fulfilled. This leads to the formation of the shock precursor and to efficient injection and acceleration of plasma particles. The strong equatorial wind from the massive companion modifies this simple picture since the pulsar wind is more compact (and then denser) when it interacts with this part of the stellar outflow.

It is worth mentioning that the compactness of γ-ray binaries allows us to study PWNe in a completely different regime with respect to isolated PWNe. In fact, the pulsar wind is terminated much closer to the pulsar in a binary system, before a substantial fraction of Poynting flux is dissipated. As a consequence, the values of the wind magnetisation and Lorentz factor at the TS are expected to be similar to those at the sonic point.

5.2 PSR B1259-63/SS 2883 γ-ray binary system

Among the γ-ray binaries, the system PSR B1259-63/SS 2883 is the only one where the compact object is observed to be a pulsar [65, 66]. The spin-period is $P = 47.7 \, ms$, corresponding to a pulsar frequency $\omega \sim 131 \, Hz$, and its derivative is $\dot{P} \sim 10^{-15}$. These values entail a spin-down luminosity $L_{\text{SD}} \sim 8 \times 10^{35} erg \, s^{-1}$ (computed with Eq. 1.1) and a NS surface magnetic field $B_{\text{NS}} = 3.2 \times 10^{19} (P\dot{P})^{1/2} \, G \sim 3 \times 10^{11} G$ [66, 64, 55]. The pulsar orbit is highly eccentric ($e = 0.87$) and a complete revolution lasts $\sim 1237 \, d$. The companion SS 2883 is a massive Be star of mass $M_\star \sim 21 - 26 \, M_\odot$ and radius $r_\star \sim 9 \, r_\odot$. Its luminosity is $L_\star \sim 6.2 \times 10^4 L_\odot$ ($L_\odot$ is the luminosity of the Sun) and the average surface temperature is $T_\star \sim 2.7 \times 10^4 K$ [75, 108]. The distance to the binary system is $D = 2.3 \pm 0.2 \, kpc$ and the inclination of the orbital plane to the plane of the sky is $i \sim 19° - 31°$ [108, 49]. The semi-major axis of the orbit is estimated to be $a = 7 \, AU = 1.05 \times 10^{14} cm$ [108], which means that the orbital distance at periastron is $l_{\text{p}} = 1.4 \times 10^{13} \, cm$, while at apastron the orbital separation is $l_{\text{a}} = 2.0 \times 10^{14} \, cm$.

In this system, the evidence for a disk-like stellar outflow is compelling. The radio pulsed emission is obscured between $t_{\text{o},1} \sim \tau - 18 \, d$ and $t_{\text{o},2} \sim \tau + 16 \, d$, where τ is the time of periastron passage (e.g., [64, 35]). In terms of the true anomaly, namely the angle between the semi-major axis and the line connecting the two stars, this corresponds to obscuration between $f_{\text{o},1} \sim 271°$ and $f_{\text{o},2} \sim 84°$, where $f_\tau = 0°$ is the true anomaly of periastron.

The eclipse is associated to the passage of the pulsar through and behind the putative disk, as observed from Earth. This picture is strengthened by the analysis of the unpulsed radio, X-ray and TeV light-curves [65, 64, 4, 5, 1, 36] which show two peaks in correspondence of the passages through the disk and a minimum in correspondence of the periastron passage, differently from the scenario proposed by [77], where the emission peak should coincide with the periastron passage. The enhancement of the emission upon disk crossing is probably due to the variation of pulsar wind parameters such as magnetisation σ or Lorentz factor Γ [130, 91]. Alternatively, it can be due to a change in the geometry of the acceleration region when the pulsar wind and the equatorial disk of the star collide [34, 35, 36]. This leads to more efficient Synchrotron and Inverse Compton emission. The rise and decay profiles of X-ray and TeV emissions are used to constrain the inclination of the intersection line between the equatorial disk and the orbital plane with respect to the major axis of the system to $\sim 20°$ [35]. The putative equatorial disk seems to be highly inclined with respect to the pulsar orbital plane ($\theta_{disk} \sim 70°$ [35, 91]) so that, except for the two disk crossings per orbit, PSR B1259-63 is supposed to interact mainly with the polar component of the stellar outflow.

As for isolated PWNe, the dominant emission mechanisms are Synchrotron radiation in the nebular magnetic field and Inverse Compton scattering off energetic electrons and positrons accelerated at the wind TS [132]. In binary systems, the target photon fields for the latter process are supplied by the companion star [77, 13] and by the circumstellar disk [74].

5.2.1   GeV flare

The most interesting feature of the binary system PSR B1259-63/SS 2883 is a flare in the GeV band occurring at $t_{flare} \sim \tau + 30 \, d$ (corresponding to the true anomaly $f_{flare} = 111°$) and lasting $\Delta t_{flare} \sim 60 \, d$ (corresponding to $\Delta f_{flare} \sim 30°$), which constitutes a challenge to present theoretical models. The flare has been observed during two consecutive orbits in 2011 [1] and 2014 [131], showing remarkable similarities between the two episodes [31]. This emission forms a new and spectrally distinct component in the band $0.1 - 1$ GeV, while no significant emission is detected above 1 GeV and in any other band. The spectrum is well described by a single power-law which is softer when the source is brighter. At the beginning of the flare, the source flux increases by a factor of ~ 10 with respect to the level of first disk passage, reaching a maximum flux above 100 MeV $F_\gamma \sim 3 \times 10^{-6} cm^{-2} \, s^{-1}$ in 2011 [1] and $F_\gamma \sim 2 \times 10^{-6} cm^{-2} \, s^{-1}$ in 2014 [131]. If the emission of the flare were isotropic, the γ-ray luminosity would almost equal the estimated pulsar spin-down luminosity, meaning that the efficiency of conversion of the NS rotational energy in GeV radiation is close to 100%. Many possible scenarios have been proposed to explain this periodic GeV flare. One possibility is based on Inverse Compton scattering off electrons in the unshocked pulsar wind [73, 74]. This requires a large value of the wind Lorentz factor $\Gamma \geq 10^4$, a dense target photon field originating in the equatorial disk and a favourable geometry, in which the region of the unshocked pulsar wind extending towards the observer is wide enough to produce the observed emission. Another viable scenario assumes that the region downstream of the TS is illuminated by X-ray photons produced in the extended PWN [50]. At this location, a relativistic Maxwellian distribution of electrons and positrons at energy $\Gamma m_e c^2$ generated at the termination shock of the pulsar wind [125] upscatters the X-ray photons giving rise to the GeV flare. Eventually, it has been suggested that the GeV flare originates in the tail of the bow-shock structure, where the flow is re-accelerated from $\Gamma \sim 1$ at the shock apex to $\Gamma \lesssim 5$ in the tail [25, 51]. The re-acceleration of the bulk cannot proceed further because, far from the shock apex, the orbital motion and the Coriolis force wrap the flow in a spiral-like shape [26]. The Synchrotron radiation produced in the accelerated region is thus Lorentz-boosted in the direction of Earth and observed as the

flare [74].

In this work, we argue that the GeV flare is produced via Inverse Compton scattering of stellar or disk photons off electrons and positrons efficiently energised at the TS after the onset of the electromagnetic precursor due to the conversion of the pulsar striped-wind into strong superluminal waves (see Chapt. 2). As already explained, superluminal waves can only propagate in tenuous plasma so that the conversion is more likely to happen when the pulsar is far from the companion rather than at periastron. This is consistent with a flare starting about one month after the periastron passage (see Sect. 5.4 in the following).

5.3 Inclination of the magnetic dipole moment

Although emission at high latitudes in the pulsar wind has been invoked to explain the GeV flare [50], the very large conversion efficiency of pulsar spin-down luminosity into the luminosity of the flare [1] suggests that the emission of this periodic episode originates in the equatorial region of the PWN, where most of the energy is deposited when the oscillating magnetic field annihilates. Recent results of 2-dimensional [110] and 3-dimensional [116] relativistic MHD simulations also support the view that efficient particle acceleration and radiation emission takes place in the equatorial region of the TS.

In a PWN, the equatorial region is defined as the range of latitudes where the wind is striped, *i.e.*, where stripes of magnetic field of opposite polarity are separated by a current sheet embedded in the flow. Thus, the wind equatorial belt extends at colatitudes $90° - \zeta < \theta < 90° + \zeta$, where θ is the polar angle computed from the pulsar spin-axis and ζ is the angle between this axis and the magnetic dipole moment. At colatitudes $\theta < 90° - \zeta$ and $\theta > 90° + \zeta$ the magnetic field does not change sign and the wind is not striped. It is clear that for a small inclination ζ, the wind equatorial region is not very extended, whereas for $\zeta = 90°$ the striped-wind occupies the entire sky.

It has been suggested that the value of the inclination of the magnetic dipole moment to the spin-axis for PSR B1259-63 is $\zeta \sim 90°$, because of the observation of a strong radio inter-pulse interpreted as the emission from the opposite magnetic pole after half a rotation of the pulsar [113]. However, this scenario is disfavoured by [65], where this feature is interpreted as a second pulse from a single magnetic pole rather than radiation from two poles. Here, we estimate the inclination of the magnetic dipole to the spin-axis assuming that the GeV flare is produced only by the interaction of the stellar wind with the equatorial region of the pulsar wind, and not with the flow at higher latitudes. This assumption is justified by two considerations. Firstly, the luminosity of the pulsar wind is proportional to $\sin^2 \theta$ [103, 23], so that most of the power is concentrated in the wind equatorial plane. Secondly, the energy available for plasma particles at the TS is not associated to the total upstream Poynting flux, but it is only associated to the Poynting flux of the alternating component of the magnetic field [95]. At colatitude $\theta = 90°$, the stripes of opposite polarity have the same width and the average magnetic field vanishes. Consequently, when the stripes annihilate, their entire energy is transferred to the plasma particles. On the other hand, at lower (or higher) colatitudes, the stripes of opposite polarity have different width and when they annihilate at the TS a fraction of the magnetic field (equal to the average magnetic field in one wavelength λ) survives. Thus, the Poynting flux carried by this component of the field is not dissipated and the energy available for particles is lower. Hence, it is conceivable that where the wind is not striped the dissipation of the wind magnetisation at the TS is negligible.

Under this assumption, we consider the equatorial region of the PWN to be a cylinder of radius r_{TS} and thickness Δ, where the inclination of the magnetic moment to the pulsar spin-axis is found as
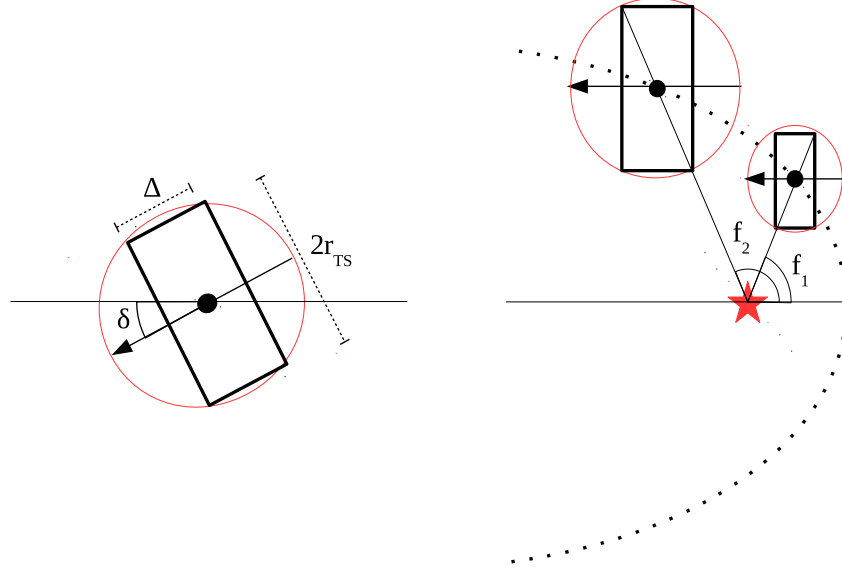
Figure 5.2: Illustration of the geometrical model projected onto the orbital plane. Left panel: pulsar wind equatorial region (solid back rectangle) and PWN (solid red circle) for $\varphi = 0°$ and generic value of δ; Right panel: the initial and final true anomalies of the interaction of the stellar wind with the equatorial region of the pulsar wind, represented for $\varphi = 0°$ and $\delta = 0°$.

$$\zeta = \tan^{-1}\left(\frac{\Delta}{2r_{TS}}\right). \tag{5.4}$$

Although the pulsar wind is probably forced into a cometary shape by the wind of the massive companion, for our purpose a spherically symmetric wind is thought to be a good approximation [132]. We build a geometrical scheme where the GeV flare is produced by the interaction between the wind of SS 2883 and the equatorial belt of the pulsar wind, namely only when the line connecting the two stars crosses the entire cylinder, without first crossing regions of higher latitudes. This is illustrated in Fig. 5.2 with a face-on representation of the orbital plane. The black rectangle and arrow are the projections of the wind equatorial region and pulsar spin-axis onto the orbital plane, respectively, while the red circle is the spherically symmetric PWN. The picture involves the following angles: φ is the angle between the pulsar spin-axis and the orbital plane; δ is the angle between the projection of the pulsar spin-axis onto the orbital plane and the semi-major axis (*i.e.*, the true anomaly of the pulsar spin-axis as shown in the left panel of Fig. 5.2). In the right panel of Fig. 5.2 we show that, if the flare were produced only by the geometrical interaction, the enhanced GeV emission would be observed for a range of true anomaly going from f_1 to f_2 for $\delta = 0°$ and $\varphi = 0°$, where $f_\tau = 0°$ is the true anomaly of periastron[1]. Instead, for $f < f_1$ and $f > f_2$, the stellar wind would interact with high latitude regions of the pulsar wind where most of the energy is carried by the average magnetic field and not by the particles. As can be seen in the picture, the

---

[1] If $\varphi = 90°$, the pulsar equatorial region lies in the orbital plane and the line connecting the two stars always crosses the entire cylinder.

beginning and the end of such a flare would correspond to

$$f_1 = \tan^{-1}\left(\frac{2r_{TS,1}}{\Delta_1}\right) \tag{5.5}$$

$$f_2 = \tan^{-1}\left(\frac{\Delta_2}{2r_{TS,2}}\right) + 90° \tag{5.6}$$

where we use the indexes 1 and 2 to account for a change of the dimension of the PWN as the orbital distance increases. In fact, the distance between the stars, and accordingly r_{TS}, changes by a factor of ~ 2 between the beginning and the end of the flare. Here, we consider η to be constant over the orbit. In case the true anomaly of the projection of the pulsar spin-axis is $\delta \neq 0°$, both the beginning and the end of the flare are delayed, in terms of true anomaly f, by the angle δ. Eventually, for $\varphi \neq 0°$, *i.e.*, for the pulsar spin-axis not lying in the orbital plane, the pulsar wind equatorial region has an effective width on the orbital plane given by $\Delta/\cos\varphi$. Thus, the general form of Eqs. 5.5 and 5.6 is

$$f_1 = \tan^{-1}\left(\frac{2\cos\varphi\, r_{TS,1}}{\Delta_1}\right) + \delta \tag{5.7}$$

$$f_2 = \tan^{-1}\left(\frac{\Delta_2}{2\cos\varphi\, r_{TS,2}}\right) + 90° + \delta \tag{5.8}$$

giving the initial and final values of the true anomaly corresponding to a flare produced by the geometric interaction of the stellar wind with the equatorial region of the PWN. A twin flare would also be expected in this case between $f_1' = f_1 + 180°$ and $f_2' = f_2 + 180°$.

However, in the scenario we have built in this work, the flare is not only due to geometrical reasons. The onset of the flare can be explained by efficient electron acceleration triggered by the formation of the shock precursor when the density in the pulsar wind is low enough to allow the propagation of superluminal waves. We assume this happens at $f_{flare} = 111° \neq f_1$, that is the true anomaly corresponding to the first observation of the enhanced GeV emission [1, 131]. The time evolution of the GeV emission is then dictated by geometrical conditions, in particular the drop of the flux of target photons with increasing orbital distance (scaling as $\propto l^{-2}$) and the less favourable inclination of the line connecting the stars with respect to the equatorial region of the pulsar wind. Associating the last observation of GeV emission at $t \sim \tau + 90\,d$ ($f_{end} \sim 141°$) to f_2 in the situation depicted in Fig. 5.2, we use Eq. 5.8 to constrain the ratio $\Delta_2/r_{TS,2}$ and thus the inclination of the magnetic moment to the pulsar spin-axis. We perform this calculation for $\delta = 20°$ and $\varphi = 46°$ [109, 74] and from Eq. 5.4 we find $\zeta \sim 23°$. Interestingly, for $\delta = 20°$ and $\varphi = 46°$ the pulsar spin-axis and the line connecting the two stars are almost perpendicular at the time of the beginning of the flare [74]. For this inclination, the geometrical collision of the winds is extremely favourable.

Given that ζ is constant, the ratio $\Delta/2r_{TS}$ is also constant over the orbit. Thus, from Eq. 5.7 we can compute $f_1 \sim 78°$, which is the true anomaly at the beginning of a geometrically induced flare. Since f_1 is smaller than the true anomaly corresponding to the end of the eclipse due to the disk ($f_{o,2} \sim 84°$), the pulsar is embedded in the equatorial stellar wind at this stage. Consequently, the plasma density in the pulsar wind is likely to be large. This prevents the propagation of superluminal waves and the formation of the shock precursor which triggers electron acceleration and the emission of the flare. An analogous argument holds true for a putative twin geometrical flare. The twin flare would occur between $f_1' \sim 258°$ and $f_2' \sim 321°$, while the passage of the pulsar through and behind the circumstellar disk starts at $f_{o,1} \sim 271°$. Thus, in this range of true anomaly the density in the pulsar wind is too large for the superluminal waves to propagate. We will comment more on this point in Sect. 5.5.

The simple geometrical model presented in this section has limitations which are mainly due to two aspects: (1) the shape of the termination shock; (2) the shape of the critical surface beyond which superluminal waves are allowed. As for point (1), we have mentioned in Sect. 1.1.3 that the surface of the TS is not disk-like, but rather oblate. Assuming that the ram pressure downstream of the TS is roughly constant, the expression for the oblate surface of the TS computed by [94, 7] is

$$\left(\frac{dr_{\text{TS}}}{d\theta}\right)^2 + r_{\text{TS}} = r_0 \sin^2 \theta \tag{5.9}$$

where r_0 is a constant depending on the external pressure and must be evaluated for the specific object under consideration. However, 3-dimensional relativistic MHD simulations by [116] suggest that the oblate deviation from a disk-like shape of the TS might not be substantial and also these authors fit the section of the equatorial region of the pulsar wind with a rectangle, as we did in this work. It is worth mentioning that the results of [116] are obtained assuming that the Poynting flux in the striped region of the wind is completely dissipated on the way from the pulsar to the TS. Although this might not be the case and most of the dissipation occurs instead at the TS itself as envisaged in the driven magnetic reconnection picture and in the scenario involving superluminal waves considered here, according to [95] this makes no difference since the plasma magnetisation and dynamics only depend on the average magnetic field in the stripes. As for point (2), in [7] it is found that the shape of the critical surface strongly depends on the angle ζ and on the ratio of $r_{\text{TS,eq}}$ to the size of the critical surface $r_{\text{cr,eq}}$, both computed at $\theta = 90°$ (in the pulsar equatorial plane). For a perpendicular rotator ($\zeta = 90°$) the shape of the critical surface is similar to the shape of the TS, *i.e.*, oblate. For an oblique rotator ($\zeta < 90°$), instead, the critical surface follows the oblate profile only in the colatitude range $90° - \zeta \leq \theta \leq 90° + \zeta$ (in the equatorial region). Outside this range (in the polar region) its shape is cone-like, in the sense that r_{cr} diverges. Thus, for $r_{\text{TS,eq}}/r_{\text{cr,eq}} \gtrsim$ a few, almost the whole critical surface falls within the TS shock radius, so that superluminal waves are allowed almost everywhere except for the regions $\theta < 90° - \zeta$ and $\theta > 90° + \zeta$, where $r_{\text{cr}} > r_{\text{TS}}$.

Although a detailed analysis of the shape of the TS and of the critical surface is probably necessary for the specific case of PSR B1259-63, the previous considerations suggest that our assumption of a disk-like equatorial region of the pulsar wind is reasonable and that our estimate $\zeta \sim 23°$ is not too rough.

5.4 Constraints from the superluminal wave scenario

The assumption that the GeV flare in PSR B1259-63 is triggered by the conversion of the MHD striped-wind into superluminal waves places some constraints on the physical parameters of the PWN, in particular on the density of the wind at the TS. To compute these constraints, we employ the conditions $\omega > \overline{\omega}_{\text{p}}$ and $R > 1$ for the propagation of superluminal waves and the jump conditions between the subluminal and superluminal waves carrying the same energy, momentum and particle fluxes (Eqs. 1.20-1.22). We recall that in Eq. 1.19 and in Eq. 1.22 the quantities $\overline{n}^{\text{u}}$ and $\overline{n}^{\text{d}}$ are the wind proper densities respectively upstream and downstream of the critical surface at distance R from the pulsar at which the conversion takes place. The value of the proper density downstream of R can be estimated inverting Eq. 1.16 and using the definition of the proper plasma frequency in Eq. 1.17. This yields

$$\overline{n}^d = \frac{m}{4\pi e^2}\left(\frac{\omega}{\Gamma_>}\right)^2 \tag{5.10}$$

from which we can compute the value of the density $n^u = \Gamma \overline{n}^u$ upstream of R, as expressed in the lab. frame. Using the definition of the particle flux density J upstream of R given in Eq. 1.19, the related jump condition Eq. 1.22 and the value of the parallel momentum $p_\parallel$ defined in Sect. 1.2, we obtain

$$n^u = \overline{n}\,^d \frac{\hat{\mu}}{\beta} \frac{\Gamma_>^2}{R^2} = \frac{m}{4\pi e^2} \frac{\hat{\mu}}{\beta} \left(\frac{\omega}{R}\right)^2. \tag{5.11}$$

Now, given that the pulsar wind is supposed to be highly relativistic ($\beta \sim 1$) and that the value of the conversion radius also fixes the mass-loading factor $\hat{\mu}$ (see Eq. 1.15), the pulsar wind density only depends on the pulsar frequency and on the location where the striped-wind converts into superluminal waves. At this stage, we make use of a basic assumption, also used in Chapt. 2, namely that the conversion to superluminal mode does not proceed spontaneously, but it is triggered by the interaction of the striped-wind with the TS. This implies that Eq. 1.15 becomes

$$R = \frac{\hat{\mu}}{a_L} \frac{r_{TS}}{r_{LC}} \tag{5.12}$$

where $r_{LC} = c/\omega$ is the light cylinder radius. The strength parameter a_L defined in Eq. 1.13 can be written for PSR B1259-63 as

$$a_L \sim 3 \times 10^9 (\Omega_s/4\pi)^{-1/2} \tag{5.13}$$

where Ω_s is the portion of sky occupied by the striped section of the pulsar wind. Since the orbital parameters of PSR B1259-63 are observationally well constrained, we know how the distance l between the two stars varies along the orbit and for reasonable values of the parameter η we can readily compute r_{TS} via Eq. 5.3 and thus obtain an estimate of the density at the TS n^u for different values of R.

To check the consistency of this estimate, we can use this value of n^u to compute the wind density at the light cylinder using a r^{-2} profile, and comparing it with the density obtained with a magnetospheric pair production model. The chosen density profile to connect n^u to n_{LC} is justified only if two conditions are met: (1) the sonic point where $\Gamma_{fms} = \sqrt{\sigma_{fms}}$ is close to the light cylinder and (2) the dissipation of the Poynting flux between the sonic point and the TS is negligible. In fact, the density of a radial and relativistic flow expanding at constant speed scales as r^{-2}, while from the theory of the pulsar wind we know that the wind accelerates from the light cylinder to the sonic point and when the magnetisation of the flow is dissipated into kinetic energy of the bulk (see Chapt. 1). While condition (2) is likely to be met in a γ-ray binary since the TS is relatively close to the pulsar and dissipation cannot work effectively on such a short length-scale[2], condition (1) is probably more demanding. In fact, although pairs are supposed to be produced in the magnetosphere with a Lorentz factor $\gamma > 20$ [23] and the flow at the wind launching point is assumed to be relativistic, it is not clear what is the bulk Lorentz factor at the light cylinder and where is located the sonic point. We will comment more on this condition in the following.

According to pair production models in the pulsar magnetosphere, the density of particles at the light cylinder is (e.g., [93, 113])

$$n_{LC} \approx \kappa \frac{\omega B_{LC}}{2\pi ec} = \kappa \frac{\omega B_{NS}}{2\pi ec} \frac{R_{NS}^3}{R_{LC}^3} \sim 3.6 \times 10^4 \kappa\, cm^{-3} \tag{5.14}$$

where we have assumed that the dominant contribution to the magnetic field comes from the dipole moment. Here, we implicitly use the definition of the Goldreich-Julian pair production rate in the polar caps defined in Eq. 1.4 stemming from the definition of the Goldreich-Julian particle density given in Eq. 1.2. The value of the

---

[2]Only a very efficient dissipation is able to convert the entire wind magnetisation into bulk kinetic energy within the TS for the Crab [93, 86], where $r_{TS,Crab} \sim 10^4 r_{TS,B1259}$.

multiplicity κ (*i.e.*, the number of secondary particles generated during a cascade) is rather uncertain, but in general it is expected to be as large as $\kappa \sim 10^1 - 10^5$ [8, 62, 63, 135]. For the specific case of PSR B1259-63, magnetic reconnection models set $\kappa \lesssim 8 \times 10^4$ [114] which implies a density at the light cylinder $n_{\mathrm{LC}} \sim 1.6 \times 10^9 cm^{-3}$, whereas for $\kappa \sim 3 \times 10^5$ [113] the density is $n_{\mathrm{LC}} \sim 7 \times 10^9 cm^{-3}$. These last two values of the multiplicity are in good agreement with the most recent semi-analytical model of cascade pair production in the polar caps of pulsar magnetospheres [135].

The value of the multiplicity is related to the mass-loading factor via (e.g., [93, 84])

$$\kappa = \frac{a_{\mathrm{L}}}{4\hat{\mu}} \tag{5.15}$$

which means that in our scenario an estimate of R, and consequently of $\hat{\mu}$, also provides the value of the pair multiplicity.

Hence, we proceed as follows. We compute the value of the parameter a_{L} with Eq. 5.13 for two possible inclinations of the magnetic dipole moment with respect to the pulsar spin-axis, namely $\zeta = 90°$ suggested by [113] and $\zeta = 23°$ found in Sect. 5.3. The former gives $\Omega_{\mathrm{s}}/4\pi = 1$ while the latter provides $\Omega_{\mathrm{s}}/4\pi = 0.39$. We obtain r_{TS} from Eq. 5.3 using the value of the orbital distance at the time of the beginning of the flare $l \sim 0.35\,a \sim 3.7 \times 10^{13} cm$, where a is the semi-major axis of the binary system. We use $\eta = 0.1$ [74, 25, 51] which entails $\dot{M} \sim 10^{-8} M_\odot\,yr^{-1}$ and $v_{\mathrm{w}} \sim 10^8 cm\,s^{-1}$, consistent with typical values of the polar wind in Be stars [139]. We then use $r_{\mathrm{TS}} \sim 4 \times 10^4\,r_{\mathrm{LC}}$ to compute the mass-loading factor for a specific value of the conversion radius R with Eq. 5.12 and we plug the values of $\hat{\mu}$ and R in Eq. 5.11 to obtain the lab. frame density of the pulsar striped-wind at the TS. This value is then scaled to the light cylinder via

$$\hat{n}_{\mathrm{LC}} = n^u \Big(\frac{r_{\mathrm{TS}}}{r_{\mathrm{LC}}}\Big)^2 \tag{5.16}$$

to estimate the wind density at this location. We collect the results of this procedure in Tab. 5.1. The value of $\hat{n}_{\mathrm{LC}}$ for each case must be compared to the value of the same quantity given by Eq. 5.14, where we use $\kappa = 5 \times 10^4$ which is appropriate for a pulsar with surface magnetic field $B_{\mathrm{NS}} \sim 3 \times 10^{11}\,G$ (dominant dipole configuration) and period $P_{\mathrm{Crab}} \sim 33\,ms$ [135] (the value of κ found by [135] shows only a weak dependence on the pulsar period, thus the uncertainty introduced using P_{Crab} instead of $P \sim 47.7\,ms$ is small). Equation 5.14 yields $n_{\mathrm{LC}} \sim 1.8 \times 10^9 cm^{-3}$. From the results in Tab. 5.1 we see that, when the conversion radius is large ($R = 10$), the conditions for the propagation of superluminal waves provide a value of the multiplicity κ which is more than one order of magni-

η	ζ	R	$\hat{\mu}$	κ	$\hat{n}_{\mathrm{LC}}\,[cm^{-3}]$
0.1	90°	1	7.8×10^4	9.7×10^3	6.3×10^8
0.1	90°	10	7.8×10^5	9.7×10^2	6.3×10^7
0.1	23°	1	1.2×10^5	9.7×10^3	1.0×10^9
0.1	23°	10	1.2×10^6	9.7×10^2	1.0×10^8
1.0	23°	1	6.0×10^4	2.0×10^4	2.1×10^9

Table 5.1: Estimates of the mass-loading factor $\hat{\mu}$, multiplicity κ and wind density at the light cylinder computed from the condition for superluminal wave propagation for different values of the inclination of the magnetic moment to the pulsar spin-axis ζ and conversion radius R. The grey row highlights our benchmark result.

tude smaller than that computed with magnetospheric pair production models. For these cases, our estimate of the plasma density at the light cylinder is $\hat{n}_{LC} \ll n_{LC}$. On the other hand, for $R = 1$ our estimate of κ is only a factor of ~ 5 smaller than the multiplicity computed by [135], showing a much better agreement with the most recent polar caps pair production model and with previous estimates for PSR B1259-63 [113]. The resulting range of mass-loading factor $\hat{\mu} \sim 7.8 \times 10^4 - 1.2 \times 10^5$ is consistent with the values published in the literature for this object ($\hat{\mu} \sim 6 \times 10^4$ [107], $\hat{\mu} \sim 4 \times 10^5$ [136] and $\hat{\mu} \sim 10^6$ [77]). For $R = 1$, the value of the plasma density at the light cylinder $\hat{n}_{LC}$ computed with our procedure is in remarkable agreement with the result of Eq. 5.14, being at most a factor of ~ 3 smaller than n_{LC}. The results are only slightly affected by the inclination ζ of the magnetic dipole moment with respect to the pulsar spin-axis. According to the results collected in Tab. 5.1, to our findings in Chapt. 2 concerning the establishment of a stable precursor and to our calculation of ζ in Sect. 5.3, we select the results obtained for $R = 1$ and $\zeta = 23°$ as benchmark (the corresponding row is highlighted in grey in Tab. 5.1).

In the last row of Tab. 5.1 we show the results of our procedure using the parameter $\eta = 1$, which implies that the TS is halfway between the two stars. Also in this case, the resulting values of $\hat{\mu}$ and κ are consistent with the most recent estimates published in the literature (κ is only a factor of ~ 2.5 smaller than the multiplicity computed by [135]) and the value of $\hat{n}_{LC}$ is even in better agreement with $n_{LC} \sim 1.8 \times 10^9 cm^{-3}$. This means that our calculation depends, though not substantially, on the value of the not very well constrained parameter η and suggests that the standing shock separating the pulsar and stellar winds might be further away from the pulsar than normally supposed.

The reason for the difference between the values of $\hat{n}_{LC}$ and n_{LC} might be that the r^{-2} density profile is not appropriate to connect the density at the TS all the way back to the light cylinder. This would be the case if assumption (1) is not valid and the wind is substantially accelerated between the light cylinder and the sonic point, where the mass-loading factor, which is a constant of the flow, can be expressed as $\hat{\mu} = \Gamma_{fms}(1 + \sigma_{fms}) \propto \sigma_{fms}^{3/2}$ [82]. However, if assumption (2) holds true, the values of the wind magnetisation and Lorentz factor at the TS factor must be similar to those at the sonic point $\sigma_{TS} \sim \sigma_{fms} \sim \hat{\mu}^{2/3}$ and $\Gamma_{TS} \sim \Gamma_{fms} \sim \hat{\mu}^{1/3}$. For the largest value of $\hat{\mu}$ in Tab. 5.1, this implies $\sigma_{fms} \sim 1.1 \times 10^4$ and $\Gamma_{fms} \sim 106$. In the Force Free Electrodynamics (FFE) regime, the bulk Lorentz factor grows linearly with the radial distance for $r \gg r_{LC}$ [29, 40], as expressed by

$$\Gamma = \left[\Gamma_{LC}^2 + \left(\frac{r}{r_{LC}}\right)^2\right]^{1/2}. \tag{5.17}$$

If a similar profile also holds for $r \gtrsim r_{LC}$, the requirement that the bulk Lorentz factor at the light cylinder is relativistic sets an upper limit on the distance between the sonic point and the light cylinder to $r_{fms}/r_{LC} \lesssim \Gamma_{fms} \sim 100$. As a consequence, assumption (1) is reasonable for the values of $\hat{\mu}$ (and consequently of Γ_{fms}) in Tab. 5.1, even though possibly not perfectly verified.

Even if assumption (1) is not valid, the selected density profile and the results in Tab. 5.1 are still consistent. In fact, in a radial and relativistic wind $nvr^2 =$ constant, where v is the bulk speed which does not change substantially for an increasing Γ as long as the flow is already relativistic at the launching point. This means that also between the light cylinder and the sonic point the relation $n \propto r^{-2}$ (or very similar) holds true and that the r^{-2} density profile is appropriate to connect the wind density from the light cylinder to the TS, provided that the dissipation in the wind between the sonic point and the TS is negligible.

5.5   GeV emission from PSR B1259-63

At this stage, we investigate whether the particles accelerated in the shock precursor are able to produce GeV photons for the inferred values of σ_{TS} and Γ_{TS} in our benchmark model. From Chapt. 3, we know that particles (electrons and positrons) reflected at the TS are distributed in a relativistic Maxwell-like distribution peaked at $\gamma \approx \sigma_{TS}\Gamma_{TS} \approx \hat{\mu}$ as expressed in the lab. frame (see Fig. 3.8). In the binary system the dominant target photon fields for Inverse Compton scattering are photons coming from the Be star SS 2883 and photons coming from the circumstellar disk. The former target photon field has dimensionless average energy $\epsilon_{0,\star} = 2.7 k_B T_\star / mc^2 \sim 10^{-5}$, where we use the temperature at the pole of the Be star $T_\star = 3.4 \times 10^4 K$ [108] because of the large inclination of the disk with respect to the orbital plane ($\theta_{disk} \sim 70°$ [35, 91]). Here, $k_B = 1.38 \times 10^{-16} erg\ K^{-1}$ is the Boltzmann constant. This average photon energy corresponds to UV frequencies. The latter target photon field has dimensionless energy $\epsilon_{0,d} = 2.7 k_B T_d / mc^2 \sim 10^{-7}$, corresponding to NIR photons [139, 44]. These photons are upscattered to energies

$$\epsilon \approx \gamma^2 \epsilon_0 \tag{5.18}$$

in the Thomson regime ($\gamma\epsilon_0 \ll 1$) and to energies

$$\epsilon \approx \gamma \tag{5.19}$$

in the Klein-Nishina regime ($\gamma\epsilon_0 \gtrsim 1$), where $\epsilon = h\nu/mc^2$. The energy of photons in the GeV flare is $\epsilon \sim 2 \times 10^3$. In this order of magnitude estimate, we consider in Tab. 5.1 our benchmark results (highlighted in grey) for $\zeta = 23°$ and $R = 1$, providing $\gamma \sim 10^5$ ($\sigma_{TS} \sim 2.4 \times 10^3$, $\Gamma_{TS} \sim 50$). This implies that the upscattering of stellar photons would be at the limit of validity of the Thomson cross-section, providing $\epsilon \sim 1.4 \times 10^5$, whereas the upscattering of disk photons would be in the Thomson regime, providing $\epsilon \sim 1.4 \times 10^3$. Hence, the particle energised in the termination shock precursor are able to produce the GeV flare upscattering disk photons.

We stress that, in this scenario, the main contribution to the GeV emission is produced by electrons being accelerated in the region of turbulent fields ahead of the TS from energies $\gamma \approx \Gamma_{TS}$, the bulk energy of the pulsar wind, to energies $\gamma \approx \sigma_{TS}\Gamma_{TS}$, peak energy of a relativistic Maxwell-like distribution at the shock front as computed in Sect. 3.7. During the energisation of the wind electrons in the pre-shock, also the upscattering of stellar photons proceeds in the Thomson regime and can contribute to the GeV flare when $\gamma > 10^3$. On the other hand, electrons accelerated in the full Fermi process can reach very high energies $\gamma \gg 10^5$. The upscattering of target photons by these particles would occur in the Klein-Nishina regime and would probably contribute more at TeV than at GeV energies, which would explain the observation of PSR B1259-63 in the Very High Energy (TeV) band [4, 5]. Fermi acceleration is probably always at work at the TS of the pulsar wind [125, 116], since a certain degree of magnetic turbulence can always be expected both upstream and downstream of it. As inferred in Chapt. 4, the resulting spectrum depends on the ratio of the wavelength of the stripes to the gyro-radius of the energetic particles, though the field-dominated (regime I) and scattering-dominated (regime II) acceleration regimes do not produce substantially different spectral indexes. The efficiency of the acceleration (in terms of the number of accelerated particles) instead, depends on the injection probability, that we inferred being in the range $P_{inj} \sim 15\% - 40\%$ when the precursor establishes ahead of the TS (caution must be used with the value of P_{inj} since we used a test particle approach). However, despite, the relatively large value of P_{inj} inferred in this work, there is no strong evidence of an increase of the TeV emission during the GeV flare. This is probably due the fact that energy is radiated away very efficiently during the flare [107]. This is shown in Fig. 5.3, where the efficiency η_{IC} of Compton scattering is
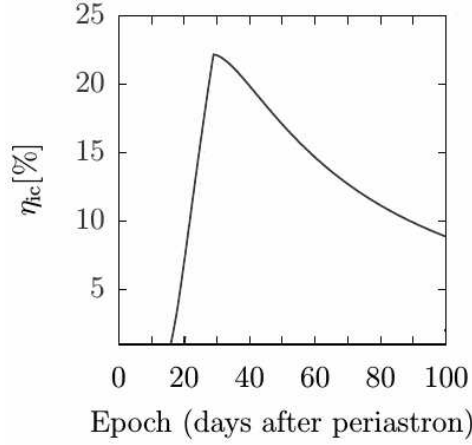
Figure 5.3: Efficiency of Compton scattering from an electromagnetic shock precursor, calculated for $\hat{\mu} = 6 \times 10^4$ and $\sigma = 100$ as a function of the time (in days) after periastron for the binary system containing PSR B1259-63. The stellar and orbital parameters are taken from [108]. Credits: adapted from Mochol & Kirk 2013 [107].

plotted as a function of the time after periastron passage for the system PSR B1259-63/SS 2883 for $\hat{\mu} = 6 \times 10^4$ and $\sigma_{TS} = 100$ [107]. The reason for the enhancement of η_{IC} is that in the electromagnetic precursor, the electron motion is mainly transverse to the direction of the flow, differently from what happens in the radial and unshocked striped-wind. Thus, electrons and positrons remain in the emission region for a time that is a factor $\gamma/p_{\parallel} \approx (8R)^{1/2}$ longer than that of radially propagating particles and consequently the radiated power is enhanced with respect to Inverse Compton emission of the same photons from the unshocked wind [107]. This argument is valid even if the results plotted in Fig. 5.3 are obtained for a magnetisation ten times smaller than what we estimate in the present work. The breakout of the electromagnetic precursor and the efficient deposition of the wind Poynting flux into particle kinetic energy mediated by superluminal waves thus provides a compelling scenario for the generation of the GeV flare in the binary system PSR B1259-63/SS 2883.

The decay of the GeV emission after the flare can be due to a number of factors: the drop of target photon flux with increasing orbital distance, the decay of the efficiency of Compton scattering, the less favourable inclination of the pulsar equatorial region or the instability of the shock precursor. Concerning the last point, we have seen in Chapt. 2 that a crucial condition for the formation of a stable electromagnetic pre-shock is that the propagation of superluminal waves is confined in a limited region close to the shock itself. This situation is more likely to be verified when $\omega \gtrsim \overline{\omega}_p$, corresponding to $R \gtrsim 1$. With increasing orbital distance (R changes by a factor of ~ 5 between the time of the flare and the time of apastron for fixed values of $\hat{\mu}$ and η) instead, the pulsar wind density drops and consequently the proper plasma frequency drops well below the pulsar frequency in an extended region upstream of the TS. In this case, the leading edge of the precursor moves apart from the TS since superluminal waves can propagate backwards until they reach the critical distance $R \sim 1$ and the structure of the pre-shock becomes unstable, as we showed with our two-fluid simulations (see Figs. 2.12 and 2.15 and related text for discussion). In turn, this might lead to a decrease of the Poynting flux dissipation efficiency, as shown in the bottom panels in Figs. 2.11

and 2.14, and consequently to a less effective electron energisation and radiation in the precursor.

At the time of the observed GeV flare, the system transitions from a regime in which superluminal waves are not allowed to one in which they can propagate. As the pulsar recedes from the companion, the stellar wind interacts with higher and higher latitudes in the pulsar wind, because of the inclination of the pulsar spin-axis with respect to the orbital plane. When the interaction occurs with the polar region of the pulsar wind where the precursor cannot form ([7]; see also Sect. 5.3) the system performs the opposite transition and the flare ceases. After the apastron passage, when the pulsar approaches SS 2883, a new transition to the superluminal waves regime can be expected. On this part of the orbit, however, the geometry of the system is different because of the inclination of the pulsar spin-axis with respect to the orbital plane. The location where the spin-axis and the line connecting the two stars are perpendicular (this is the favourable geometry at the beginning of the flare) corresponds to the true anomaly $f \sim 291°$ ($f_{o,1} \sim 271°$ and $f_{o,2} \sim 84°$ are the values of the true anomaly at the beginning and at the end of the radio eclipse related to the disk). As discussed in Sect. 5.3, at this location in the orbit the pulsar wind interacts with the dense equatorial stellar wind and the resulting density in the pulsar wind is likely to be too large for the the formation of the shock precursor. On the other hand, the location where the orbital distance is the same as at the beginning of the flare (for which $R \sim 1$) corresponds to $f \sim 249°$. This value of the true anomaly is not favourable since a twin, geometrically induced flare would start at $f'_1 \sim 258°$. Thus, at this location the stellar wind interacts with a high latitude region of the pulsar wind. Furthermore, as the pulsar approaches the companion and the geometrical conditions become more favourable, the pulsar wind becomes denser because of the interaction with the stellar wind, which makes the launch of the superluminal waves less probable. We also remark that, since the pulsar approaches and crosses the high-density equatorial stellar outflow during this section of the orbit, the pulsar wind is probably dense enough to prevent the propagation of superluminal waves and the formation of the precursor. This would rule out the scenario of a twin flare.

It is worth mentioning that the binary system PSR B1259-63/SS 2883 is not an isolated case. For instance, a similar system has been observed in the Small Magellanic Cloud containing the pulsar PSR J0045-7319 [70, 69, 19] in an eccentric orbit ($e = 0.81$) around a luminous companion similar to SS 2883. The frequency and the spin-down luminosity of this pulsar are $\sim 1.1\,Hz$ and $\sim 2.2 \times 10^{32}\,erg\,s^{-1}$, respectively. Also in this system the orbital separation changes by a factor of ~ 10 between apastron and periastron, making the scenario presented in this work very appealing, although the lower spin-down luminosity and the greater distance ($D \sim 60\,kpc$) mean that the foreseen γ-ray emission is probably unobservable [13].

As for the remaining γ-ray binaries, LS 5039 and LS I +61°303 seem to be the best candidate to be pulsars orbiting massive stars (see [49] for a review). However, their orbits are much less eccentric ($e = 0.35$ and $e = 0.54$ for LS 5039 and LS I +61°303, respectively) and much tighter to the companion, with a semi-major axis which is at least one order of magnitude smaller than that of PSR B1259-63 for both objects [32, 33]. As a consequence, if the massive companions of these putative pulsars are similar to SS 2883, the compact objects are always deeply embedded in the stellar wind during the orbit, which turns into an effective confinement and large density of the pulsar winds. This prevents, in these systems, the propagation of superluminal waves and the formation of the shock precursor which explains the lack of γ-ray flares in LS 5039 and LS I +61°303.

Chapter 6

Summary and conclusions

Pulsar Wind Nebulae (PWNe) are among the most efficient particle accelerators in the Universe and share many similarities with different classes of relativistic sources. The wealth of data from PWNe allows us to investigate the physics of shock acceleration and to compare our theoretical expectations with observations.

In PWNe, the fast rotation of the central pulsar drives the formation of a strong wind of relativistic electron-positron pairs and large amplitude electromagnetic fields. The magnetic field is frozen into the plasma and forms a pattern of stripes of alternating polarity separated by a corrugated current sheet, as described in the ideal-MHD approximation. The wind expands in the surrounding medium until its pressure is balanced by the ram pressure of the confining Supernova Remnant or Interstellar Medium, where it is terminated by a relativistic Termination Shock (TS). Close to the pulsar the wind is dense and its energy content is dominated by the electromagnetic component. However, sufficiently far away from the central pulsar, the density drops and the field can no longer be regarded as stationarily frozen-in. Beyond a critical distance, strong electromagnetic waves of superluminal phase speed can be generated by the conversion of the striped-wind. These waves deeply modifies the structure of the TS and mediate the dissipation of the Poynting flux carried by the wind into particle kinetic energy, as required by the observation of Synchrotron and Inverse Compton radiation at the location of TS.

We investigate with a 1-dimensional, relativistic, two-fluid code the modifications of the TS when the interaction of the striped-wind with the shock triggers the conversion into superluminal waves. We show that, independently of the values of the wind Lorentz factor Γ and magnetisation σ, the propagation of these waves forms a precursor ahead of the shock where the incoming flow is slowed down and the wind Poynting flux is transformed into enthalpy of the plasma. The breakout of the precursor always generates a linear expansion phase in which the leading edge of this structure travels upstream with speed χ. In general, the relative magnitude of χ with respect to the superluminal wave group speed determines whether the precursor keeps expanding upstream for the entire simulation, sets up in a stationary state where its extension remains constant with time, or undergoes an oscillation-like phase where its extension alternately expands and contracts. Interestingly, two stationary states are obtained for different values of Γ and σ when the distance of the TS from the pulsar is close to the critical distance.

The integration of test particle trajectories in the background electromagnetic fields of the stationary configurations of the pre-shock shows that electrons (and positrons) propagating in the precursor increase their energy by a factor roughly equal to σ. Downstream of the shock, the spectrum of particles is a Maxwell-like distribution, in agreement with the results of Particle-In-Cell simulations studying acceleration in annihilating magnetic fields

during shock driven reconnection. We find that electrons and positrons carried along with the wind are reflected back into the upstream and escape the simulation box with a probability that varies between 10% and 40%. These particles form a population of pre-accelerated particles upstream of the TS which are available for further acceleration. Although the value of the reflection probability might be large for the test particle approach to be consistent, our study suggests that the onset of the precursor is a possible solution to the injection problem to be investigated with a self-consistent approach.

We study the acceleration of injected electrons (and positrons) with a Monte Carlo code simulating the presence of magnetic turbulence (acting as elastic scattering centres) both upstream of the TS, in the striped pulsar wind, and downstream of it, in the unmagnetised nebula. We show that, when the scattering length is much larger than the wavelength of the stripes, the Fermi-like acceleration proceeds in two regimes dictated by the relative magnitude of the wavelength of the stripes and of the gyro-radius of energetic particles. The spectrum of accelerated electrons (in absence of radiation losses) is a power-law of index $s = 4.29 \pm 0.01$ when the acceleration is dominated by the magnetic field in the pulsar wind and $s = 4.23 \pm 0.01$ when the acceleration is dominated by the scattering off magnetic irregularities. For parameters reasonable in PWN environments, the acceleration is dominated by scattering. Therefore, if the acceleration is fast enough that radiation losses are negligible during the process, Fermi-like acceleration at the TS in PWNe produces a power-law with index similar to the one produced by the same mechanism at unmagnetised, relativistic shocks.

We discuss the implications of this acceleration scenario for the γ-ray binary system PSR B1259-63/SS 2883, where a pulsar and its nebula orbit a massive Be star producing a strong stellar wind. In binary systems, the conditions for the formation of the pre-shock which triggers efficient electron injection and acceleration can be periodically met during the orbit when the pulsar recedes from the companion. Assuming that this happens in coincidence with the onset of the powerful GeV flare occurring $\sim 30\,d$ after periastron passage, we build a geometrical model to constrain the inclination ζ of the pulsar magnetic dipole moment with respect to the spin-axis. We estimate $\zeta \sim 23°$ which entails that the necessary conditions for the establishment of the precursor are not met when the pulsar approaches the companion. This explains the lack of a twin flare. Although the model must be extended to fully consider the oblate shape of the TS and the shape of the critical surface beyond which superluminal waves can propagate, our estimate seems to correctly account for the main aspects of these two issues. The values of the product $\sigma\Gamma$ and multiplicity κ in the pulsar wind entailed by our scenario are in agreement with the results published in the literature for PSR B12259-63. We employ the value of ζ and the assumption concerning the breakout of the precursor to compute the density of electrons (and positrons) in the wind. Our evaluation is consistent with the density computed with magnetospheric pair production models within a factor of ~ 3. We show that the GeV flare emitted by PSR B1259-63 can be produced by electrons (and positrons) Compton scattering stellar and disk photons in the Thomson regime during the energisation in the shock precursor, while particles undergoing the full Fermi process probably contribute more at TeV energies.

Fermi acceleration is usually supposed to be inefficient at relativistic and perpendicular shock fronts because of the large degree of downstream advection. In this work, we show instead that the conversion of the pulsar striped-wind into superluminal waves and the subsequent breakout of the precursor creates an environment of turbulent fields able to trigger and sustain Fermi-like acceleration at the TS. This is particularly true in the equatorial region of the wind, where most of the radiation from PWNe is supposed to come from.

Appendix A

Lorentz transformations

For the purpose of clarity, we illustrate the geometry of the shock that we use in our set of simulations throughout this work. According to the case under consideration, the shock can be a non-relativistic shock front (in Sect. 4.1) or a relativistic one (in Sect. 4.3 and following). When the magnetic field is present upstream of the shock, as in Sect. 4.5.2, its direction is perpendicular to the shock normal, thus the shock is perpendicular. In Sect. 4.5.3 and in Chapt. 5, the shock represents the termination shock in a pulsar wind nebula, where upstream we simulate the pulsar wind and downstream the nebula. The same geometry of the shock also applies to the two-fluid simulations presented in Chapt. 2.

The shock front is a 2-dimensional infinite interface in the yz-plane, whose normal is parallel to the x-axis. The
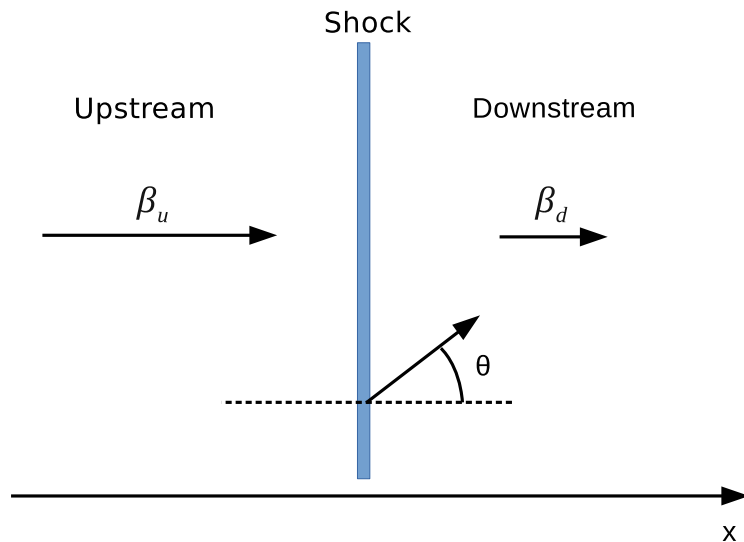

Figure A.1: Illustration of the geometry of the simulated shock.

97

speed of the upstream and downstream, as measured in the shock frame, are β_u and β_d, respectively, and are directed along the x-axis. The associated Lorentz factors are $\overline{\Gamma}_s = (1 - \beta_u^2)^{-1/2}$ and $\widetilde{\Gamma}_s = (1 - \beta_d^2)^{-1/2}$. The upstream fluid is on the left-hand side of the termination shock, the downstream is on the right-hand side of the shock, as illustrated in Fig. A.1. In the upstream and downstream reference frames, where the fluid is at rest, the speed of the shock is $\overline{\beta}_s = \beta_u$ and $\widetilde{\beta}_s = \beta_d$, respectively, which are anti-parallel to the shock normal (namely in the negative x-direction).

The polar angle θ is measured from the x-axis in the range $[0 : \pi]$, while the azimuthal angle ϕ in the yz-plane is measured from the y-axis in the range $[0 : 2\pi]$. The need to define both cartesian and polar spherical coordinates stems from the fact that the two-fluid simulation computes all the physical quantities, in particular the background electromagnetic fields, in cartesian coordinates, but polar spherical coordinates are more suitable for the numerical integration of the particle trajectories (see Chapts. 3 and 4).

In our treatment, there are three relevant reference frames: the upstream reference frame (URF), the downstream reference frame (DRF) and the shock reference frame (SRF) coinciding with the laboratory reference frame. The integration of test particle trajectories presented in Chapt. 3 is performed in SRF. The Monte Carlo simulation of the Fermi-like acceleration process, presented in Chapt. 4, is instead performed alternately in URF and DRF. These three frames are related by Lorentz transformations.

We define k a quantity expressed in SRF, $\overline{k}$ a quantity expressed in the URF and $\widetilde{k}$ a quantity expressed in the DRF. Notice that, in Chapts. 1 and 2, a quantity $\overline{k}$ is expressed in the comoving fluid frame of the fluid. The sets of Lorentz transformations connecting these reference frames is given in the following.

To transform from SRF to URF we use:

$$
\begin{cases}
\overline{x} = \overline{\Gamma}_s(x - \overline{\beta}_s t) & \text{(A.1)} \\[2mm]
\overline{t} = \overline{\Gamma}_s(t - \overline{\beta}_s x) & \text{(A.2)} \\[2mm]
\overline{\gamma} = \overline{\Gamma}_s(\gamma - \overline{\beta}_s p_x) & \text{(A.3)} \\[2mm]
\overline{\mu} = \dfrac{\mu - \overline{\beta}_s}{1 - \overline{\beta}_s \mu} & \text{(A.4)}
\end{cases}
$$

where $\overline{\Gamma}_s = (1 - \overline{\beta}_s^2)^{-1/2}$, $\mu = \cos\theta$ and $p_x = \beta\gamma\mu$ is the magnitude of the x component of the momentum of the electron ($m = 1$ in this work) and γ is the electron Lorentz factor.

The opposite set, to transform from URF to SRF, is

$$
\begin{cases}
x = \overline{\Gamma}_s(\overline{x} + \overline{\beta}_s \overline{t}) & \text{(A.5)} \\[2mm]
t = \overline{\Gamma}_s(\overline{t} + \overline{\beta}_s \overline{x}) & \text{(A.6)} \\[2mm]
\gamma = \overline{\Gamma}_s(\overline{\gamma} + \overline{\beta}_s \overline{p}_x) & \text{(A.7)} \\[2mm]
\mu = \dfrac{\overline{\mu} + \overline{\beta}_s}{1 + \overline{\beta}_s \overline{\mu}} \, . & \text{(A.8)}
\end{cases}
$$

Similarly, for the transformation from SRF to DRF, we have

$$\begin{cases} \widetilde{x} = \widetilde{\Gamma}_{\mathrm{s}}(x - \widetilde{\beta}_{\mathrm{s}}t) & \text{(A.9)} \\[2mm] \widetilde{t} = \widetilde{\Gamma}_{\mathrm{s}}(t - \widetilde{\beta}_{\mathrm{s}}x) & \text{(A.10)} \\[2mm] \widetilde{\gamma} = \widetilde{\Gamma}_{\mathrm{s}}(\gamma - \widetilde{\beta}_{\mathrm{s}}p_{\mathrm{x}}) & \text{(A.11)} \\[2mm] \widetilde{\mu} = \dfrac{\mu - \widetilde{\beta}_{\mathrm{s}}}{1 - \widetilde{\beta}_{\mathrm{s}}\mu}, & \text{(A.12)} \end{cases}$$

where $\widetilde{\Gamma}_{\mathrm{s}} = (1 - \widetilde{\beta}_{\mathrm{s}}^2)^{-1/2}$ is the Lorentz factor of the shock expressed in DRF. The opposite transformation from DRF to SRF is performed via

$$\begin{cases} x = \widetilde{\Gamma}_{\mathrm{s}}(\widetilde{x} + \widetilde{\beta}_{\mathrm{s}}\widetilde{t}) & \text{(A.13)} \\[2mm] t = \widetilde{\Gamma}_{\mathrm{s}}(\widetilde{t} + \widetilde{\beta}_{\mathrm{s}}\widetilde{x}) & \text{(A.14)} \\[2mm] \gamma = \widetilde{\Gamma}_{\mathrm{s}}(\widetilde{\gamma} + \widetilde{\beta}_{\mathrm{s}}\widetilde{p}_{\mathrm{x}}) & \text{(A.15)} \\[2mm] \mu = \dfrac{\widetilde{\mu} + \widetilde{\beta}_{\mathrm{s}}}{1 + \widetilde{\beta}_{\mathrm{s}}\widetilde{\mu}}. & \text{(A.16)} \end{cases}$$

To perform the transformation from URF to DRF and *viceversa* we need the relative speed between the two frames, which is computed as

$$\beta_{\mathrm{rel}} = \frac{\overline{\beta}_{\mathrm{s}} - \widetilde{\beta}_{\mathrm{s}}}{1 - \overline{\beta}_{\mathrm{s}}\widetilde{\beta}_{\mathrm{s}}} \sim 1 - \frac{1}{2\Gamma_{\mathrm{rel}}^2} \tag{A.17}$$

where $\Gamma_{\mathrm{rel}} \sim \overline{\Gamma}_{\mathrm{s}}/\sqrt{2}$ ([21], [79]). So the transformation from DRF to URF is realised through

$$\begin{cases} \overline{x} = \Gamma_{\mathrm{rel}}(\widetilde{x} - \beta_{\mathrm{rel}}\widetilde{t}) & \text{(A.18)} \\[2mm] \overline{t} = \Gamma_{\mathrm{rel}}(\widetilde{t} - \beta_{\mathrm{rel}}\widetilde{x}) & \text{(A.19)} \\[2mm] \overline{\gamma} = \Gamma_{\mathrm{rel}}(\widetilde{\gamma} - \beta_{\mathrm{rel}}\widetilde{p}_{\mathrm{x}}) & \text{(A.20)} \\[2mm] \overline{\mu} = \dfrac{\widetilde{\mu} - \beta_{\mathrm{rel}}}{1 - \beta_{\mathrm{rel}}\widetilde{\mu}} & \text{(A.21)} \end{cases}$$

whereas the opposite transformation from URF to DRF is performed via

$$\begin{cases} \widetilde{x} = \Gamma_{\mathrm{rel}}(\overline{x} + \beta_{\mathrm{rel}}\overline{t}) & \text{(A.22)} \\[2mm] \widetilde{t} = \Gamma_{\mathrm{rel}}(\overline{t} + \beta_{\mathrm{rel}}\overline{x}) & \text{(A.23)} \\[2mm] \widetilde{\gamma} = \Gamma_{\mathrm{rel}}(\overline{\gamma} + \beta_{\mathrm{rel}}\overline{p}_{\mathrm{x}}) & \text{(A.24)} \\[2mm] \widetilde{\mu} = \dfrac{\overline{\mu} + \beta_{\mathrm{rel}}}{1 + \beta_{\mathrm{rel}}\overline{\mu}}. & \text{(A.25)} \end{cases}$$

A particle in the upstream can be caught up by the shock, travelling with speed $\overline{\beta}_{\mathrm{s}}$ in the negative x-direction, only when the projection of its speed on the x-axis is larger than the speed of the shock, the condition being $\overline{\beta} \cdot \overline{\mu} > -\overline{\beta}_{\mathrm{s}}$. Similarly, a particle in the downstream can cross into the upstream only when the projection of its speed on the x-axis is smaller than the speed of the shock in that frame, namely when $\widetilde{\beta} \cdot \widetilde{\mu} < -\widetilde{\beta}_{\mathrm{s}}$. Given that normally we consider ultra-relativistic particles travelling almost at the speed of light, the previous conditions turn into $\overline{\mu} > -\overline{\beta}_{\mathrm{s}}$ and $\widetilde{\mu} < -\widetilde{\beta}_{\mathrm{s}}$.

The set of equations to Lorentz transform physical quantities between two frames of reference is essential in the Monte Carlo approach to the particle acceleration. In fact, this simulation is performed alternately in URF and DRF and the data we store, e.g. energy and momentum, are expressed alternately in URF or DRF. However, ultimately we want to express all of these quantities in the same reference frame to obtain the energy spectrum and the angular distribution (see Chapt. 4).

The Lorentz transformations are also needed for the electromagnetic field components. In the two-fluid simulation, the analytic form of the transverse, circularly polarised, magnetic shear wave is given in SRF and the components of the electric field are obtained thanks to the frozen-in condition

$$\mathbf{E} + \boldsymbol{\beta} \times \mathbf{B} = 0 \,. \tag{A.26}$$

The full set of electromagnetic components is

$$
\begin{cases}
B_x = 0 & \text{(A.27)} \\
B_y = B_0 \cos(k_0 x - \Omega t) & \text{(A.28)} \\
B_z = -B_0 \sin(k_0 x - \Omega t) & \text{(A.29)} \\
E_x = 0 & \text{(A.30)} \\
E_y = \beta B_z & \text{(A.31)} \\
E_z = -\beta B_y & \text{(A.32)}
\end{cases}
$$

where the frequency $\Omega = \omega/\overline{\omega}_{p0}$ is expressed in terms of the proper plasma frequency (Eq. 1.17) and the wavenumber is $k_0 = \Omega/\overline{\beta}_s > 0$, with $\overline{\beta}_s = \sqrt{1 - 1/\overline{\Gamma}_s^2}$ (for details see Chapt. 2). The four-wave-number vector is thus given by $\overrightarrow{k} = (\Omega, k_0, 0, 0)$. The Lorentz boost of the field components into URF is given by

$$
\begin{cases}
\overline{B}_x = 0 & \text{(A.33)} \\
\overline{B}_y = \overline{\Gamma}_s(B_y + \overline{\beta}_s E_z) = \dfrac{B_y}{\overline{\Gamma}_s} & \text{(A.34)} \\
\overline{B}_z = \overline{\Gamma}_s(B_z - \overline{\beta}_s E_y) = \dfrac{B_z}{\overline{\Gamma}_s} & \text{(A.35)} \\
\overline{E}_x = 0 & \text{(A.36)} \\
\overline{E}_y = \overline{\Gamma}_s(E_y - \overline{\beta}_s B_z) = 0 & \text{(A.37)} \\
\overline{E}_z = \overline{\Gamma}_s(E_z + \overline{\beta}_s B_y) = 0 & \text{(A.38)}
\end{cases}
$$

which is supplemented by the transformation of $\overrightarrow{k}$ into $\overline{\overrightarrow{k}} = (0, k_0/\overline{\Gamma}_s, 0, 0)$. Given that $\varphi = k^\nu x_\nu = \overline{k}^\nu \overline{x}_\nu$ we can write the analytic form of the magnetic shear in URF as

$$\overline{\mathbf{B}} = \frac{B_0}{\overline{\Gamma}_s}(\hat{\mathbf{y}} \cos \varphi - \hat{\mathbf{z}} \sin \varphi) \,. \tag{A.39}$$

Appendix B

Stochastic increments

The code for the numerical integration of the particle trajectory computes at every time step the following quantities $(x, y, z, \theta, \phi, \gamma)$, namely the position vector **x** of the particle in cartesian coordinates and the direction and magnitude of the momentum vector **p** in polar spherical coordinates, where θ is the polar angle and ϕ is the azimuthal angle about the x-axis (see Appen. A). The deterministic integration of electron trajectories is carried out using Eqs. 3.2-3.7 defined in Chapt. 3. The Monte Carlo method used to simulate the *pitch-angle* scattering off magnetic turbulence both in the upstream and downstream of the shock consists in a two-steps procedure, which is
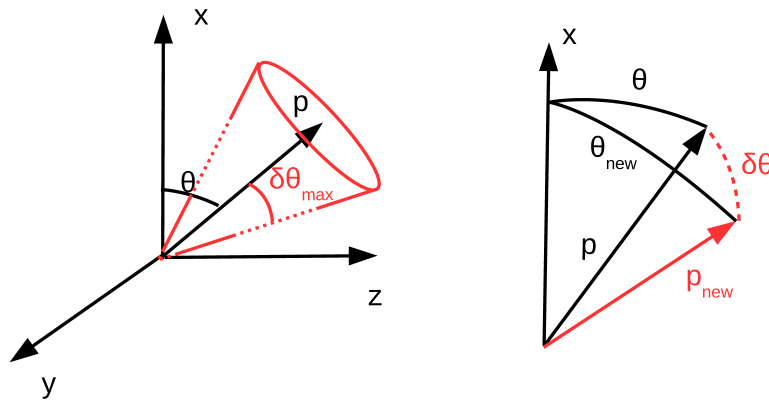

Figure B.1: Illustration of the procedure to obtain the stochastic increment in the Monte Carlo simulation.

illustrated in Fig. B.1. Firstly, in the left panel, the values of θ and ϕ are computed at a given time with the Eqs. 3.6 and 3.7, which provide the *deterministic* direction of the momentum **p**. A cone of aperture $\delta\theta_{max}$ is defined about **p**. Secondly, in the right panel of Fig. B.1, a new direction **p**$_{new}$ for the momentum is randomly generated within the cone about the previously obtained **p**. The new direction of the momentum is represented in red. The *stochastic* direction **p**$_{new}$ forms an angle $\delta\theta \leq \delta\theta_{max}$ with respect to **p** and its polar and azimuthal angles are θ_{new} and ϕ_{new}, respectively. The sum of many similar steps corresponds to a random motion $W(t_i)$ of the tip of the momentum vector on the surface of a sphere, represented in Fig. B.2.

This approach leads to a stochastic differential equation of the kind of Eq. 4.14 for θ and ϕ, where the *deterministic* increment is provided by the Lorentz force, as given in Eqs. 3.6 and 3.7, whereas the *stochastic* increment $\Delta W = W_{i+1} - W_i$ at each time step is nothing but $\Delta\theta = \theta_{new} - \theta$ for the polar angle and $\Delta\phi = \phi_{new} - \phi$ for the azimuthal angle, respectively. The computation of the new values of the angles is carried out as explained below. We use an auxiliary reference frame K' where $x' \equiv p$. Without loss of generality, y' lies in the xp-plane. In this frame, we define the cone aperture angle

$$\delta\theta_{max} = \alpha \sqrt{\Delta t} \tag{B.1}$$

where Δt is the integration time step and α is a proportionality factor which is set to unity, unless otherwise stated. We extract the polar angle $\delta\theta'$ in a flat random distribution in the range $[0 : \delta\theta_{max}]$ and the azimuthal angle ϕ' in a
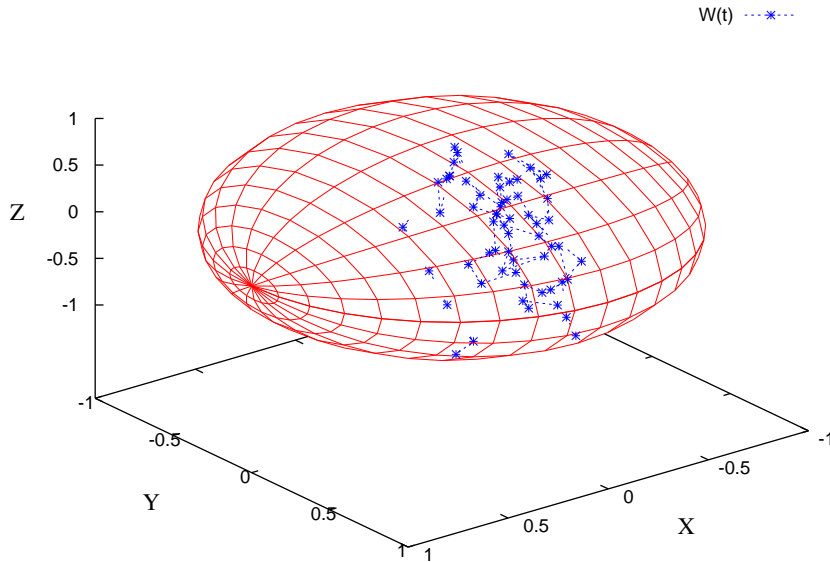

Figure B.2: The Wiener process corresponds to the random walk of the tip of the momentum vector on the surface of a sphere. Here the radius of the sphere is normalised to the magnitude of momentum p.

flat random distribution in the range $[-\pi : \pi]$. In K', the direction of the new momentum vector is

$$
\begin{pmatrix}
\cos \delta\theta' \\
\sin \delta\theta' \cos \phi' \\
\sin \delta\theta' \sin \phi'
\end{pmatrix}.
\tag{B.2}
$$

To transform this vector back to the frame of integration K, which represents alternately URF and DRF, we use the composite rotation matrix

$$
R(\theta, \phi) =
\begin{pmatrix}
\cos \theta & -\sin \theta & 0 \\
\sin \theta \cos \phi & \cos \theta \cos \phi & -\sin \phi \\
\sin \theta \sin \phi & \cos \theta \sin \phi & \cos \phi
\end{pmatrix}
\tag{B.3}
$$

from which we compute

$$
\frac{\mathbf{p}_{\text{new}}}{p} =
\begin{pmatrix}
\cos \delta\theta_{\text{new}} \\
\sin \delta\theta_{\text{new}} \cos \phi_{\text{new}} \\
\sin \delta\theta_{\text{new}} \sin \phi_{\text{new}}
\end{pmatrix} =
\begin{pmatrix}
n_{\text{new},x} \\
n_{\text{new},y} \\
n_{\text{new},z}
\end{pmatrix}
\tag{B.4}
$$

as

$$
\frac{\mathbf{p}_{\text{new}}}{p} =
\begin{pmatrix}
\cos \delta\theta' \cos \theta - \sin \delta\theta' \cos \delta\phi' \sin \theta \\
\cos \delta\theta' \sin \theta \cos \phi + \sin \delta\theta' \cos \delta\phi' \cos \theta \cos \phi - \sin \delta\theta' \sin \delta\phi' \sin \phi \\
\cos \delta\theta' \sin \theta \sin \phi + \sin \delta\theta' \cos \delta\phi' \cos \theta \sin \phi + \sin \delta\theta' \sin \delta\phi' \cos \phi
\end{pmatrix}.
\tag{B.5}
$$

The previous relations allow us to express the angles of the stochastically determined direction of momentum through

$$
\theta_{\text{new}} = \cos^{-1} \left[\cos \delta\theta' \cos \theta - \sin \delta\theta' \cos \delta\phi' \sin \theta \right]
\tag{B.6}
$$

$$
\phi_{\text{new}} =
\begin{cases}
\tan^{-1} \left(n_{\text{new},z}/n_{\text{new},y} \right) & \text{if } n_{\text{new},y} > 0 \\
\tan^{-1} \left(n_{\text{new},z}/n_{\text{new},y} \right) + \pi & \text{if } n_{\text{new},y} < 0, \ n_{\text{new},z} \geq 0 \\
\tan^{-1} \left(n_{\text{new},z}/n_{\text{new},y} \right) - \pi & \text{if } n_{\text{new},y} < 0, \ n_{\text{new},z} < 0.
\end{cases}
\tag{B.7}
$$

This algorithm activates at every time step of the numerical integration and provides to the integration routine the stochastic increment of the variables θ and ϕ in the appropriate Eq. 4.14, with the coefficient $b_i = 1$ in our treatment.

Bibliography

[1] Abdo, A. A. et al. (2011). Discovery of High-energy Gamma-ray Emission from the Binary System PSR B1259-63/LS 2883 around Periastron with Fermi. *ApJ*, 736:L11.

[2] Achterberg, A., Gallant, Y. A., Kirk, J. G., and Guthmann, A. W. (2001). Particle acceleration by ultrarelativistic shocks: theory and simulations. *MNRAS*, 328:393–408.

[3] Achterberg, A. and Krülls, W. M. (1992). A fast simulation method for particle acceleration. *A&A*, 265:L13–L16.

[4] Aharonian, F., Akhperjanian, A. G., et al. (2005). Discovery of the binary pulsar PSR B1259-63 in very-high-energy gamma rays around periastron with HESS. *A&A*, 442:1–10.

[5] Aharonian, F., Akhperjanian, A. G., et al. (2009). Very high energy γ-ray observations of the binary PSR B1259-63/SS2883 around the 2007 Periastron. *A&A*, 507:389–396.

[6] Amano, T. and Kirk, J. G. (2013). The Role of Superluminal Electromagnetic Waves in Pulsar Wind Termination Shocks. *ApJ*, 770:18.

[7] Arka, I. and Kirk, J. G. (2012). Superluminal Waves in Pulsar Winds. *ApJ*, 745:108.

[8] Arons, J. (1983). Pair creation above pulsar polar caps - Geometrical structure and energetics of slot gaps. *ApJ*, 266:215–241.

[9] Arons, J. (2002). Theory of Pulsar Winds. In Slane, P. O. and Gaensler, B. M., editors, *Neutron Stars in Supernova Remnants*, volume 271 of *Astronomical Society of the Pacific Conference Series*, page 71.

[10] Asseo, E., Kennel, C. F., and Pellat, R. (1978). Synchro-Compton radiation damping of relativistically strong linearly polarized plasma waves. *A&A*, 65:401–408.

[11] Asseo, E., Pellat, R., and Llobet, X. (1984). Spherical propagation of large amplitude pulsar waves. *A&A*, 139:417–425.

[12] Axford, W. I., Leer, E., and Skadron, G. (1977). The acceleration of cosmic rays by shock waves. *International Cosmic Ray Conference*, 11:132–137.

[13] Ball, L. and Kirk, J. G. (2000). Probing pulsar winds using inverse Compton scattering. *Astroparticle Physics*, 12:335–349.

[14] Ballard, K. R. and Heavens, A. F. (1991). First-order Fermi acceleration at oblique relativistic magnetohy-drodynamic shocks. *MNRAS*, 251:438–448.

[15] Ballard, K. R. and Heavens, A. F. (1992). Shock acceleration and steep-spectrum synchrotron sources. *MNRAS*, 259:89–94.

[16] Begelman, M. C. (1998). Instability of Toroidal Magnetic Field in Jets and Plerions. *ApJ*, 493:291–300.

[17] Begelman, M. C. and Kirk, J. G. (1990). Shock-drift particle acceleration in superluminal shocks - A model for hot spots in extragalactic radio sources. *ApJ*, 353:66–80.

[18] Bell, A. R. (1978). The acceleration of cosmic rays in shock fronts. I. *MNRAS*, 182:147–156.

[19] Bell, J. F., Bessell, M. S., Stappers, B. W., Bailes, M., and Kaspi, V. M. (1995). PSR J0045-7319: A Dual-Line Binary Radio Pulsar. *ApJ*, 447:L117.

[20] Blandford, R. D., Applegate, J. H., and Hernquist, L. (1983). Thermal origin of neutron star magnetic fields. *MNRAS*, 204:1025–1048.

[21] Blandford, R. D. and McKee, C. F. (1976). Fluid dynamics of relativistic blast waves. *Physics of Fluids*, 19:1130–1138.

[22] Blandford, R. D. and Ostriker, J. P. (1978). Particle acceleration by astrophysical shocks. *ApJ*, 221:L29–L32.

[23] Bogovalov, S. V. (1999). On the physics of cold MHD winds from oblique rotators. *A&A*, 349:1017–1026.

[24] Bogovalov, S. V. and Khangoulian, D. V. (2002). On the origin of the torus and jet-like structures in the centre of the Crab Nebula. *MNRAS*, 336:L53–L55.

[25] Bogovalov, S. V., Khangulyan, D., Koldoba, A. V., Ustyugova, G. V., and Aharonian, F. A. (2012). Modelling the interaction between relativistic and non-relativistic winds in the binary system PSR B1259-63/SS2883- II. Impact of the magnetization and anisotropy of the pulsar wind. *MNRAS*, 419:3426–3432.

[26] Bosch-Ramon, V., Barkov, M. V., Khangulyan, D., and Perucho, M. (2012). Simulations of stellar/pulsar-wind interaction along one full orbit. *A&A*, 544:A59.

[27] Bucciantini, N. (2014). Pulsar Wind Nebulae Modeling. *International Journal of Modern Physics Conference Series*, 28:1460162.

[28] Bucciantini, N., Arons, J., and Amato, E. (2011). Modelling spectral evolution of pulsar wind nebulae inside supernova remnants. *MNRAS*, 410:381–398.

[29] Buckley, R. (1977). Pulsar magnetospheres with arbitrary geometry in the force-free approximation. *MNRAS*, 180:125–140.

[30] Bühler, R. and Blandford, R. (2014). The surprising Crab pulsar and its nebula: a review. *Reports on Progress in Physics*, 77(6):066901.

[31] Caliandro, G. A., Cheung, C. C., Li, J., Scargle, J. D., Torres, D. F., Wood, K. S., and Chernyakova, M. (2015). Gamma-Ray Flare Activity from PSR B1259-63 during 2014 Periastron Passage and Comparison to Its 2010 Passage. *ApJ*, 811:68.

[32] Casares, J., Ribas, I., Paredes, J. M., Martí, J., and Allende Prieto, C. (2005a). Orbital parameters of the microquasar LS I +61 303. *MNRAS*, 360:1105–1109.

[33] Casares, J., Ribó, M., Ribas, I., Paredes, J. M., Martí, J., and Herrero, A. (2005b). A possible black hole in the γ-ray microquasar LS 5039. *MNRAS*, 364:899–908.

[34] Chernyakova, M. and Illarionov, A. (2000). Non-pulsed Emission from the Binary System B1259-63. *Ap&SS*, 274:177–188.

[35] Chernyakova, M., Neronov, A., Lutovinov, A., Rodriguez, J., and Johnston, S. (2006). XMM-Newton observations of PSR B1259-63 near the 2004 periastron passage. *MNRAS*, 367:1201–1208.

[36] Chernyakova, M., Neronov, A., van Soelen, B., Callanan, P., O'Shaughnessy, L., Babyk, I., Tsygankov, S., Vovk, I., Krivonos, R., Tomsick, J. A., Malyshev, D., Li, J., Wood, K., Torres, D., Zhang, S., Kretschmar, P., McSwain, M. V., Buckley, D. A. H., and Koen, C. (2015). Multi-wavelength observations of the binary system PSR B1259-63/LS 2883 around the 2014 periastron passage. *MNRAS*, 454:1358–1370.

[37] Chiueh, T., Li, Z.-Y., and Begelman, M. C. (1998). A Critical Analysis of Ideal Magnetohydrodynamic Models for Crab-like Pulsar Winds. *ApJ*, 505:835–843.

[38] Clemmow, P. C. (1974). Nonlinear waves in a cold plasma by Lorentz transformation. *Journal of Plasma Physics*, 12:297–317.

[39] Clemmow, P. C. (1977). Nonlinear, superluminous, periodic waves in a plasma with magnetic field. *Journal of Plasma Physics*, 17:301–316.

[40] Contopoulos, I. and Kazanas, D. (2002). Toward Resolving the Crab σ-Problem: A Linear Accelerator? *ApJ*, 566:336–342.

[41] Coroniti, F. V. (1990). Magnetically striped relativistic magnetohydrodynamic winds - The Crab Nebula revisited. *ApJ*, 349:538–545.

[42] Del Zanna, L., Amato, E., and Bucciantini, N. (2004). Axially symmetric relativistic MHD simulations of Pulsar Wind Nebulae in Supernova Remnants. On the origin of torus and jet-like features. *A&A*, 421:1063–1073.

[43] Del Zanna, L., Volpi, D., Amato, E., and Bucciantini, N. (2006). Simulated synchrotron emission from pulsar wind nebulae. *A&A*, 453:621–633.

[44] Dougherty, S. M., Waters, L. B. F. M., Burki, G., Cote, J., Cramer, N., van Kerkwijk, M. H., and Taylor, A. R. (1994). Near-IR excess of Be stars. *A&A*, 290.

[45] Drury, L. O. (1983). An introduction to the theory of diffusive shock acceleration of energetic particles in tenuous plasmas. *Reports on Progress in Physics*, 46:973–1027.

[46] Drury, L. O. (1992). Particle acceleration in supernova remnants. In Zank, G. P. and Gaisser, T. K., editors, *Particle Acceleration in Cosmic Plasmas*, volume 264 of *American Institute of Physics Conference Series*, pages 189–194.

[47] Drury, L. O. and Voelk, J. H. (1981). Hydromagnetic shock structure in the presence of cosmic rays. *ApJ*, 248:344–351.

[48] Dubus, G. (2006). Gamma-ray binaries: pulsars in disguise? *A&A*, 456:801–817.

[49] Dubus, G. (2013). Gamma-ray binaries and related systems. *A&AR*, 21:64.

[50] Dubus, G. and Cerutti, B. (2013). What caused the GeV flare of PSR B1259-63? *A&A*, 557:A127.

[51] Dubus, G., Lamberts, A., and Fromang, S. (2015). Modelling the high-energy emission from gamma-ray binaries using numerical relativistic hydrodynamics. *A&A*, 581:A27.

[52] Ellison, D. C. and Double, G. P. (2004). Diffusive shock acceleration in unmodified relativistic, oblique shocks. *Astroparticle Physics*, 22:323–338.

[53] Ellison, D. C., Reynolds, S. P., and Jones, F. C. (1990). First-order Fermi particle acceleration by relativistic shocks. *ApJ*, 360:702–714.

[54] Fermi, E. (1949). On the Origin of the Cosmic Radiation. *Physical Review*, 75:1169–1174.

[55] Gaensler, B. M. and Slane, P. O. (2006). The Evolution and Structure of Pulsar Wind Nebulae. *ARAA*, 44:17–47.

[56] Gardiner, C. W. (2004). *Handbook of stochastic methods for physics, chemistry and the natural sciences*, volume 13 of *Springer Series in Synergetics*. Springer-Verlag, Berlin.

[57] Goldreich, P. and Julian, W. H. (1969). Pulsar Electrodynamics. *ApJ*, 157:869.

[58] Guo, F. and Giacalone, J. (2010). The Effect of Large-scale Magnetic Turbulence on the Acceleration of Electrons by Perpendicular Collisionless Shocks. *ApJ*, 715:406–411.

[59] Guo, F. and Giacalone, J. (2015). The Acceleration of Electrons at Collisionless Shocks Moving Through a Turbulent Magnetic Field. *ApJ*, 802:97.

[60] Hadasch, D., Torres, D. F., Tanaka, T., Corbet, R. H. D., Hill, A. B., Dubois, R., Dubus, G., Glanzman, T., Corbel, S., Li, J., Chen, Y. P., Zhang, S., Caliandro, G. A., Kerr, M., Richards, J. L., Max-Moerbeck, W., Readhead, A., and Pooley, G. (2012). Long-term Monitoring of the High-energy γ-Ray Emission from LS I +61°303° and LS 5039. *ApJ*, 749:54.

[61] Hester, J. et al. (2013). Crab nebula composite image, http://chandra.harvard.edu/photo/2002/0052/more.html.

[62] Hibschman, J. A. and Arons, J. (2001a). Pair Multiplicities and Pulsar Death. *ApJ*, 554:624–635.

[63] Hibschman, J. A. and Arons, J. (2001b). Pair Production Multiplicities in Rotation-powered Pulsars. *ApJ*, 560:871–884.

[64] Johnston, S., Ball, L., Wang, N., and Manchester, R. N. (2005). Radio observations of PSR B1259-63 through the 2004 periastron passage. *MNRAS*, 358:1069–1075.

[65] Johnston, S., Manchester, R. N., Lyne, A. G., Bailes, M., Kaspi, V. M., Qiao, G., and D'Amico, N. (1992). PSR 1259-63 - A binary radio pulsar with a Be star companion. *ApJ*, 387:L37–L41.

[66] Johnston, S., Manchester, R. N., Lyne, A. G., Nicastro, L., and Spyromilio, J. (1994). Radio and Optical Observations of the PSR:B1259-63 / SS:2883 Be-Star Binary System. *MNRAS*, 268:430.

[67] Kargaltsev, O., Cerutti, B., Lyubarsky, Y., and Striani, E. (2015). Pulsar-Wind Nebulae. Recent Progress in Observations and Theory. *Space Sci Rev*, 191:391–439.

[68] Kargaltsev, O. and Pavlov, G. G. (2008). Pulsar Wind Nebulae in the Chandra Era. In Bassa, C., Wang, Z., Cumming, A., and Kaspi, V. M., editors, *40 Years of Pulsars: Millisecond Pulsars, Magnetars and More*, volume 983 of *American Institute of Physics Conference Series*, pages 171–185.

[69] Kaspi, V. M., Bell, J. F., Bessell, M., Stappers, B., Bailes, M., and Manchester, R. N. (1994a). Radio and Optical Observations of PSR J0045-7319. In *American Astronomical Society Meeting Abstracts*, volume 26 of *Bulletin of the American Astronomical Society*, page 1416.

[70] Kaspi, V. M., Johnston, S., Bell, J. F., Manchester, R. N., Bailes, M., Bessell, M., Lyne, A. G., and D'Amico, N. (1994b). A massive radio pulsar binary in the Small Magellanic Cloud. *ApJ*, 423:L43–L45.

[71] Kennel, C. F. and Coroniti, F. V. (1984a). Confinement of the Crab pulsar's wind by its supernova remnant. *ApJ*, 283:694–709.

[72] Kennel, C. F. and Coroniti, F. V. (1984b). Magnetohydrodynamic model of Crab nebula radiation. *ApJ*, 283:710–730.

[73] Khangulyan, D., Aharonian, F. A., Bogovalov, S. V., and Ribó, M. (2011). Gamma-Ray Signal from the Pulsar Wind in the Binary Pulsar System PSR B1259-63/LS 2883. *ApJ*, 742:98.

[74] Khangulyan, D., Aharonian, F. A., Bogovalov, S. V., and Ribó, M. (2012). Post-periastron Gamma-Ray Flare from PSR B1259-63/LS 2883 as a Result of Comptonization of the Cold Pulsar Wind. *ApJ*, 752:L17.

[75] Khangulyan, D., Hnatic, S., Aharonian, F., and Bogovalov, S. (2007). TeV light curve of PSR B1259-63/SS2883. *MNRAS*, 380:320–330.

[76] Kirk, J. G. (2010). Waves in pulsar winds. *Plasma Physics and Controlled Fusion*, 52(12):124029.

[77] Kirk, J. G., Ball, L., and Skjæraasen, O. (1999). Inverse Compton emission of TeV gamma rays from PSR B1259-63. *Astroparticle Physics*, 10:31–45.

[78] Kirk, J. G., Bell, A. R., and Arka, I. (2009a). Pair production in counter-propagating laser beams. *Plasma Physics and Controlled Fusion*, 51(8):085008.

[79] Kirk, J. G. and Duffy, P. (1999). TOPICAL REVIEW: Particle acceleration and relativistic shocks. *Journal of Physics G Nuclear Physics*, 25:163.

[80] Kirk, J. G. et al. (2009b). Striped-wind corrugated current sheet, https://www.mpi-hd.mpg.de/mpi/en/ta/research/pulsar-winds/.

[81] Kirk, J. G., Guthmann, A. W., Gallant, Y. A., and Achterberg, A. (2000). Particle Acceleration at Ultrarelativistic Shocks: An Eigenfunction Method. *ApJ*, 542:235–242.

[82] Kirk, J. G., Lyubarsky, Y., and Petri, J. (2009c). The Theory of Pulsar Winds and Nebulae. In Becker, W., editor, *Astrophysics and Space Science Library*, volume 357 of *Astrophysics and Space Science Library*, page 421.

[83] Kirk, J. G., Melrose, D. B., Priest, E. R., Benz, A. O., and Courvoisier, T. J.-L., editors (1994). *Plasma Astrophysics*.

[84] Kirk, J. G. and Mochol, I. (2011). Charge-starved, Relativistic Jets and Blazar Variability. *ApJ*, 729:104.

[85] Kirk, J. G. and Schneider, P. (1987). On the acceleration of charged particles at relativistic shock fronts. *ApJ*, 315:425–433.

[86] Kirk, J. G. and Skjæraasen, O. (2003). Dissipation in Poynting-Flux-dominated Flows: The σ-Problem of the Crab Pulsar Wind. *ApJ*, 591:366–379.

[87] Kochanek, C. S. (1993). Some implications of PSR 1259-63. *ApJ*, 406:638–650.

[88] Komissarov, S. S. and Lyubarsky, Y. E. (2003). The origin of peculiar jet-torus structure in the Crab nebula. *MNRAS*, 344:L93–L96.

[89] Komissarov, S. S. and Lyubarsky, Y. E. (2004). Synchrotron nebulae created by anisotropic magnetized pulsar winds. *MNRAS*, 349:779–792.

[90] Kong, S. W., Cheng, K. S., and Huang, Y. F. (2012). Modeling the Multiwavelength Light Curves of PSR B1259-63/LS 2883. II. The Effects of Anisotropic Pulsar Wind and Doppler Boosting. *ApJ*, 753:127.

[91] Kong, S. W., Yu, Y. W., Huang, Y. F., and Cheng, K. S. (2011). Modelling the multiwavelength light curves of PSR B1259-63/SS 2883. *MNRAS*, 416:1067–1076.

[92] Levenberg, K. (1944). A method for the solution of certain non-linear problems in least squares. *Quarterly Journal of Applied Mathmatics*, 2:164–168.

[93] Lyubarsky, Y. and Kirk, J. G. (2001). Reconnection in a Striped Pulsar Wind. *ApJ*, 547:437–448.

[94] Lyubarsky, Y. E. (2002). On the structure of the inner Crab Nebula. *MNRAS*, 329:L34–L36.

[95] Lyubarsky, Y. E. (2003). The termination shock in a striped pulsar wind. *MNRAS*, 345:153–160.

[96] Manchester, R. N., Damico, N., and Tuohy, I. R. (1985). A search for short-period pulsars. *MNRAS*, 212:975–986.

[97] Maraschi, L. and Treves, A. (1981). A model for LSI61 deg 303. *MNRAS*, 194:1P–5P.

[98] Marquardt, D. (1963). An Algorithm for Least-Squares Estimation of Nonlinear Parameters. *An Algorithm for Least-Squares Estimation of Nonlinear Parameters*, 11:431–441.

[99] Max, C. E. (1973). Parametric instability of a relativistically strong electromagnetic wave. *Physics of Fluids*, 16:1480–1489.

[100] Melatos, A. and Melrose, D. B. (1996). Energy transport in a rotation-modulated pulsar wind. *MNRAS*, 279:1168–1190.

[101] Meyer, M., Horns, D., and Zechlin, H.-S. (2010). The Crab Nebula as a standard candle in very high-energy astrophysics. *A&A*, 523:A2.

[102] Michel, F. C. (1969). Relativistic Stellar-Wind Torques. *ApJ*, 158:727.

[103] Michel, F. C. (1973). Rotating Magnetospheres: an Exact 3-D Solution. *ApJ*, 180:L133.

[104] Michel, F. C. (1991). *Theory of neutron star magnetospheres*. Chicago, University of Chicago Press, 1991.

[105] Michel, F. C. (1994). Magnetic structure of pulsar winds. *ApJ*, 431:397–401.

[106] Mirabel, I. F. (2006). Very energetic gamma-rays from microquasars and binary pulsars. *Science*, 312:1759.

[107] Mochol, I. and Kirk, J. G. (2013). Radiative Damping and Emission Signatures of Strong Superluminal Waves in Pulsar Winds. *ApJ*, 776:40.

[108] Negueruela, I., Ribó, M., Herrero, A., Lorenzo, J., Khangulyan, D., and Aharonian, F. A. (2011). Astrophysical Parameters of LS 2883 and Implications for the PSR B1259-63 Gamma-ray Binary. *ApJ*, 732:L11.

[109] Okazaki, A. T., Nagataki, S., Naito, T., Kawachi, A., Hayasaki, K., Owocki, S. P., and Takata, J. (2011). Hydrodynamic Interaction between the Be Star and the Pulsar in the TeV Binary PSR B1259-63/LS 2883. *PASJ*, 63:893–901.

[110] Olmi, B., Del Zanna, L., Amato, E., and Bucciantini, N. (2015). Constraints on particle acceleration sites in the Crab nebula from relativistic magnetohydrodynamic simulations. *MNRAS*, 449:3149–3159.

[111] Ostrowski, M. (1993). Cosmic-Ray Acceleration at Relativistic Shock Waves in the Presence of Oblique Magnetic Fields with Finite-Amplitude Perturbations. *MNRAS*, 264:248.

[112] Peacock, J. A. (1981). Fermi acceleration by relativistic shock waves. *MNRAS*, 196:135–152.

[113] Pétri, J. and Dubus, G. (2011). Implication of the striped pulsar wind model for gamma-ray binaries. *MNRAS*, 417:532–540.

[114] Pétri, J. and Lyubarsky, Y. (2007). Magnetic reconnection at the termination shock in a striped pulsar wind. *A&A*, 473:683–700.

[115] Porth, O., Komissarov, S. S., and Keppens, R. (2013). Solution to the sigma problem of pulsar wind nebulae. *MNRAS*, 431:L48–L52.

[116] Porth, O., Komissarov, S. S., and Keppens, R. (2014). Three-dimensional magnetohydrodynamic simulations of the Crab nebula. *MNRAS*, 438:278–306.

[117] Press, W. H., Flannery, B. P., and Teukolsky, S. A. (1986). *Numerical recipes. The art of scientific computing*. Cambridge: University Press, 1986.

[118] Rees, M. J. and Gunn, J. E. (1974). The origin of the magnetic field and relativistic particles in the Crab Nebula. *MNRAS*, 167:1–12.

[119] Riquelme, M. A. and Spitkovsky, A. (2011). Electron Injection by Whistler Waves in Non-relativistic Shocks. *ApJ*, 733:63.

[120] Ruderman, M. A. and Sutherland, P. G. (1975). Theory of pulsars - Polar caps, sparks, and coherent microwave radiation. *ApJ*, 196:51–72.

[121] Rybicki, G. B. and Lightman, A. P. (1979). *Radiative processes in astrophysics*. Wiley-VCH, 1979.

[122] Scholer, M. (1990). Diffuse ions at a quasi-parallel collisionless shock - Simulations. *GRL*, 17:1821–1824.

[123] Shimada, N., Terasawa, T., Hoshino, M., Naito, T., Matsui, H., Koi, T., and Maezawa, K. (1999). Diffusive Shock Acceleration of Electrons at an Interplanetary Shock Observed on 21 Feb 1994. *ApSS*, 264:481–488.

[124] Sironi, L. and Spitkovsky, A. (2009). Particle Acceleration in Relativistic Magnetized Collisionless Pair Shocks: Dependence of Shock Acceleration on Magnetic Obliquity. *ApJ*, 698:1523–1549.

[125] Sironi, L. and Spitkovsky, A. (2011). Acceleration of Particles at the Termination Shock of a Relativistic Striped Wind. *ApJ*, 741:39.

[126] Skjæraasen, O., Melatos, A., and Spitkovsky, A. (2005). Particle-in-Cell Simulations of a Nonlinear Transverse Electromagnetic Wave in a Pulsar Wind Termination Shock. *ApJ*, 634:542–546.

[127] Spruit, H. C. (2002). Dynamo action by differential rotation in a stably stratified stellar interior. *A&A*, 381:923–932.

[128] Summerlin, E. J. and Baring, M. G. (2012). Diffusive Acceleration of Particles at Oblique, Relativistic, Magnetohydrodynamic Shocks. *ApJ*, 745:63.

[129] Takamoto, M. and Kirk, J. G. (2015). Rapid Cosmic-ray Acceleration at Perpendicular Shocks in Supernova Remnants. *ApJ*, 809:29.

[130] Takata, J. and Taam, R. E. (2009). Probing the Pulsar Wind in the γ-ray Binary System PSR B1259-63/SS 2883. *ApJ*, 702:100–113.

[131] Tam, P. H. T., Li, K. L., Takata, J., Okazaki, A. T., Hui, C. Y., and Kong, A. K. H. (2015). High-energy Observations of PSR B1259-63/LS 2883 through the 2014 Periastron Passage: Connecting X-Rays to the GeV Flare. *ApJ*, 798:L26.

[132] Tavani, M. and Arons, J. (1997). Theory of High-Energy Emission from the Pulsar/Be Star System PSR 1259-63. I. Radiation Mechanisms and Interaction Geometry. *ApJ*, 477:439–464.

[133] Tavani, M., Arons, J., and Kaspi, V. M. (1994). Regimes of high-energy shock emission from the Be star/pulsar system PSR 1259-63. *ApJ*, 433:L37–L40.

[134] Teraki, Y., Ito, H., and Nagataki, S. (2015). Particle Acceleration in Superluminal Strong Waves. *ApJ*, 805:138.

[135] Timokhin, A. N. and Harding, A. K. (2015). On the Polar Cap Cascade Pair Multiplicity of Young Pulsars. *ApJ*, 810:144.

[136] Uchiyama, Y., Tanaka, T., Takahashi, T., Mori, K., and Nakazawa, K. (2009). Suzaku Observations of PSR B1259-63: A New Manifestation of Relativistic Pulsar Wind. *ApJ*, 698:911–921.

[137] Vietri, M. (1995). The Acceleration of Ultra–High-Energy Cosmic Rays in Gamma-Ray Bursts. *ApJ*, 453:883.

[138] Waters, L. B. F. M. (1986). The density structure of discs around Be stars derived from IRAS observations. *A&A*, 162:121–139.

[139] Waters, L. B. F. M., van den Heuvel, E. P. J., Taylor, A. R., Habets, G. M. H. J., and Persi, P. (1988). Evidence for low-velocity winds in Be/X-ray binaries. *A&A*, 198:200–210.

[140] Wentzel, D. G. (1974). Cosmic-ray propagation in the Galaxy - Collective effects. *Annual Reviews of Astronomy & Astrophysics*, 12:71–96.

[141] Zhang, B. and Harding, A. K. (2000). Full Polar Cap Cascade Scenario: Gamma-Ray and X-Ray Luminosities from Spin-powered Pulsars. *ApJ*, 532:1150–1171.